# Growth, Optical Properties, and Optimization of Infrared Optoelectronic Materials

by

Preston Thomas Webster

A Dissertation Presented in Partial Fulfillment
of the Requirements for the Degree
Doctor of Philosophy

Approved May 2016 by the
Graduate Supervisory Committee:

Shane R. Johnson, Chair
Yong-Hang Zhang
José Menéndez
Dragica Vasileska

ARIZONA STATE UNIVERSITY

August 2016

ABSTRACT

High-performance III-V semiconductors based on ternary alloys and superlattice systems are fabricated, studied, and compared for infrared optoelectronic applications. InAsBi is a ternary alloy near the GaSb lattice constant that is not as thoroughly investigated as other III-V alloys and that is challenging to produce as Bi has a tendency to surface segregate and form droplets during growth rather than incorporate. A growth window is identified within which high-quality droplet-free bulk InAsBi is produced and Bi mole fractions up to 6.4% are obtained. Photoluminescence with high internal quantum efficiency is observed from InAs/InAsBi quantum wells. The high structural and optical quality of the InAsBi materials examined demonstrates that bulk, quantum well, and superlattice structures utilizing InAsBi are an important design option for efficient infrared coverage.

Another important infrared material system is InAsSb and the strain-balanced InAs/InAsSb superlattice on GaSb. Detailed examination of X-ray diffraction, photoluminescence, and spectroscopic ellipsometry data provides the temperature and composition dependent bandgap of bulk InAsSb. The unintentional incorporation of approximately 1% Sb into the InAs layers of the superlattice is measured and found to significantly impact the analysis of the InAs/InAsSb band alignment. In the analysis of the absorption spectra, the ground state absorption coefficient and transition strength of the superlattice are proportional to the square of the electron-hole wavefunction overlap; wavefunction overlap is therefore a major design parameter in terms of optimizing absorption in these materials. Furthermore in addition to improvements through design

optimization, the optical quality of the materials studied is found to be positively enhanced with the use of Bi as a surfactant during molecular beam epitaxy growth.

A software tool is developed that calculates and optimizes the miniband structure of semiconductor superlattices, including bismide-based designs. The software has the capability to limit results to designs that can be produced with high structural and optical quality, and optimized designs in terms of maximizing absorption are identified for several infrared superlattice systems at the GaSb lattice constant. The accuracy of the software predictions are tested with the design and growth of an optimized mid-wave infrared InAs/InAsSb superlattice which exhibits superior optical and absorption properties.

ACKNOWLEDGMENTS

I would foremost like to acknowledge the support provided to me by my wife and best friend Denise Webster. I would like to thank my advisor and friend Dr. Shane Johnson, for giving me the opportunity to work with this excellent group of people and for always being available to guide me in this research. I would also like to thank the other members of my committee, Dr. Yong-Hang Zhang, Dr. José Menéndez, and Dr. Dragica Vasileska for their guidance and advice. I am also grateful to my father Tom Webster, my mother Lori McAllister, my sister Kadie Webster, the rest of my family and the other students in our group.

Additionally, I would also like to acknowledge financial support through the U.S. Army Research Office MURI program (Grant Number W911NF-10-1-0524), the National Science Foundation (Grant Numbers DMR-0909028 and 1410393), and STTR grant FA9550-15-C-0016, as well as the use of facilities in the LeRoy Eyring Center for Solid State Science and the John M. Cowley Center for High Resolution Electron Microscopy at Arizona State University.

TABLE OF CONTENTS

Page

CHAPTER Page

LIST OF TABLES

LIST OF FIGURES

Figure Page

Figure Page

Figure Page

# 1. INTRODUCTION

For many decades since the demonstrations of the first light emitting diode [1] and semiconductor laser [2], both GaAs *p*-*n* junction devices, III-V semiconductors have been used for high performance optoelectronic device applications due to the advantageous electrical properties of high-quality crystalline material and the wide spectral range of direct bandgaps which allow III-V materials to absorb and emit light in the visible and infrared spectrum. The bandgap energies of selected III-V semiconductors are plotted as a function of the lattice constant of the crystal, see Figure 1a at low temperature and 1b at room temperature, which shows that direct bandgap III-V binary and ternary alloys (circles and solid curves respectively) span a continuous photon energy range from the low energy visible to the long-wavelength infrared [3-5]. While indirect bandgap materials (squares and dotted curves) interact less strongly with light at their bandgap energy than direct bandgap materials, their larger bandgaps are often utilized to provide one-sided injection of carriers, electrical and optical confinement, and window effects which significantly improve the performance of modern optoelectronic devices [6,7]. Although the ternary alloys presented cover a continuous spectral range, only a handful of these compositions can be grown with high epitaxial quality due to the lack of commonly available lattice-matched substrates (indicated with vertical dashed lines) at every lattice constant. The main challenge to optoelectronic device designers has always been in finding materials with appropriate bandgaps (and band offsets) for the desired application, which also have lattice constants near those of commercially available substrates (GaAs, InP, GaSb, etc.), or in managing the lattice strain when the materials have different lattice constants.

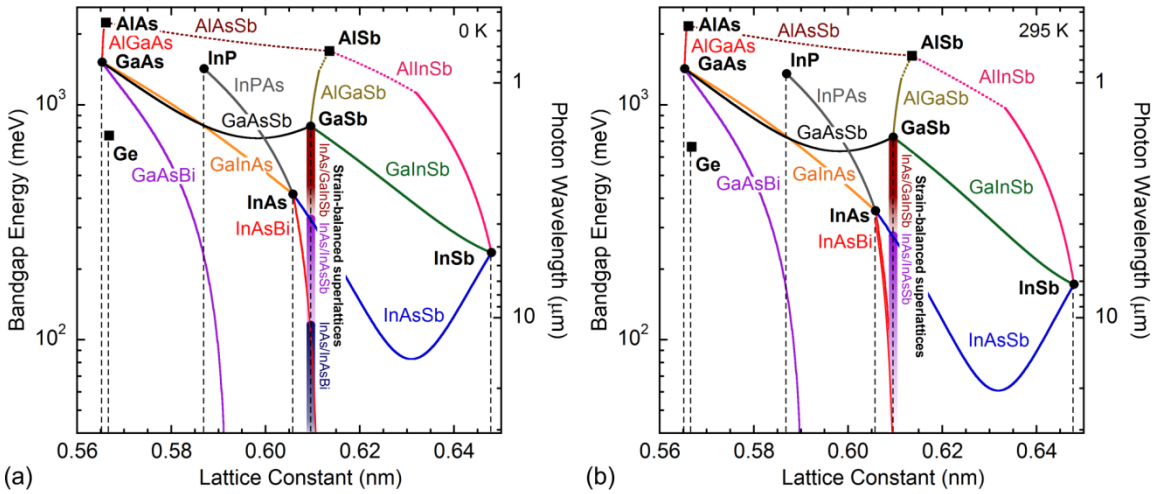


Figure 1: Bandgap energy as a function of the lattice constant of III-V; (a) low temperature and (b) room temperature, with the lattice constants of common binary substrates indicated with vertical dashed lines. Direct bandgap binary and ternary alloys are indicated with circles and solid curves, while indirect bandgap materials are indicated with squares and dotted curves. Strain-balanced InAs/GaInSb, InAs/InAsSb, and InAs/InAsBi are superlattice systems which can be grown arbitrarily thick on GaSb substrates and cover a large portion of the infrared spectrum.

Efficient detection in the infrared is desirable for a variety of commercial, military, and academic applications including gas detection, thermal imaging, and infrared spectroscopy, with each application having great need for precisely-tunable high-performance devices. The ternary alloy InAsSb (blue curve, Figure 1) spans the technologically important 3 to 5 and 8 to 12 μm atmospheric windows, however no conventional substrates exist with lattice constants at the longest wavelength InAsSb compositions. As a result, the thickness of a strained InAsSb layer, or any strained layer for that matter, must be limited so that the strain in the layer can be accommodated without lattice relaxation, otherwise the layer must be allowed to relax through the

formation of lattice defects [8]. In the first case, limiting the strained layer thickness is a design constraint that may be very difficult to contend with if the layer is too thin to absorb an adequate amount of light to overcome noise or functionalize the device. In the second case, the defects in the layer can establish electronic states in the bandgap which introduce an additional dark current generation mechanism thereby increasing the shot noise in the detector or sufficiently degrading the device beyond operability. In either case, the signal to noise ratio will be lower than it could have been had the layer been grown at its optimal design thickness without lattice defects.

Alternatively, the ternary alloy InAsBi (red curve, Figure 1) provides another possible means of reaching longer wavelengths. Photoluminescence measurements of bulk InAsBi samples grown by metalorganic vapor phase epitaxy indicate that the bandgap energy of InAsBi decreases at a rate of 42 to 55 meV/% Bi [9,10], and Bi mole fractions as large as 6.4% (nearly lattice-matched to GaSb) have been achieved using molecular beam epitaxy [11,12]. However just as with InAsSb, ternary InAsBi provides relatively little bandgap engineering flexibility due to the constraint that high quality material needs to be closely lattice-matched, drastically limiting the range of mole fractions that can be grown dislocation free on an InAs or GaSb substrate. An additional degree of design freedom is necessary to simultaneously select the bandgap energy and lattice constant; this can be achieved using a quaternary alloy or by engineering the band structure using a superlattice [13].

Strain-balanced InAs/InAsSb superlattices [14] offer access to the mid- to long-wavelength infrared region using a ternary material system at the GaSb lattice constant,

providing the benefits of low defect pseudomorphic growth on a commercially-available binary substrate. High quality InAs/InAsSb superlattices have already been demonstrated with lifetimes as long as 412 ns [15] and 9 μs [16] at 77 K, and 850 ns [16] at 250 K, and it is predicted that a lifetime of 350 ns is all that is required for an infrared photodetector to achieve background-limited operation [17]. The effective bandgap of the strain-balanced InAs/InAsSb superlattice is shown as a vertical purple line at the GaSb lattice constant in Figure 1. Whereas the bandgaps of ternary bulk materials are adjusted via the alloy mole fraction which induces strain, the effective bandgap of the strain-balanced superlattice is adjusted using the InAsSb layer mole fraction and the superlattice period thickness. In the superlattice, strain is managed by compensating the tensile strain of the InAs layers with the compressive strain of the $InAs_{1-x}Sb_x$ layers (compressive for $x > 0.089$), thereby allowing the superlattice region to be grown arbitrarily thick at the substrate lattice constant without lattice relaxation [18]. However, in general, reducing the effective bandgap of a superlattice also reduces its absorption coefficient [19]. This aspect of the superlattice is represented by the dark-to-light color gradients in the strain-balanced InAs/InAsSb, InAs/GaInSb, and InAs/InAsBi superlattice design lines in Figure 1, and represents a characteristic of the superlattice that can be optimized to identify the best performing material systems across the infrared and beyond.

In addition to design optimization, the performance of both bulk and superlattice materials can be enhanced by improving the optical quality of the material itself with the use of surfactants during molecular beam epitaxy growth [20,21]. A surfactant is an elemental or molecular species present on the surface of the material during growth that modifies the growth kinetics. Sb and Bi have been used as surfactants to decrease surface

roughness and increase photoluminescence intensity and carrier mobility in n-AlGaAs [22,23], and improving N-incorporation, photoluminescence intensity, and surface morphology in GaAsN [24,25]. Both Sb and Bi are suitable surfactants for arsenides as the typical growth temperatures are sufficiently high that little Sb or Bi incorporates into the growing film, and the trace amounts that do are isoelectronic with As. Likewise, Bi is a suitable surfactant for antimonides such as bulk InAsSb or the InAs/InAsSb superlattice.

In this work, the growth of high quality InAsBi layers and the optical properties of bulk and quantum well InAsBi are discussed in Chapters 2 and 3. The band offsets and absorption properties of InAs/InAsSb superlattices are discussed in Chapter 4. A key conclusion of Chapter 4 is that the absorption coefficient of the superlattice is proportional to the square of the electron-hole wavefunction overlap, and this relationship is used to identify superlattice designs that maximize absorption across the infrared in Chapter 5. Improvement to the optical quality of strain-balanced InAs/InAsSb superlattices achieved through the use of Bi as a surfactant is discussed in Chapter 6.

## 2. GROWTH OF DROPLET-FREE LATTICE-MATCHED *InAsBi*

Incorporating of Bi into InAs produces a ternary III-V alloy system near the 0.61 nm lattice constant which covers the technologically important mid- to long-wavelength infrared region. One challenge for this material system is that it is not straightforward to incorporate Bi into the bulk InAs lattice, since Bi has a tendency to surface-segregate and form droplets during growth. Molecular beam epitaxy growth conditions for InAsBi are explored, and a growth window is identified (temperatures $> 260$ °C, V/III flux ratios $0.98 < \text{As/In} < 1.02$ and $\text{Bi/In} \cong 0.065$) for droplet-free, high-quality crystalline material where Bi mole fractions of up to 6.4% (nearly lattice-matched to GaSb) are obtained.

### 2.1 Advantages of III-V-Bi Alloys

Alloying semiconductor materials provides additional degrees of freedom to engineer the bandgap energy and band offsets for electronic and optoelectronic device applications. For example, when GaAs is alloyed with Bi, the bandgap reduction comes primarily from the upward shift of the heavy hole and light hole bands due to the close proximity of the Bi impurity state to the GaAs valence band, while the split-off hole and conduction bands are only weakly affected [26]. Large bandgap reduction rates that vary with mole fraction are reported for $GaAs_{1-x}Bi_x$; 90 meV/% Bi at $x = 0.01$, 57 meV/% Bi at $x = 0.05$, and 43 meV/% Bi at $x = 0.10$ [27], 83 meV/% Bi for $x = 0$ - 0.036 [28], and 62 meV/% Bi for $x = 0.02 – 0.08$ [29]. The band anticrossing model is commonly used to

characterize the bandgap reduction as a function of Bi mole fraction [30]. Within the model, the bandgap reduction associated with Bi alloying in GaAs (69 meV/% Bi at $x = 0$) is significantly larger than for Sb (21 meV/% [3]) or In (16 meV/% In [3]); see Table 1. Adjusting the material's bandgap energies for strain on a GaAs substrate, the respective bandgap reduction rates become 63 meV/% Bi, 17 meV/% Sb, and 12 meV/% In. Moreover, for 1% mole fraction of In, Sb, or Bi in GaAs, the induced strain is -0.07%, -0.08%, or -0.12% in each respective alloy. As the strain introduced by the incorporation of Bi is not significantly larger than for In or Sb, a greater bandgap reduction rate per unit strain is obtained using Bi (526 meV/% strain) than for In (170 meV/% strain) or Sb (222 meV/% strain). This large bandgap reduction per unit strain is highly favorable for quantum well and strain-balanced superlattice applications, and is characteristic of III-V-Bi materials.

Table 1. Bandgap reduction rates per unit mole fraction and per unit strain for GaInAs, GaAsSb, and GaAsBi on GaAs at low temperature.

| Material | Bandgap reduction per unit mole fraction (dilute $x$) | | Layer strain for $x = 0.01$ (%) | Bandgap reduction per unit strain (meV/% strain) |
|---|---|---|---|---|
| | Unstrained (meV/%) | Strained (meV/%) | | |
| $Ga_{1-x}In_xAs$ | 16 | 12 | -0.07% | 170 |
| $GaAs_{1-x}Sb_x$ | 21 | 17 | -0.08% | 222 |
| $GaAs_{1-x}Bi_x$ | 69 | 63 | -0.12% | 526 |

For longer wavelength applications, InAs can be alloyed with Sb or Bi and devices can be designed on either the InAs or nearby GaSb substrate to obtain greater flexibility to manage the strain. For example, $InAs_{0.911}Sb_{0.089}$ is lattice-matched to GaSb with a low temperature bandgap energy of 325 meV (3.8 μm wavelength) [4], and larger Sb mole fractions can be utilized to reach smaller effective bandgaps in the 8 to 12 μm wavelength region using the strain-balanced InAs/InAsSb superlattice [14,19]. Likewise, $InAs_{0.932}Bi_{0.068}$ is lattice-matched to GaSb with a low temperature bandgap energy of 118 meV (10.5 μm wavelength), and as a result large mole fractions of Bi are not necessary to reach long wavelengths. In fact, with a bandgap reduction rate of 55 meV/% Bi [10], InAsBi can effectively cover the 3 to 5 μm mid-wave infrared region when grown on InAs and can cover the 8 to 12 μm long-wave infrared region when grown on GaSb, and in both cases can do so with very little induced strain. As a result, InAsBi-based optoelectronic devices are uniquely capable of reaching mid- and long-wave infrared wavelengths, down to zero bandgap and even semimetallic transitions, with virtually no design constraints due to strain.

## 2.2 Flux Calibrations for Molecular Beam Epitaxy Growth of InAsBi

Bi is a difficult element to incorporate into III-V alloys because it surface segregates and evaporates from the surface at the typical III-V growth temperatures of 400 to 700 °C, and it forms surface droplets when the growth temperature is reduced below 400 °C. Significant Bi incorporation occurs when low growth temperatures (~300 °C) and near-stoichiometric group-V fluxes are utilized, and thus accurate

calibration of these fluxes is critically important. The In-flux is accurately determined from the period thickness of strain-balanced InAs/InAsSb superlattices measured by X-ray diffraction. The Bi/In flux ratio is calibrated using cross-sectional scanning electron micrographs of a calibration structure, and the As/In flux ratio is calibrated using reflection high-energy electron diffraction during the growth of InAs.

The Bi-flux is determined using the calibration sample structure shown in Figure 2. At a growth temperature of 590°C, 200 nm of GaAs is grown between 10 nm thick AlAs marker layers, and the entire structure is capped with 20 nm of GaAs. The substrate is then cooled to 100°C to ensure that there is no evaporation of the Bi layer that follows. The Bi layer is grown for an amount of time which is estimated to produce a 200 nm thick layer of Bi, after which the sample is cleaved and the cross-section is examined using a scanning electron microscope detecting backscattered electrons to obtain high atomic mass contrast. The thickness of the Bi layer is determined with respect to the 200 nm thick GaAs layer, which is easily identified by the high greyscale contrast provided by the AlAs markers. The Bi-flux is determined by dividing the product of the atomic density of Bi ($\rho_{\mathrm{Bi}} = 2.82\times10^{22}$ cm$^{-3}$ [31]) and the measured Bi layer thickness ($d_{Bi}$) by the deposition time ($t_{Bi}$); see Equation 1. Dividing the Bi-flux by the In-flux yields the Bi/In flux ratio which can easily be scaled by increasing or decreasing the relative Bi-flux measured using the flux gauge inside the molecular beam epitaxy system.

$$\text{Bi-flux} = \frac{\rho_{\mathrm{Bi}} \times d_{Bi}}{t_{Bi}} \tag{1}$$

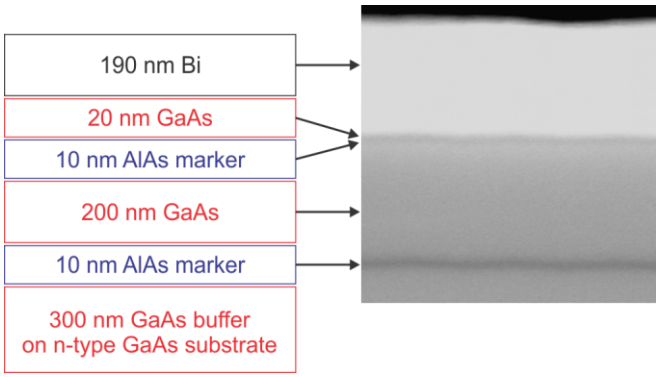


Figure 2: Bi-flux calibration sample structure (left) alongside the electron micrograph of the sample cross-section (right) used to measure the Bi layer thickness with respect to the accurately calibrated 200 nm thick GaAs layer for the determination of the Bi-flux.

Whereas the Bi/In flux ratio is uniform across the 75 mm GaAs substrate used for the calibration, the As/In flux ratio possesses a significant radial dependence. The radial profile of the As/In flux ratio shown in Figure 3 is measured/calibrated during the growth of InAs at 300°C on a 50 mm InAs substrate under rotation. The As/In flux ratio at the center of the wafer is calibrated using reflection high-energy electron diffraction. Starting with an As-overpressure, the As-flux is progressively reduced until the surface reconstruction transforms from an As-rich (2×4), to a (1×1), to an In-rich (4×2) [32]; the transitional (1×1) surface reconstruction indicates that the As/In flux ratio is unity at the center of the wafer where the electron diffraction takes place. The radial profile is determined during growth under rotation, starting with unity As/In flux at the wafer center and incrementally reducing the As-flux in 1% steps. As the As-flux is reduced, distinct concentric rings of rough growth develop due to the formation of In-droplets on the In-rich growth surfaces seen in the inset of Figure 3. The As/In flux ratio in the

center region of the wafer is relatively constant, but increases by approximately 4% from a radius of 10 mm to the edge of a 50 mm diameter (25 mm radius) wafer. The non-uniformity of the As/In flux ratio is mainly due to a ~3% decrease in the In-flux moving radially from the center to the edge of the wafer.

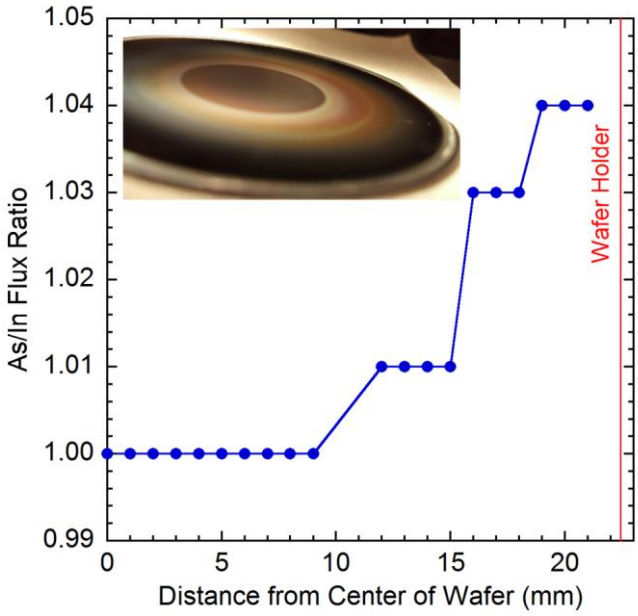


Figure 3: Radial profile of the As/In flux ratio (under rotation) measured during the growth of InAs at 300 °C on the 50 mm InAs wafer seen in the figure inset. The unity flux ratio is given at the center of the wafer by the (1×1) surface reconstruction (measured by reflection high-energy electron diffraction) and the radial profile is determined by further reducing the As-flux in 1% increments, which results in the formation of concentric haze rings across the wafer as In-droplets form in regions deficient in As (see photograph in inset).

This small non-uniformity in the As/In flux ratio has little impact on the growth of most arsenide materials that are grown with As/III flux ratios greater than unity, however 4% is very significant when the fluxes are near-stoichiometric as is the case for the growth of arsenide-bismide materials. In the following experiments, InAsBi is grown with a target As/In flux ratio at the center of each wafer keeping in mind the change of the As/In flux ratio across the wafer. By keeping track of the As/In flux ratio and characterizing the InAsBi radially across the wafer, continuous ranges of growth conditions are studied on single 50 mm wafers.

## 2.3 Growth of High-Quality Droplet-Free InAsBi on GaSb

Bulk InAsBi layers are grown by molecular beam epitaxy on ¼ 50 mm and full 50 mm Zn-doped GaSb substrates at temperatures ranging from 260 to 300 °C, calibrated using an infrared pyrometer [33]. The As/In flux ratio is uniform to within 1% for growths on ¼ wafers, and varies by 4% for growths on full 50 mm wafers with the radial profile shown in Figure 3. The bulk InAsBi samples consist of a 500 nm thick GaSb buffer, a 15 nm thick InAs spacer (samples a - e), and a 1 μm thick InAsBi layer; the entire structure is capped with a 10 nm thick InAs layer (samples a - e), a 10 nm thick GaSb layer (sample h), or left uncapped (samples f and g). The growth conditions and Bi mole fractions of each sample are summarized in Table 2.

Table 2. Growth conditions and Bi mole fractions measured using X-ray diffraction for 1 μm thick InAsBi samples grown on ¼ or full 50 mm GaSb substrates.

| Sample | Substrate (¼ or full 50 mm GaSb) | Growth temp. (°C) | Bi/In flux ratio | As/In flux ratio (center) | Bi mole fraction | As/In flux ratio (at point of X-ray diffraction measurement) |
|---|---|---|---|---|---|---|
| a | full | 280 | 0.065 | 0.96 | 0.064 | 0.98 – 0.99 |
| b | full | 270 | 0.065 | 0.96 | 0.062 | 0.99 – 1.00 |
| c | full | 260 | 0.065 | 1.00 | 0.060 | 1.03 – 1.04 |
| d | full | 270 | 0.065 | 1.00 | 0.059 | 1.00 – 1.02 |
| e | full | 280 | 0.060 | 1.00 | 0.057 | 1.00 – 1.03 |
| f | ¼ | 280 | 0.060 | 1.00 | 0.054 | 1.00 |
| g | ¼ | 280 | 0.060 | 1.05 | 0.051 | 1.05 |
| h | ¼ | 300 | 0.100 | 1.50 | 0.003 | 1.50 |

All growths are performed using a constant In-flux of $2.73\times10^{14}$ atoms $cm^{-2}\cdot s^{-1}$ that corresponds to an InAs on InAs growth rate of about 0.5 monolayers per second. This flux corresponds to growth rates of 9.10 nm per minute for InAs on InAs, 9.15 nm per minute for InAs on GaSb, and 9.27 nm per minute for InAsBi lattice-matched to GaSb. The 9.15 nm per minute growth rate and the inferred In-flux are accurately calibrated using X-ray diffraction measurements of the period thickness of strain-balanced InAs/InAsSb superlattices grown on GaSb substrates. The InAsBi layers grown between 280 and 260 °C with V/In flux ratios greater than unity and Bi/In flux ratios of ~0.065 exhibited group-V terminated surface reconstructions: (2×3) for droplet-free growth and (2×1) for growth with Bi-droplet formation that evolves to a spotty 2× with chevrons as droplets begin to cover the surface.

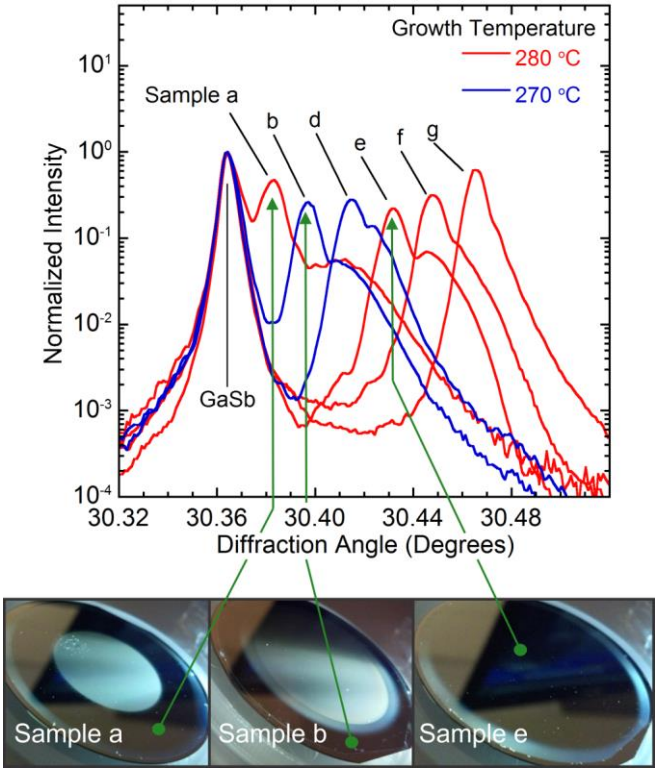


Figure 4: Plot shows coupled ω-2θ X-ray diffraction patterns from the (004)-planes of 1 μm thick InAsBi layers grown on GaSb substrates. For samples a, b, and e, the positions of the measurements are shown by the solid green lines to the photos of the sample surfaces below.

The surface and structural quality of the 1 μm thick InAsBi samples is found to be strongly dependent on the group-V fluxes, as each sample developed regions of rough and smooth growth. Photographs of samples a, b, and e are shown in Figure 4, where the rough regions are identified as droplets using Nomarski interference contrast and scanning electron microscope images. Energy-dispersive X-ray spectroscopy verifies that the droplets are composed of Bi, a result that is consistent with ω-2θ X-ray diffraction measurements of the Bi mole fraction which show that the droplet-free regions have significantly larger Bi content than the droplet-covered regions.

X-ray diffraction measurements are performed using a PANalytical X'Pert PRO Materials Research Diffractometer. The incident beam optics consist of an X-ray mirror and a 2-crystal Ge (220) 4-bounce monochromator with a 0.25 degree divergence slit and a 0.25 inch width mask which determines the width of the beam incident on the sample. The diffracted beam optics consists of a triple axis monochromator and a 0.50 degree slit placed before the detector. The plot in Figure 4 shows the coupled ω-2θ X-ray diffraction patterns measured from the (004)-planes in the smooth surface regions of the six bulk samples a, b, d, e, f, and g. The shift in the main layer peaks to lower diffraction angles, towards the GaSb substrate diffraction peak, indicates decreasing tensile strain and larger Bi mole fraction in the InAsBi layers. The Bi mole fractions provided in Table 2 are determined using the dynamical X-ray diffraction software X'pert Epitaxy [34], along with the 0.66108 nm lattice constant and 0.350 Poisson's ratio of InBi [12]. The reciprocal space maps shown in Figure 5 are performed in the vicinity of the (115)-reflection of the GaSb substrate of each sample. With decreasing Bi mole fraction, the peak separation in the growth direction reciprocal lattice (vertical axis) increases indicating increasing tensile strain in the layer. Moreover, all samples exhibit GaSb and InAsBi diffraction peaks at the same in-plane reciprocal lattice position of 2.32 $nm^{-1}$ (horizontal axis), which verifies that all of these samples are coherently strained.

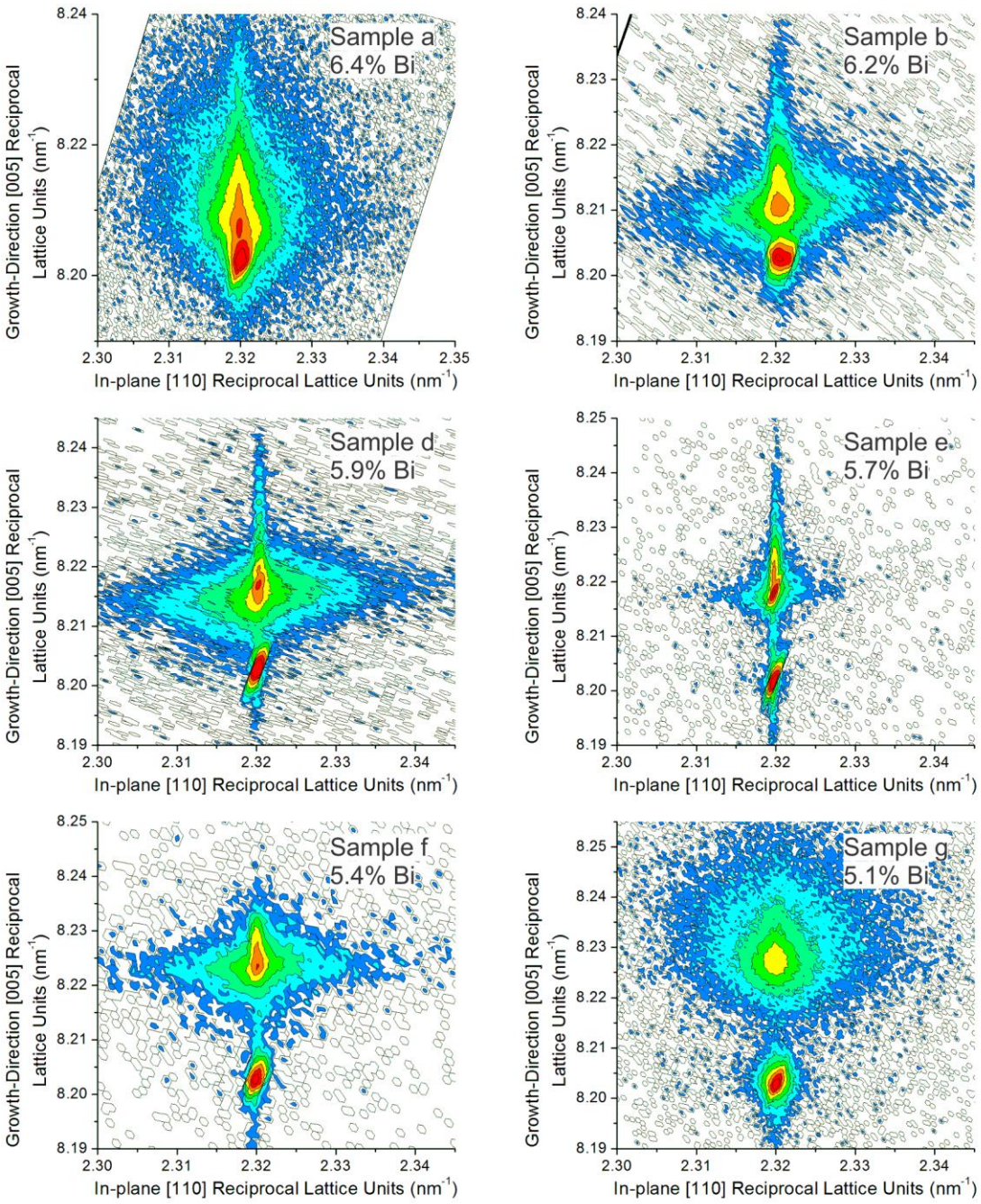


Figure 5. Reciprocal space maps in the vicinity of the (115)-reflection of the GaSb substrates of bulk InAsBi samples.

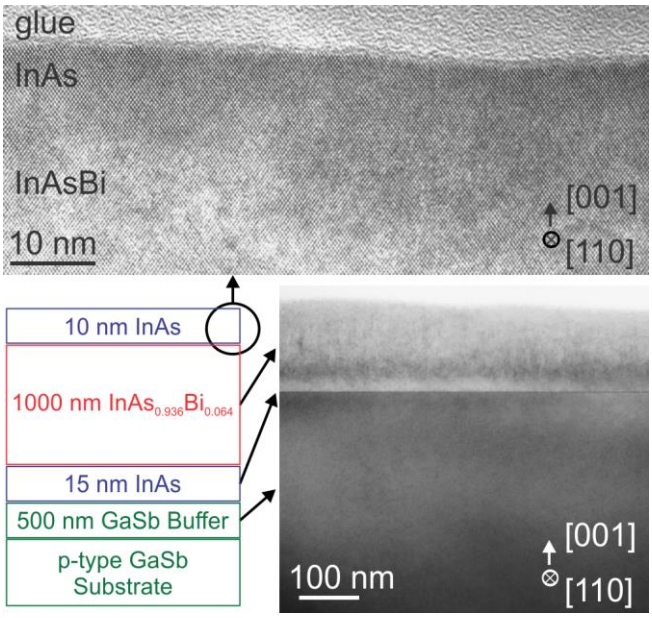


Figure 6: Cross-section electron micrographs showing nearly lattice-matched bulk $InAs_{0.936}Bi_{0.064}$ (sample a); high-resolution (upper) and bright-field (lower right), sample regions imaged are indicated on the cross-section schematic. The high-resolution image shows excellent crystallinity at the top of the InAsBi layer and InAs cap, and the bright-field image shows that the material has no visible defects over large lateral distances. **Image acquired by Jing Lu and Dr. David J. Smith at Arizona State University* [11].

Transmission electron micrographs from the smooth surface region of sample a are shown in Figure 6 where the regions imaged are indicated on the cross-section schematic. The upper micrograph is a high-resolution image that confirms excellent crystallinity at the top of the InAsBi layer and InAs cap. The lower micrograph is a bright-field image which shows that this sample has no visible defects over large lateral distances. These results indicate excellent crystal quality with few defects over many hundreds of nanometers.

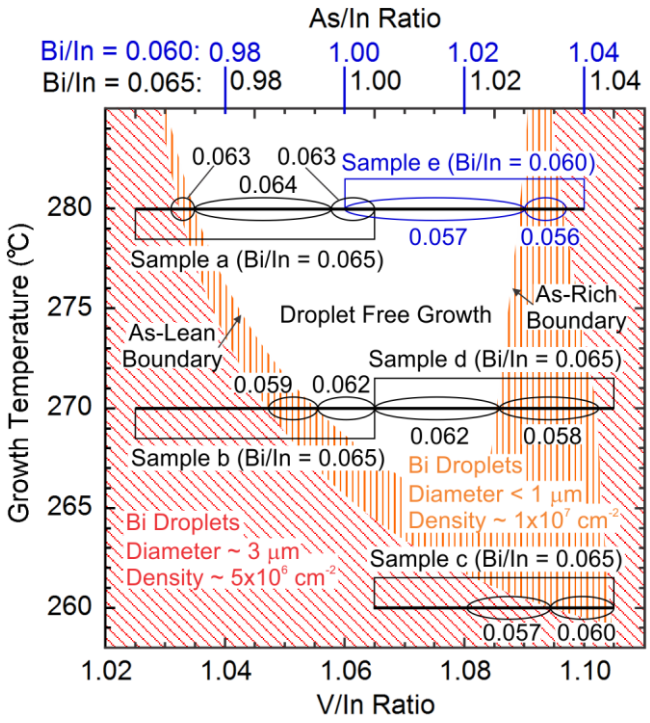


Figure 7: Growth temperature versus the V/In (As/In + Bi/In) flux ratio (lower horizontal axis) during molecular beam epitaxy growth of bulk InAsBi. The As/In flux ratio is shown on the upper horizontal axis for sample e (blue upper axis) with a Bi/In flux ratio of 0.060 and for the other samples (black upper axis) with a Bi/In flux ratio of 0.065. Three distinct growth regions are shown; droplet-free (not shaded), submicrometer diameter Bi-droplets with a density of ~$1\times10^{7}$ $cm^{-2}$ (orange vertical lines), and ~3 μm diameter Bi-droplets with a density of ~$5\times10^{6}$ $cm^{-2}$ (red diagonal lines). The growth space sampled by each growth is shown by the thick horizontal line of each rectangular area labeled by sample name. The ovals drawn along each sample region indicate the location and Bi mole fraction measured by X-ray diffraction.

The molecular beam epitaxy growth space for high-quality InAsBi is mapped in Figure 7 by plotting growth temperature versus the V/In flux ratio for the five bulk samples that were grown on full 50 mm wafers (samples a, b, c, d, and e, see Table 2). The radial locations of InAsBi growth with and without droplet formation are determined

across each of the 50 mm wafers, and the corresponding As/In flux ratios are established at each location using the As/In flux ratio profile given in Figure 3 scaled by the As/In flux ratio setting at the center of each sample. The growth space sampled by each wafer is shown by the thick horizontal line of each rectangular area labeled by sample name. The ovals drawn along each sample region indicate the location and the percentage Bi mole fraction measured by X-ray diffraction. Three distinct regions of growth are identified in the plot; droplet-free high-quality crystalline growth (not shaded), < 1 μm diameter Bi-droplets with a density of $1\times10^{7}$ $cm^{-2}$ (shaded with orange vertical lines), and 3 μm diameter Bi-droplets with a density of $5\times10^{6}$ $cm^{-2}$ (shaded with red diagonal lines).

Samples a and e are grown at 280 °C with different group-V flux conditions. Sample a is grown with a Bi/In flux ratio of 0.065 and an As/In flux ratio (black upper horizontal axis) of 0.96 at the wafer center increasing to 1.00 at the edge. This sample is very rough at the center of the wafer, having formed a dense array of 1 to 3 μm diameter droplets (see left-hand photograph in Figure 4), and abruptly becomes smooth near the point at which the As/In flux ratio is 0.97. The Bi composition in the smooth region of the sample is 0.064, indicated by the circled region on the thick horizontal line. Sample e is grown with a Bi/In flux ratio of 0.060 and an As/In flux ratio (blue upper horizontal axis) of 1.00 at the wafer center increasing to 1.04 at the edge. This sample is smooth in the wafer center (see right-hand photograph in Figure 4), with the formation of sub-micrometer sized Bi-droplets at the wafer edge. Samples b and d are grown at 270 °C with a Bi/In flux ratio of 0.065 and an As/In flux ratio of 0.96 to 1.00 (center to edge) for sample b and 1.00 to 1.04 (center to edge) for sample d, resulting in a continuous range of growth conditions at 270 °C wherein droplet-free growth occurs for 0.99 < As/In < 1.02.

Sample c is grown at 260 °C with a Bi/In flux ratio of 0.065 and an As/In flux ratio of 1.00 to 1.04 (center to edge). Under these growth conditions, Bi-droplets are formed across the entire growth surface, though the droplets within 4 mm of the edge are much smaller than those in the center.

The growths on ¼ 50 mm GaSb wafers (samples f, g, and h) are not shown in Figure 7, and due to their smaller size the As/In flux is uniform to within 1% across the samples. Sample f is grown under the same conditions as the center of the larger sample, sample e (280°C, 1.00 As/In flux ratio, and 0.060 Bi/In flux ratio) and it has a slightly smaller Bi mole fraction (0.054 compared to 0.057). Sample g has a slightly lower Bi mole fraction (0.051) compared to samples e (0.057) and f (0.054) grown at the same temperature and Bi-flux, which is consistent with the presence of a 5% larger As/In flux ratio. However, the observed Bi deficiency did not result in as many Bi-droplets as would be expected from the results presented in Figure 7. Sample h is grown at 300 °C with a 1.50 As/In flux ratio and a 0.10 Bi/In flux ratio. Under these non-stoichiometric flux conditions, only a small percentage of the Bi incorporates with most of the Bi remaining on the surface to form a dense ~$4\times10^{7}$ $cm^{-2}$ coverage of 1 µm diameter droplets. This is approximately four times more surface Bi than observed in the droplet covered regions of samples a through e which were grown with near-stoichiometric As/In flux ratios and lower Bi-fluxes. This growth (sample h) resulted in a thick, 90% relaxed, InAsBi layer with a Bi mole fraction of 0.002; the relaxation and composition are determined self consistently from the growth-direction strain of the InAsBi lattice measured by X-ray diffraction and the shift in the photoluminescence peak predicted by strain and the band anticrossing model.

## 2.4 Bi Incorporation in InAsBi

The incident and excess flux ratios and mole fractions of As and Bi at the droplet-free and small droplet boundaries of the As-lean and As-rich growth regimes are summarized in Table 3. From the point of view of the competition between Bi and As for group-V sites, it is expected that reducing the As/In flux ratio would enable further incorporation of Bi. However, as the As/In flux ratio is decreased, there is an unexpected reduction in Bi incorporation and the onset of Bi-droplet formation as the excess Bi coalesces on the surface during As-lean growth, indicating that the interaction between Bi and As also plays a significant role in the incorporation of Bi. For example (refer to Figure 7), the droplet-free boundary for As-lean growth at 280 °C occurs where the As mole fraction is 0.936, the Bi mole fraction is 0.064, the incident As/In is 0.97, and the incident Bi/In is 0.065. The excess flux ratios are the difference between the incident flux ratio and the incorporated mole fraction, hence the excess As/In is 0.034 and the excess Bi/In is 0.001. As the incident As/In flux ratio is reduced, the excess 0.001 Bi/In begins to coalesce into small droplets, until the small droplet boundary is reached at which point the excess As/In is 0.031 and the excess Bi/In of 0.002 enables the formation of substantially larger droplets. The same effects are observed in the As-lean growth boundaries at 270 °C; small droplets begin to form at the droplet-free growth boundary when the excess As/In is less than 0.052, leaving an excess Bi/In of 0.003 to initiate the formation of small droplets at 270 °C. Large droplets begin to form when the As/In is brought below 0.042 with an excess Bi/In of 0.006 at 270 °C.

Table 3. Incident and excess flux ratios and mole fractions of As and Bi at the boundaries of droplet-free InAsBi growth and small Bi-droplet formation observed in Figure 7.

| | Growth temp. (°C) | Growth boundary | As/In flux ratio | Bi/In flux ratio | As mole fraction | Bi mole fraction | Excess As/In | Excess Bi/In |
|---|---|---|---|---|---|---|---|---|
| As-Lean Growth (As/In<1) | 280 | Droplet-free | 0.970 | 0.065 | 0.936 | 0.064 | 0.034 | 0.001 |
| | | Small droplet | 0.968 | 0.065 | 0.937 | 0.063 | 0.031 | 0.002 |
| | 270 | Droplet-free | 0.990 | 0.065 | 0.938 | 0.062 | 0.052 | 0.003 |
| | | Small droplet | 0.983 | 0.065 | 0.941 | 0.059 | 0.042 | 0.006 |
| As-Rich Growth (As/In>1) | 280 | Droplet-free | 1.030 | 0.060 | 0.944 | 0.056 | 0.086 | 0.004 |
| | | Small droplet | 1.035 | 0.060 | 0.945 | 0.055 | 0.090 | 0.005 |
| | 270 | Droplet-free | 1.021 | 0.065 | 0.941 | 0.059 | 0.080 | 0.006 |
| | | Small droplet | 1.038 | 0.065 | 0.943 | 0.057 | 0.095 | 0.008 |

On the other hand, in the As-rich regime, the onset of small droplet formation occurs when the excess As/In flux exceeds 0.086 at 280°C, at which point the excess Bi/In of 0.004 begins to form small droplets on the surface. With increasing As, large droplets begin to form for excess As/In flux ratios greater than 0.090 and excess Bi/In flux ratios of 0.005. At 270°C, small droplets begin to form at excess As/In and Bi/In flux ratios of 0.080 and 0.006, and large droplets begin to form at excess As/In and Bi/In flux ratios of 0.095 and 0.008. Comparing the excess flux ratios across the full range of incident As/In flux ratios, the droplet-free growth window can be defined for excess flux ratios ranging from $0.034 < As/In < 0.086$ at 280 °C, $0.052 < As/In < 0.080$ at 270 °C, and temperatures not less than 270 °C.

These results indicate that the incorporation of Bi is strongly affected by its interaction with As on the growth surface, where an optimal amount of As results in the maximum amount of Bi incorporation without the formation of Bi-droplets. The presence of too little or too much As reduces the incorporation of Bi. It seems that under the appropriate concentration, As on the growth surface behaves like a reactive surfactant enhancing the incorporation of Bi during the growth of InAsBi, much like Te does for In during the growth of GaInAs [35] or the growth of binaries such as GaAs [36,37]. When the As-flux is decreased below a critical level, excess As/In < 3-5%), excess Bi on the surface coalesces forming droplets as less Bi is incorporated into the growing InAsBi film via the As-Bi interaction. Likewise, when the As-flux is increased above a critical level, excess As/In > 8-9%, excess Bi on the surface coalesces forming droplets as less Bi is incorporated into the growing InAsBi film via the As-Bi interaction. In the former

case, there is not enough As on the surface to react with all of the Bi and in the latter case the interaction of As with itself overwhelms its interaction with Bi.

## 2.5 Chapter 2 Summary

The substrate temperatures and flux conditions for the molecular beam epitaxy growth of smooth, high quality, nearly lattice-matched InAsBi on GaSb substrates without the formation of Bi-droplets are identified as temperatures $> 260$ °C and $0.98 < \text{As/In} < 1.02$ with $\text{Bi/In} \cong 0.065$. The maximum incorporation of Bi occurs in this growth window, where Bi mole fractions up to 0.064 are obtained. Outside this growth window, less Bi incorporates and the excess Bi coalesces into surface-droplets.

# 3. OPTICAL PROPERTIES OF *InAsBi*

A number of high-quality dilute bismide InAs/InAsBi/InAs quantum wells and nearly lattice-matched InAsBi bulk layers with Bi mole fractions ranging from 0.051 to 0.064 are grown on GaSb substrates using molecular beam epitaxy. The room temperature refractive index and absorption coefficient of bulk InAsBi are measured using spectroscopic ellipsometry, and the bandgap energy as a function of Bi mole fraction is fit using the band anticrossing model. The optical properties of the quantum wells are assessed using temperature and excitation dependent photoluminescence spectroscopy. Detailed analysis of the photoluminescence shows that the photogenerated carriers recombine radiatively in the InAs/InAsBi quantum wells, indicating good internal quantum efficiency, and the temperature dependence of the InAsBi bandgap energy is accurately described using the Einstein single oscillator.

## 3.1 Spectroscopic Ellipsometry of Bulk InAsBi

The bandgap and absorption properties of InAsBi are determined from a 930 nm thick layer of bulk $InAs_{0.936}Bi_{0.064}$ (sample a, see Table 2) grown by molecular beam epitaxy on a (100)-oriented 50 mm GaSb substrate [11,12]. The sample structure consists of a 500 nm thick GaSb buffer, a 13.95 nm thick InAs layer, a 930 nm thick $InAs_{0.936}Bi_{0.064}$ layer, and a 9.30 nm thick InAs cap, and is shown in Figure 8. This layer structure differs from the nominal cross section described in Section 2.3 only in that the InAsBi and InAs layer thicknesses have been corrected to reflect the actual InAs growth rate inferred from the 930 nm thick InAsBi layer [12].

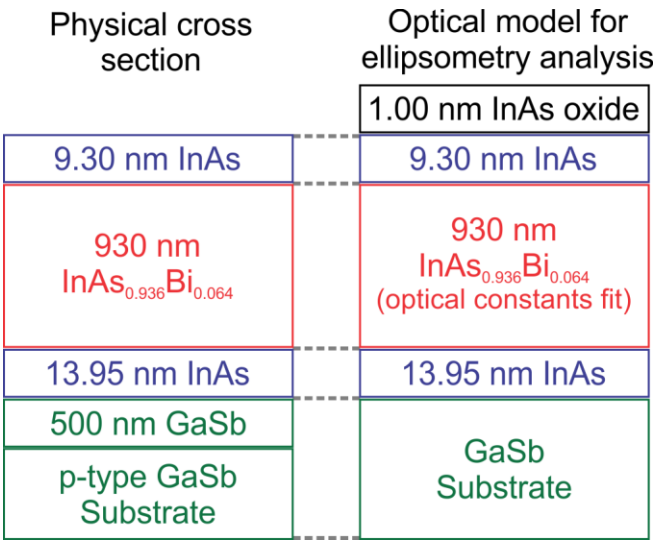


Figure 8. Bulk InAsBi sample cross section (left) alongside the optical model used for ellipsometry analysis (right) in which the optical constants of the 930 nm thick $InAs_{0.936}Bi_{0.064}$ layer are fit to the measured ellipsometric parameters.

The optical properties of the $InAs_{0.936}Bi_{0.064}$ layer are measured by spectroscopic ellipsometry using VASE and IR-VASE model spectroscopic ellipsometers to respectively cover the ultraviolet to near infrared and the near infrared to long wavelength infrared spectral ranges [38]. The ellipsometric parameters $\Psi$ and $\Delta$ are measured at 64, 68, 72, and 76, degrees; combining the angle data measured by the two ellipsometers, the ellipsometric parameters are obtained for photon energies ranging from 44 meV to 4.4 eV (28.2 to 0.282 μm wavelength). The depolarization of the measured reflection is reduced below 2% for all photon energies by roughing the backside of the semi-transparent GaSb wafer with 400 grit sandpaper prior to the measurement. The backside roughing procedure used is described in Appendix A.

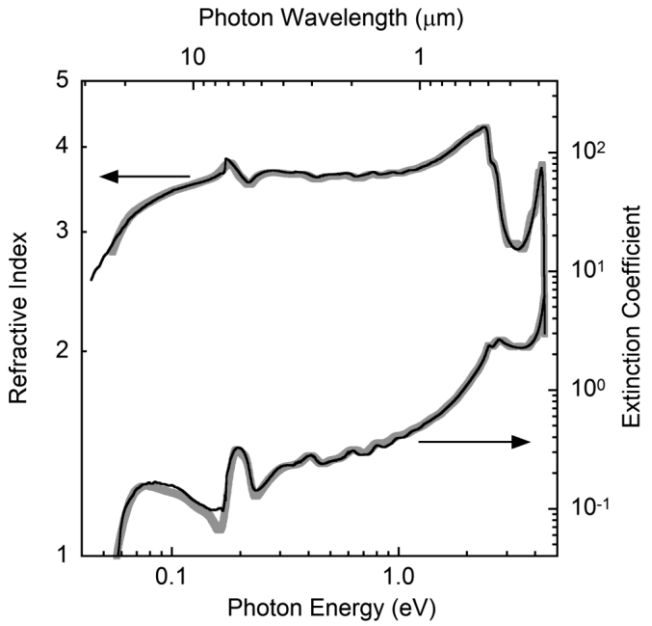


Figure 9. Refractive index (left-hand vertical axis) and extinction coefficient (right-hand vertical axis) of bulk $InAs_{0.936}Bi_{0.064}$ plotted as a function of photon energy (lower horizontal axis) and photon wavelength (upper horizontal axis). The optical constants identified using point-by-point and oscillator fitting analyses are shown with black and grey curves respectively.

The ellipsometric optical model of the sample is shown schematically alongside the physical cross section in Figure 8. The WVASE software library [39] provides the optical constants of the GaSb, InAs, and InAs native oxide layers, and the optical constants of the InAsBi layer are fit using a point-by-point (wavelength-by-wavelength) analysis method [40]. The value of using the point-by-point analysis is that it results in the actual measured optical constants unmodified by any particular fitting or smoothing model such as the general oscillator model and its various functional forms. The point-by-point refractive index $n$ (left-hand vertical axis) and extinction coefficient $k$ (right-hand vertical axis) are plotted as a function of photon energy $hv$ (lower horizontal axis)

and photon wavelength $\lambda$ (upper horizontal axis) in Figure 9 (black curves). In addition, an oscillator model [39,40] composed of a PSEMI0 oscillator at the bandgap and Gaussian oscillators above the bandgap is also fit to the data producing the grey curves in Figure 9. The value of the oscillator model analysis is that it enforces Kramers-Kronig consistency [41-43], and therefore shows that the point-by-point fitted optical constants are also Kramers-Kronig consistent.

The absorption coefficient $\alpha = 4\pi k/\lambda$ shown in Figure 10 is determined using the point-by-point fitted extinction coefficient ($k$) in Figure 9. The figure inset shows the absorption coefficient in the range of 50 to 100 meV (black curve) and its first derivative (grey curve). The position of the first derivative maximum identifies the tensilely strained $InAs_{0.936}Bi_{0.064}$ bandgap energy of 60 meV with an absorption coefficient of 503 $cm^{-1}$.

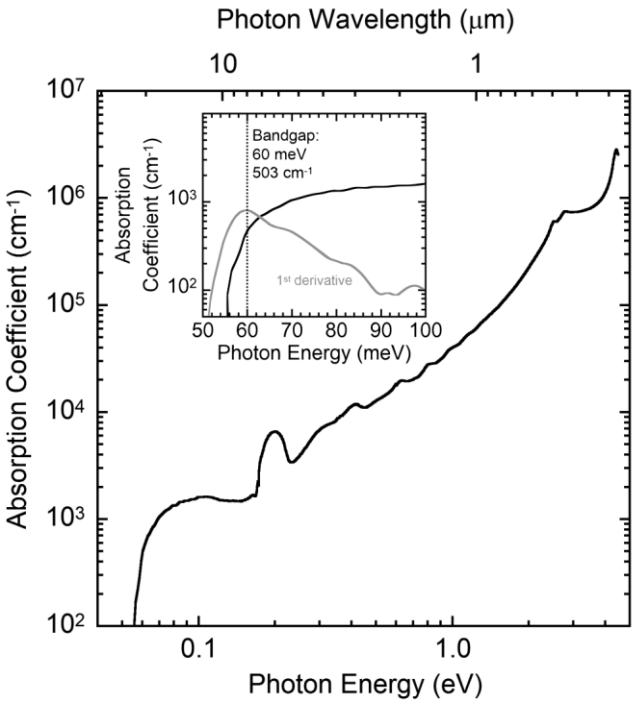


Figure 10. Absorption coefficient of $InAs_{0.936}Bi_{0.064}$ plotted as a function of photon energy (lower horizontal axis) and photon wavelength (upper horizontal axis). Inset shows the absorption coefficient in the range of 50 to 100 meV (black curve) as well as its first derivative as a function of energy (grey curve) which is used to determine the bandgap energy of nearly lattice-matched $InAs_{0.936}Bi_{0.064}$ at 60 meV.

## 3.2 Band Anticrossing in InAsBi

The valence band edge of InAsBi is expressed as a function of Bi mole fraction $x$ using the valence band anticrossing model [30,44] in Equation 2. In the equation, $E_v(x)$ is the position of the InAsBi valence band edge relative to the InAs valence band edge, $\Delta E_v$ is the energy separation between the InBi and InAs valence band edges, $E_{Bi}$ is the energy of the Bi impurity state relative to the InAs valence band edge, and $C_{Bi}$ is the coupling parameter that characterizes the strength of the band anticrossing interaction.

Physically, the quantity inside the first set of square brackets represents the valence band anticrossing interaction which dominates in the As-rich mole fraction regime, while the quantity in the second set of square brackets represents the linear variation in the valence band which is assumed to dominate in the Bi-rich mole fraction regime as has been observed experimentally in GaAsSb [30] and InAsSb [45] and is similarly assumed for GaAsBi [30]. Reciprocally, As may be expected to produce an anticrossing interaction in the conduction band in the Bi-rich regime [30,45], however as Bi-rich mole fraction InAsBi has not been synthesized, the conduction band edge is assumed to vary linearly with mole fraction between the conduction band edges of InAs and InBi.

$$E_v(x) = \left[\frac{(\Delta E_v \cdot x) + E_{Bi} + \sqrt{\left((\Delta E_v \cdot x) - E_{Bi}\right)^2 + (2C_{Bi})^2 \cdot x}}{2}\right](1-x) + [\Delta E_v \cdot x]x \qquad (2)$$

The valence band edge of InBi is predicted by linearly extrapolating from the valence band edges of InP, InAs, and InSb as a function of lattice constant [3] in Figure 11a, from which the energy separation between the InBi and InAs valence band edges, $\Delta E_v$, of 0.80 eV is identified at the 0.66108 nm lattice constant of InBi [12]. Also shown in the figure are the valence band edges of Ga-V (Figure 11b) and Al-V binaries (Figure 11c) from which the valence band edges of GaBi and AlBi are also predicted. The conduction band edge of InBi is specified by the InBi valence band edge plus the -1.63 eV bandgap energy of InBi calculated using density functional theory [26]. The Bi impurity state is located 0.4 eV below the valence band edge of GaAs [30] which is itself located 0.21 eV below the valence band edge of InAs [3], therefore the energy of the Bi impurity state relative to the InAs valence band edge, $E_{Bi}$, is -0.61 eV.

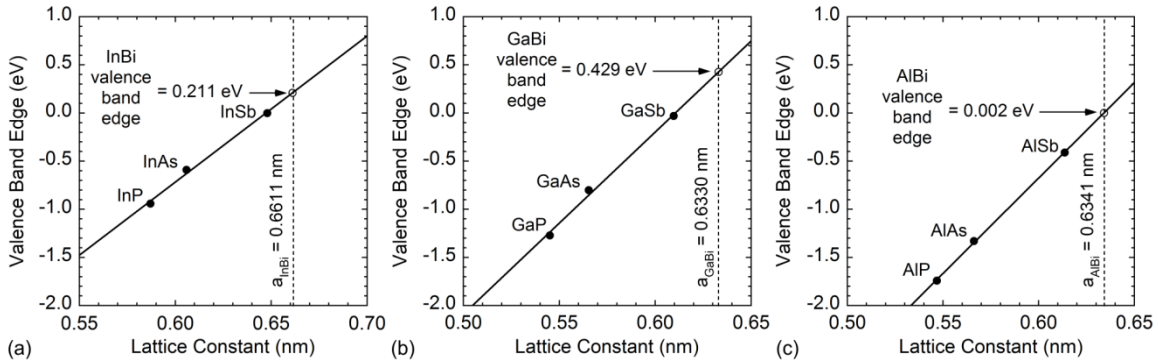


Figure 11. Valence band edges of conventional III-V binary semiconductors (solid circles) plotted as a function of lattice constant, (a) InP, InAs, and InSb, (b) GaP, GaAs, and GaSb, and (c) AlP, AlAs, and AlSb. The solid lines are linear fits to the data which are used to predict the valence band edges of InBi, GaBi, and AlBi (open circles).

When InAsBi is grown pseudomorphically on GaSb as is the case for the bulk $InAs_{0.936}Bi_{0.064}$ layer examined in Section 3.1, strain modifies the conduction and valence band edge positions of the material. The band anticrossing model characterizes the band edge positions of unstrained material; therefore the coupling parameter $C_{Bi}$ in Equation 2 is fit using the unstrained $InAs_{0.936}Bi_{0.064}$ bandgap specified by the 60 meV strained bandgap measured in Section 3.1 plus 0.6 meV due to the 0.036% tensile strain in the layer. The 0.6 meV strain offset is calculated using the Pikus-Bir Hamiltonian [46,47], the deformation potentials of InAs [3], and a composition-dependent Poisson's ratio which varies linearly with mole fraction between Poisson's ratio of InAs (0.352) and InBi (0.350) [3,12].

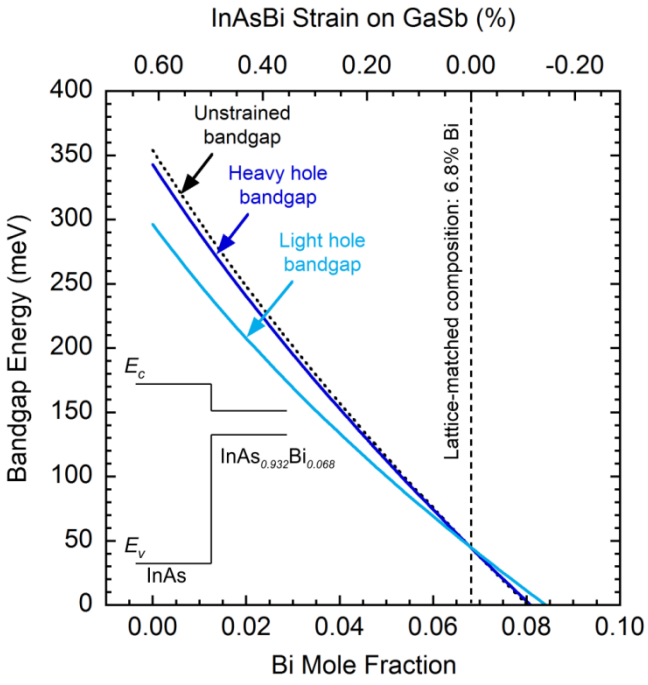


Figure 12. Room temperature bandgap energy of InAsBi plotted as a function of Bi mole fraction (lower horizontal axis). The dotted black curve shows the unstrained bandgap and the solid light and dark blue curves show the light and heavy hole bandgaps of coherently strained InAsBi on GaSb. The corresponding strain is shown on the upper horizontal axis. The inset shows the conduction and valence band edge positions ($E_c$ and $E_v$) of tensilely strained InAs and lattice-matched $InAs_{0.932}Bi_{0.068}$ on GaSb.

The $InAs_{1-x}Bi_x$ bandgap energy as a function of Bi mole fraction is computed using the valence band anticrossing model and the Bi coupling parameter and other parameters given in Tables 4 and 5. The unstrained bandgap shown by the dotted black curve in Figure 12 is plotted as a function of Bi mole fraction on the lower horizontal axis. Over the range of 0 to 3% Bi mole fraction, the average linear bandgap reduction rate per unit mole fraction is 50.7 meV/% Bi, which lies between the rates of 42 and 55 meV/% Bi reported over the same range of mole fractions [9,10]. When this material

is coherently strained to GaSb (upper horizontal axis), the light and heavy hole bands split producing the light hole (solid light blue curve) and heavy hole (solid dark blue curve) bandgaps. InAsBi is perfectly lattice-matched to GaSb at 6.8% Bi mole fraction with the conduction and valence band edge positions ($E_c$ and $E_v$) shown in the figure inset, and becomes semimetallic at 8.0% Bi mole fraction at room temperature. For the strained material, the bandgap reduction rate is 42.4 meV/% Bi over the same range of mole fractions (0 to 3% Bi) and is even greater (50.0 meV/% Bi) for dilute Bi mole fractions.

Table 4. InAsBi valence band anticrossing parameters.

| Parameter | Value |
|---|---|
| Energy separation between the InAs and InBi valence band edges, $\Delta E_v$ | 0.80 eV |
| Bi impurity level, $E_{Bi}$ | -0.61 eV |
| Bi coupling parameter, $C_{Bi}$ | 1.529 eV |

Table 5. Physical and band structure parameters of InAs and InBi.

| Parameter | Value | |
|---|---|---|
| | InAs | InBi |
| Valence band edge | -0.59 eV | 0.21 eV |
| 0 K bandgap energy | 0.417 eV | -1.63 eV |
| 295 K bandgap energy | 0.354 eV | -1.63 eV |
| Lattice constant | 0.60583 nm | 0.66108 nm |
| Poisson's ratio | 0.352 | 0.350 |
| Conduction band deformation potential | -5.08 eV | -5.08 eV |
| Valence band deformation potential | -1.00 eV | -1.00 eV |
| Shear deformation potential | -1.80 eV | -1.80 eV |
| Electron effective mass | 0.026 | 0.026 |
| Heavy hole effective mass | 0.333 | 0.333 |

## 3.3 Growth of InAs/InAsBi Quantum Wells

Two dilute bismide InAs/InAsBi quantum wells are grown using molecular beam epitaxy on (100)-oriented GaSb substrates. The quantum well consists of a 10 nm thick layer of InAsBi sandwiched between 50 nm thick InAs layers which are all grown at a rate of 0.5 monolayers per second at 300 °C using a 0.021 Bi/In flux ratio. The InAs/InAsBi/InAs active region is itself sandwiched between 10 nm thick AlSb layers which provide confinement to photogenerated carriers, and the entire structure is capped with 10 nm of GaSb to prevent oxidation of the upper AlSb layer. The cross section schematic of the quantum well structure is shown in Figure 13.

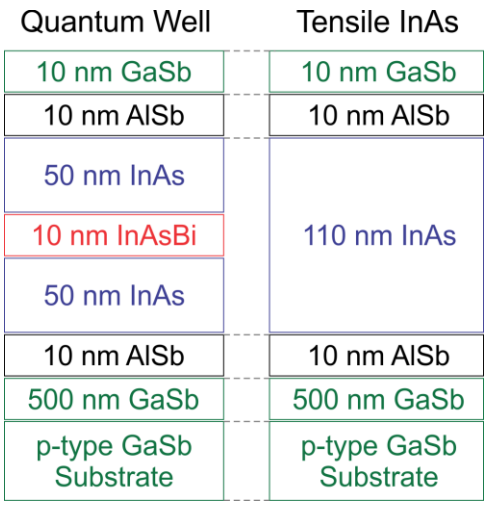


Figure 13. Cross section schematics of the InAs/InAsBi quantum well (left) and the tensile InAs reference structure (right).

During the growth of the InAs/InAsBi/InAs active region, the As/In flux ratio is 1.30 during the InAs layers, and the As/In flux ratio is reduced to near stoichiometry during the InAsBi layer to facilitate the incorporation of Bi. The two quantum wells are grown using different As-fluxes, making use of the radial non-uniformity in the As/In flux ratio so as to span a continuous set of flux conditions at 300 °C. The As/In flux profiles used for each growth are shown in Figure 14. In the first growth (green circles), the As/In flux ratio is 0.97 at the wafer center and increases to 1.01 at the wafer edge. In the second growth (blue circles), the As/In flux ratio is 1.00 at the wafer center and increases to 1.04 at the wafer edge. For both growths, a (4×2) surface reconstruction is observed on the In-terminated growth surfaces at the wafer center. From these two growths, a total of 5 samples are produced from various points on the wafers grown under different As/In flux conditions detailed in Table 6. The sixth sample in the table is the tensile InAs reference sample, which is essentially the equivalent sample structure grown without Bi shown in Figure 13. The InAs reference sample is grown with an As/In flux ratio of 1.30 (the same as the 50 nm thick InAs layers of the quantum wells), and exhibits an As-terminated (2×4) surface reconstruction. The surface reconstructions exhibited by each growth are shown in Figure 15.

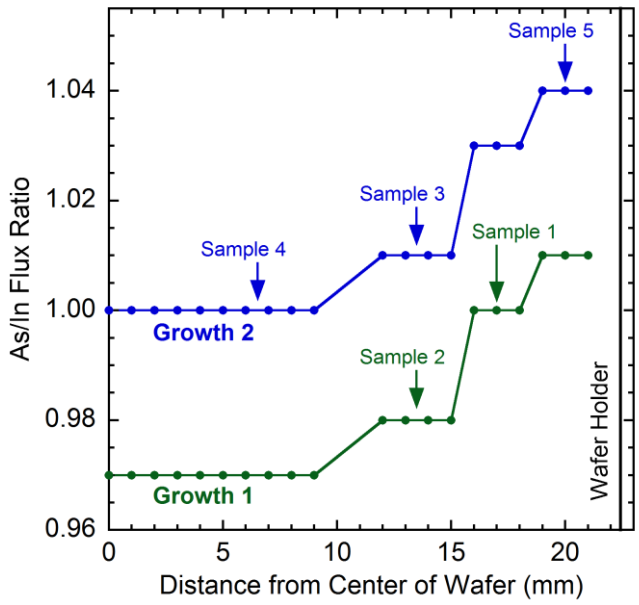


Figure 14. Radial profile of the As/In flux ratio (under rotation) for two InAs/InAsBi quantum well growths 1 and 2, from which five samples are obtained at different radial locations on the wafers.

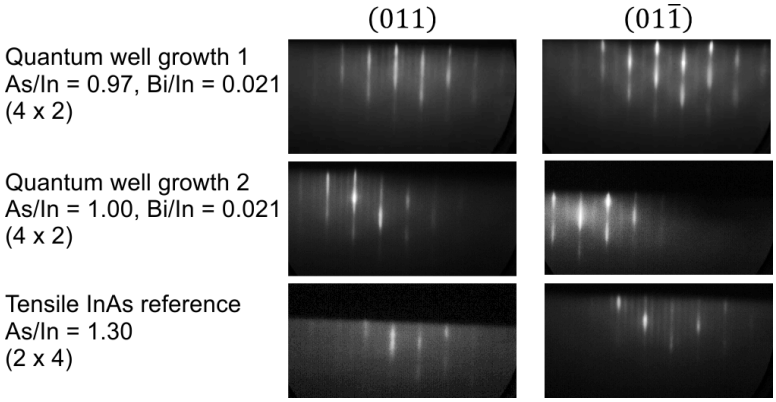


Figure 15. Reflection high-energy electron diffraction patterns observed during the growth of InAs and InAsBi under various As/In flux conditions.

Table 6. Bi mole fraction, bandgap energy, and As/In flux ratio incident during the growth of 10 nm thick InAsBi quantum wells (samples 1 – 5) and the 110 nm tensile InAs reference (sample 6). All growths are performed at 300 °C and all quantum wells are grown using a 0.021 Bi/In flux ratio.

| Sample | As/In flux ratio | Bi mole fraction (%) | Bandgap at 0 K (meV) | Bandgap at 295 K (meV) |
|---|---|---|---|---|
| 1 | 1.00 | 0.350 | 336.7 | 290.1 |
| 2 | 0.98 | 0.238 | 342.3 | 293.6 |
| 3 | 1.01 | 0.198 | 344.3 | 295.2 |
| 4 | 1.00 | 0.152 | 346.6 | 294.7 |
| 5 | 1.04 | 0.086 | 349.9 | 301.3 |
| 6 | 1.30 | 0.000 | 354.2 | 305.9 |

### 3.4 Temperature and Excitation Dependent Photoluminescence

Photoluminescence is measured as a function of temperature (12 to 295 K) and pump power (0.7 to 200 mW) using a Nicolet Instrument Corporation Magna-IR 760 Fourier transform infrared spectrometer and an 808 nm pump laser with spot diameter of 183 μm. The corresponding pump power density reaching the quantum well active region is 0.93 to 265 $W \cdot cm^{-2}$ and the corresponding carrier excitation density in the quantum well is $2 \times 10^{24}$ to $5 \times 10^{26}$ $cm^{-3} \cdot s^{-1}$. The moveable mirror in the interferometer travels slowly at 0.1582 $cm \cdot s^{-1}$, while the photoluminescence signal entering the interferometer is deliberately pulsed at a much greater rate of 50 kHz (via the pump laser) to produce an amplitude modulated time-domain interferogram on a 50 kHz carrier signal. A digital lock-in amplifier locks in on the 50 kHz interferogram to remove the ambient blackbody background and all unwanted signals that are not modulated at 50 kHz to maximize the signal to noise ratio in the photoluminescence experiments.

Characteristic low temperature photoluminescence spectra from the dilute InAsBi quantum well sample set in Table 6 are shown in Figure 16. The three subplots in the figure show the photoluminescence spectra of sample 6 with no Bi (Figure 16a), sample 5 with 0.086% Bi (Figure 16b) and sample 1 with 0.350% Bi (Figure 16c) for pump powers ranging from 0.93 to 265 $W \cdot cm^{-2}$. In the plots, each curve and excitation level indicated in blue represents an order of magnitude increase in the pump power. Increasing excitation results in a larger photoluminescence intensity, and a shift in the photoluminescence peak position to higher energies. Increasing Bi mole fraction in the quantum well produces a shift in the photoluminescence peak position and the extent of the Urbach tail to lower energies; this characteristic in the photoluminescence has also been observed in GaAsBi and is generally attributed to localized states created in the vicinity of the valence band when dilute quantities of Bi are present [48,49].

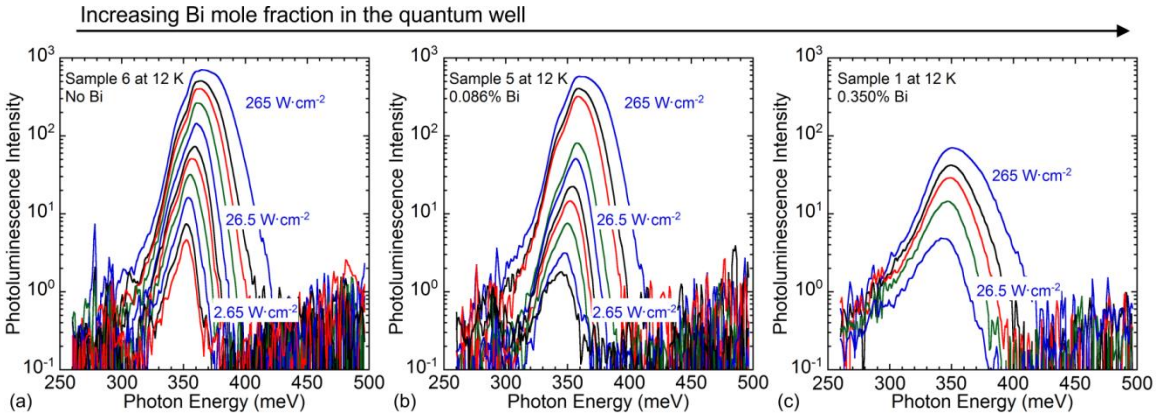


Figure 16. Photoluminescence intensity as a function of photon energy for InAs/InAsBi quantum wells with; (a) no Bi, (b) 0.086% Bi, and (c) 0.350% Bi in the quantum wells.

Figure 17 shows the photoluminescence from the highest Bi mole fraction quantum well, sample 1, as the temperature is increased from 12 to 295 K at a constant pump power density of 265 $W \cdot cm^{-2}$. The general trend of decreasing photoluminescence intensity is consistent with an increasing radiative lifetime with increasing temperature, however this is not the case at 50 K which exhibits the strongest photoluminescence intensity. The reason for this phenomenon can be understood by considering how dilute quantities of Bi introduce localized states near the valence band of the material. The deepest localized states act as the most efficient radiative recombination centers, whereas states in the continuum band are mobile enough to efficiently move to the non-radiative recombination centers that exist in the material [50]. By increasing the temperature from 12 to 50 K, sufficient thermal energy has been provided to allow localized holes to tunnel to more localized radiative centers thereby increasing the photoluminescence intensity. However as the temperature is increased further, occupation of the continuum band begins to dominate, resulting in a decrease in photoluminescence intensity as the radiative lifetime increases with temperature.

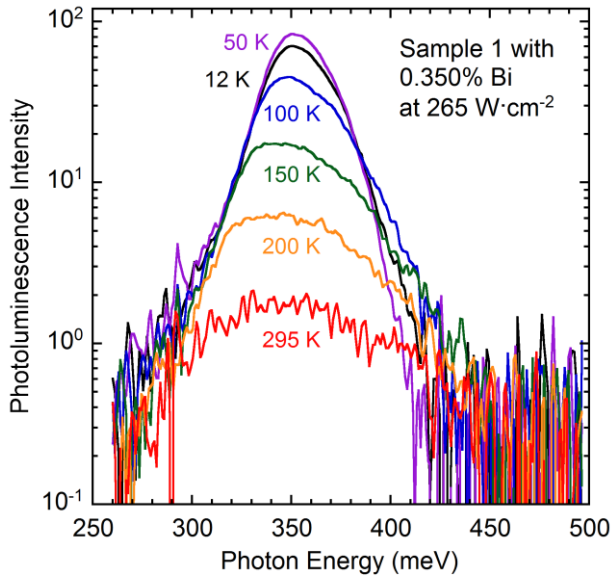


Figure 17. Photoluminescence intensity as a function of photon energy for an InAs/InAsBi quantum well with 0.350% Bi measured at temperatures ranging from 12 to 295 K.

Detailed analysis of the integrated photoluminescence intensity as a function of temperature and excitation in Figure 18 provides a measure of the overall optical quality of the InAs/InAsBi quantum wells. In the figure, the horizontal axis displays the pump power density which is proportional to the density of photogenerated electron-hole pairs ($\Delta EHP$). The vertical axis displays the integrated photoluminescence intensity ($I_{PL}$) which is proportional to the density of electron-hole pairs that recombine radiatively in the active region ($\Delta EHP_{Rad}$). The density of electron-hole pairs that recombine radiatively can be expressed as the product of the density of photogenerated electron-hole pairs ($\Delta EHP$) and the quantum efficiency ($QE$), which is itself the ratio of the radiative recombination rate ($R_{Rad}$) to the sum of the radiative and non-radiative recombination rates ($R_{Rad} + R_{Non-rad}$) given by Equation 3.

$$I_{PL} \propto \Delta EHP_{Rad} = QE \times \Delta EHP = \left[\frac{R_{Rad}}{R_{Rad} + R_{Non-rad}}\right] \times \Delta EHP \quad (3)$$

$$R_{Rad} = B_{Rad} \times \Delta EHP^2 \quad (4)$$

$$R_{Nonrad} = A_{SRH} \times \Delta EHP \quad (5)$$

$$I_{PL} \propto \left[\frac{B_{Rad} \times \Delta EHP}{B_{Rad} \times \Delta EHP + A_{SRH}}\right] \times \Delta EHP \quad (6)$$

Equation 3 can be further simplified by expressing the radiative and non-radiative recombination rates ($R_{Rad}$ and $R_{Non-rad}$) as a function of the density of photogenerated electron-hole pairs ($\Delta EHP$). The rate of the radiative recombination process is limited by the concentrations of the particles involved, namely the electron and hole concentrations, and can therefore be written as the product of the square of the photogenerated electron-hole pair density ($\Delta EHP^2$) and a rate constant ($B_{Rad}$) as shown in Equation 4. The rate constant $B_{Rad}$ is the radiative recombination coefficient which is a measure of the radiative recombination efficiency in the material, and is therefore a fundamentally thermodynamic property. On the other hand, the non-radiative recombination rate is generally a function of multiple non-radiative recombination mechanisms; however recombination through Shockley-Read-Hall recombination centers is the dominant non-radiative recombination process in this material. As a result, the non-radiative recombination rate in Equation 3 can be exchanged for the Shockley-Read-Hall recombination rate given in Equation 5. The Shockley-Read-Hall recombination centers capture minority carriers in the material which rapidly recombine with majority carriers at a rate much greater than the minority carrier capture rate. As a result, the Shockley-Read-Hall recombination rate is only limited by the density of minority carriers, and is

therefore expressed as the product of the photogenerated electron-hole pair density ($\Delta EHP$) and a rate constant ($A_{SRH}$). The rate constant $A_{SRH}$ is the Shockley-Read-Hall recombination coefficient which is a measure of the Shockley-Read-Hall recombination efficiency in the material, and is therefore primarily a function of the density of Shockley-Read-Hall recombination centers.

Substituting Equations 4 and 5 into Equation 3 and canceling the common factor of $\Delta EHP$ results in the simplified expression for the integrated photoluminescence intensity given by Equation 6. In the radiative recombination dominated limit ($B_{Rad} \times \Delta EHP \gg A_{SRH}$), the integrated photoluminescence is proportional to the density of photogenerated electron hole pairs and therefore follows a power law 1 slope when plotted as a function of pump power. On the other hand in the Shockley-Read-Hall recombination dominated limit ($B_{RAD} \times \Delta EHP \ll A_{SRH}$), the integrated photoluminescence is proportional to the square of the density of photogenerated electron hole pairs and therefore follows a power law 2 slope when plotted as a function of pump power. For each sample shown in Figure 18, the power law 1 and 2 slopes are indicated by dashed lines for comparison. It can be seen that the quantum wells operate with near unity quantum efficiency (power law 1 slope) over most temperatures and excitation levels, only exhibiting significant non-radiative recombination (slope greater than 1 but still much less than 2) at the lowest excitation levels and higher temperatures.

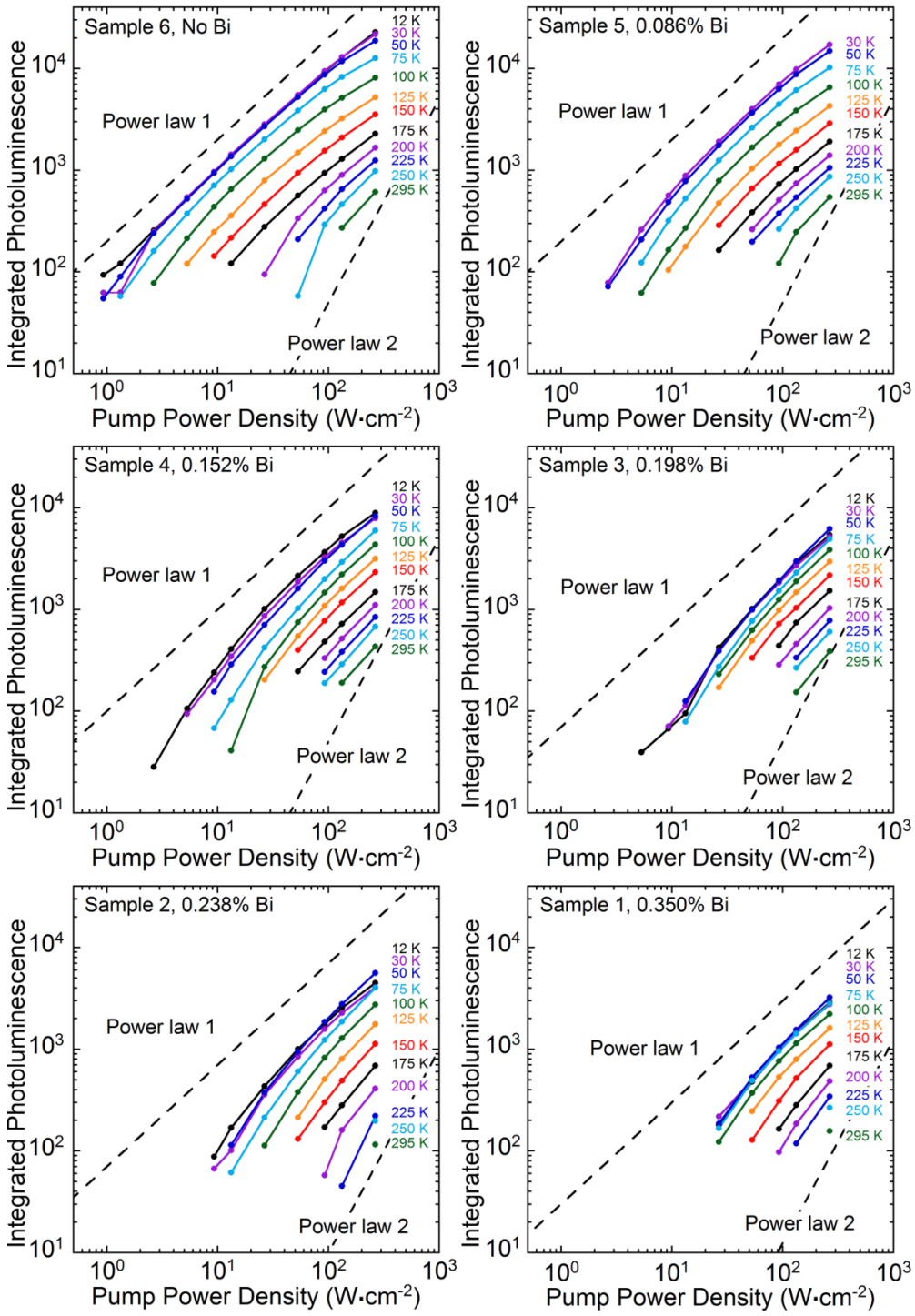


Figure 18. Integrated photoluminescence intensity plotted as a function of the pump power density used to excite InAs/InAsBi quantum wells at temperatures ranging from 12 to 295 K. Characteristic slopes for radiative (power law 1) and Shockley-Read-Hall (power law 2) limited recombination are indicated by dashed lines.

## 3.5 Temperature Dependence of the InAsBi Bandgap

To determine the temperature dependence of the InAsBi bandgap, an accurate method of identifying the bandgap from the photoluminescence is needed. As photoluminescence is the result of radiative recombination between occupied states, the photoluminescence spectrum is essentially the just the product of the optical joint density of states and the photon occupation number. Since the optical joint density of states rapidly increases at the onset of optical transitions involving the electron and hole continuum band edges at the bandgap while the occupation number decreases at a lesser rate, careful analysis of the photoluminescence first derivative as a function of photon energy can have good sensitivity to the bandgap.

Figure 19 shows the photoluminescence first derivative maximum of each InAs/InAsBi quantum well sample as a function of pump power density and temperature. For most temperatures, the photoluminescence first derivative maximum is independent of pump power density, however at the very lowest temperatures the first derivative maximum decreases with decreasing excitation and therefore warrants further investigation. The reason for this phenomenon can be understood by comparing the low temperature photoluminescence at low and high pump power densities. The green and blue curve in Figure 20 show the photoluminescence observed from sample 4 using 53 and 265 $W \cdot cm^{-2}$ of excitation. The photoluminescence first derivative maxima are indicated by green and blue arrows at 336 and 347 meV, and the blue arrow at 347 meV is extended downward to indicate its position on the green (53 $W \cdot cm^{-2}$) spectrum. Under lower excitation conditions (green curve), the bands are simply not filled up to the

bandgap at 347 meV as the photoluminescence intensity has already begun decreasing at this point; as a result, the first derivative maximum identifies the greatest rate of increase in the tail state density of states. Higher excitation conditions are needed to effectively populate the states in the continuum bands at low temperature to identify the bandgap in material with a large density of tail states as is the case in III-V-Bi materials. In chapter 4, it will be shown that the photoluminescence first derivative maximum is entirely independent of excitation in conventional materials that do not possess such a high density of tail states for temperatures as low as 15 K.

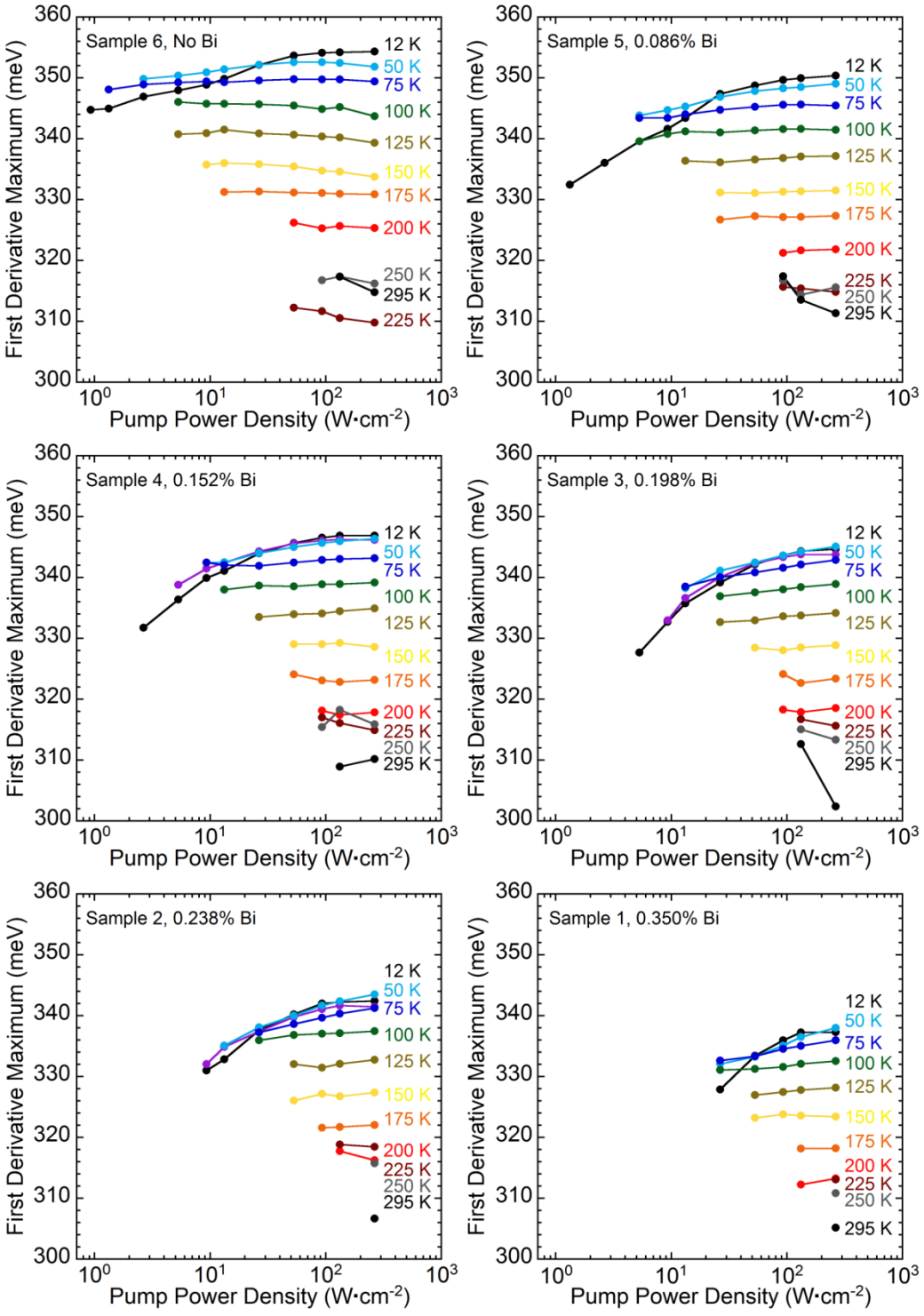


Figure 19. Photoluminescence first derivative maximum of InAs/InAsBi quantum well samples plotted as a function of the pump power density used to excite the quantum wells at temperatures ranging from 12 to 295 K.

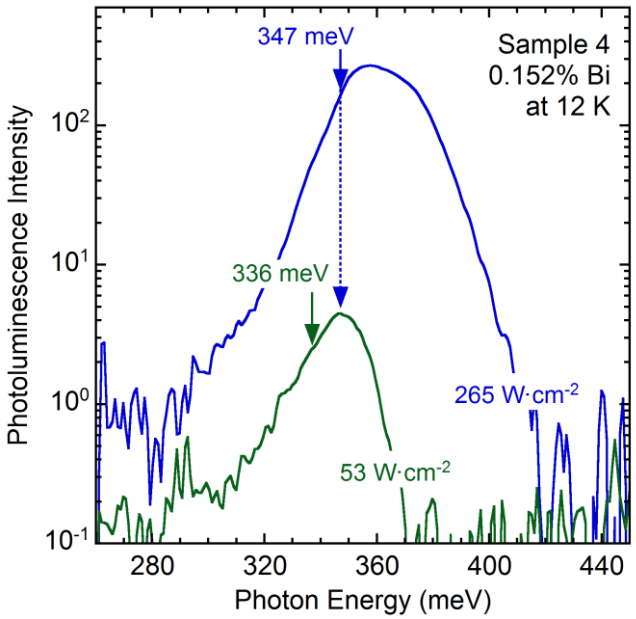


Figure 20. Low temperature photoluminescence observed from an InAs/InAsBi quantum well sample with 0.152% Bi (sample 4) under 53 and 265 $W \cdot cm^{-2}$ of excitation (green and blue curves). The photoluminescence first derivative maxima are indicated by vertical arrows.

Taking the average value of the photoluminescence first derivative maximum for pump power densities greater than 90 $W \cdot cm^{-2}$ as a measure of the bandgap energy, the bandgap of each sample (circles) is plotted as a function of temperature in Figure 21. For temperatures greater than 200 K, the photoluminescence first derivative maximum is difficult to accurately resolve because the photoluminescence signal is much broader and noisier than at lower temperatures, therefore this data represented by the open circles is not included in the analysis of the bandgap temperature dependence. Solid lines represent fits of the Einstein single oscillator model [51,52] given by Equation 7 to the temperature dependent data where $T$ is the absolute temperature, $k$ is the Boltzmann

constant (0.0862 meV/K), and the fitting parameters are $E_0$ the 0 K bandgap energy, $T_E$ the Einstein temperature, and $S_0$ the dimensionless coupling parameter where $S_0 k$ is the slope of the high temperature linear asymptote. The Einstein single oscillator model parameters for InAs/InAsBi quantum well samples 1 through 6 are detailed in Table 7.

$$E_g(T) = E_0 - \frac{S_0 k T_E}{\exp(T_E/T) - 1} \tag{7}$$

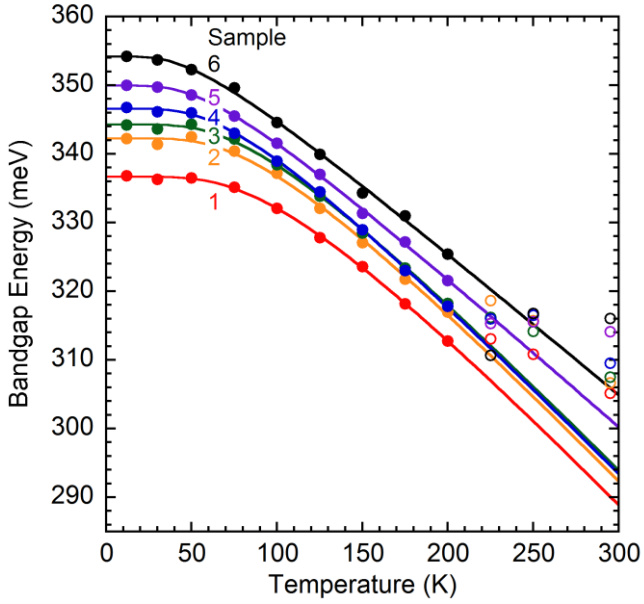


Figure 21. Bandgap energy of dilute bismide InAs/InAsBi quantum wells with Bi mole fractions ranging from 0.00 to 0.35% as a function of temperature (solid and open circles). Solid lines represent Einstein single oscillator model fits to the temperature dependent data (solid circles only).

Table 7. Einstein single oscillator model parameters ($E_0$, $S_0$, and $T_E$) and extrapolated room temperature bandgap energy $E_g$ of InAs/InAsBi quantum wells detailed in Table 6.

| Sample | Bi mole fraction (%) | $E_0$ (meV) | $S_0$ | $T_E$ (K) | $E_g$ at 295 K (meV) |
|---|---|---|---|---|---|
| 1 | 0.350 | 336.7 | 3.10 | 286.8 | 290.1 |
| 2 | 0.238 | 342.3 | 3.07 | 260.5 | 293.6 |
| 3 | 0.198 | 344.3 | 3.03 | 247.7 | 295.2 |
| 4 | 0.152 | 346.6 | 2.98 | 210.4 | 294.7 |
| 5 | 0.086 | 349.9 | 2.59 | 170.0 | 301.3 |
| 6 | 0.000 | 354.2 | 2.44 | 143.1 | 305.9 |

The Bi mole fractions listed for each quantum well in Tables 6 and 7 are determined using the band anticrossing model developed in Section 3.2. In the model, the strained bandgap reduction rate is 50.0 meV/% Bi for dilute Bi mole fractions, and the Bi mole fraction of each sample is determined by dividing the bandgap reduction relative to the reference sample with no Bi (sample 6) by this bandgap reduction rate. This is shown in Figure 22 which plots the bandgap energy of InAsBi as a function of Bi mole fraction showing each low temperature bandgap energy (blue circles) along the 50.0 meV/% Bi bandgap reduction rate (solid blue line). Also shown are the room temperature bandgap energies (red circles) inferred using the Einstein single oscillator model parameters from Figure 21 and Table 7 plotted as a function of Bi mole fraction. Fitting the slope of the extrapolated room temperature data results in nearly the same bandgap reduction rate of 50.9 meV/% Bi (solid red line).

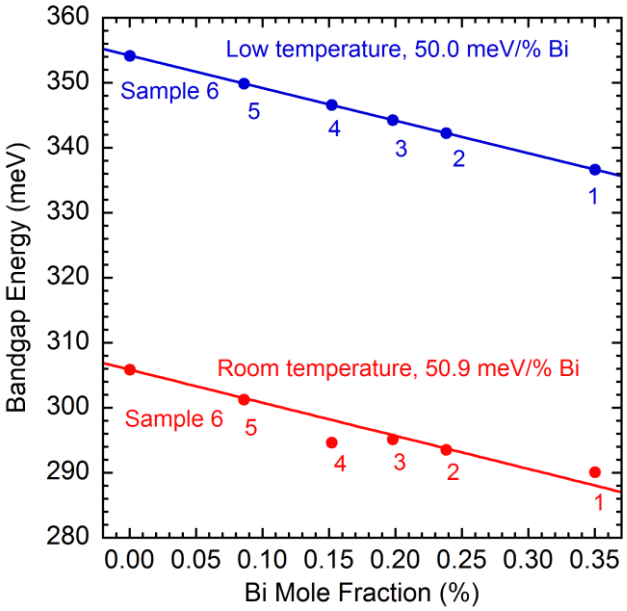


Figure 22. Bandgap energy of InAs/InAsBi quantum wells plotted as a function of Bi mole fraction. Low and room temperature bandgap data is given by blue and red circles, and the linear bandgap reduction rates are given by blue and red lines.

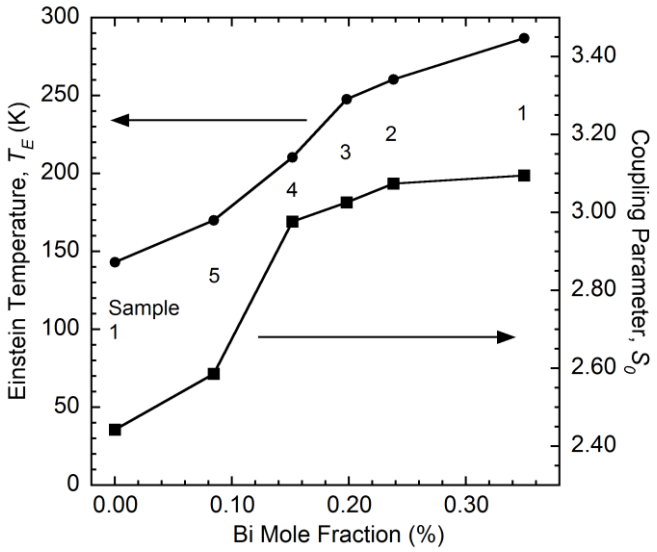


Figure 23. Temperature dependence parameters, Einstein temperature (circles, left-hand vertical axis) and coupling parameter (squares, right-hand vertical axis), of InAs/InAsBi quantum wells plotted as a function of Bi mole fraction.

Figure 23 shows the Einstein temperature (circles, left-hand vertical axis) and coupling parameter (squares, right-hand vertical axis) of the InAs/InAsBi quantum wells in Table 7 as a function of Bi mole fraction. Both the Einstein temperature and the coupling parameter increase with increasing Bi mole fraction. A larger Einstein temperature indicates that the low temperature bandgap of the material will remain temperature independent up to larger temperatures, i.e. the knee in the temperature dependent curves in Figure 21 will extend further to the right. A larger coupling parameter indicates that the bandgap will decrease at a greater rate with temperature in the high temperature linear asymptote regime.

## 3.6 Photoluminescence of Bulk InAsBi

The optical properties of bulk InAsBi are also investigated using photoluminescence spectroscopy. Whereas the InAs/InAsBi quantum wells contain carrier confinement barriers that greatly reduce the loss of photogenerated carriers outside of the active region, the bulk InAsBi structures do not contain carrier confinement layers and do not exhibit photoluminescence for the most part due to weak confinement of photogenerated carriers. Nevertheless, low temperature photoluminescence is observed from sample h with 0.33% Bi (see Table 2) excited using a pump power density of 90 $W \cdot cm^{-2}$. The photoluminescence spectra from sample h (red curve), a 300 μm thick InAs substrate (black curve), and a 500 nm thick $InAs_{0.911}Sb_{0.089}$ layer confined by 10 nm thick AlSb layers on GaSb (blue curve) are compared in Figure 24. The bandgap of the InAsBi layer is identified at the photoluminescence first derivative at 394 meV. As the

bandgap reduction rate due to Bi and due to strain [46,47] are both known, the 0.33% Bi mole fraction and 89% relaxation are determined by self-consistently using the bandgap measured using photoluminescence and dynamical simulation of the (004)-plane X-ray diffraction pattern from sample h. Comparing these results to the photoluminescence from the 500 nm thick $InAs_{0.911}Sb_{0.089}$ layer, it is found that small amount of Bi provide a large reduction in the bandgap of InAs and that rate of reduction is much greater than for Sb.

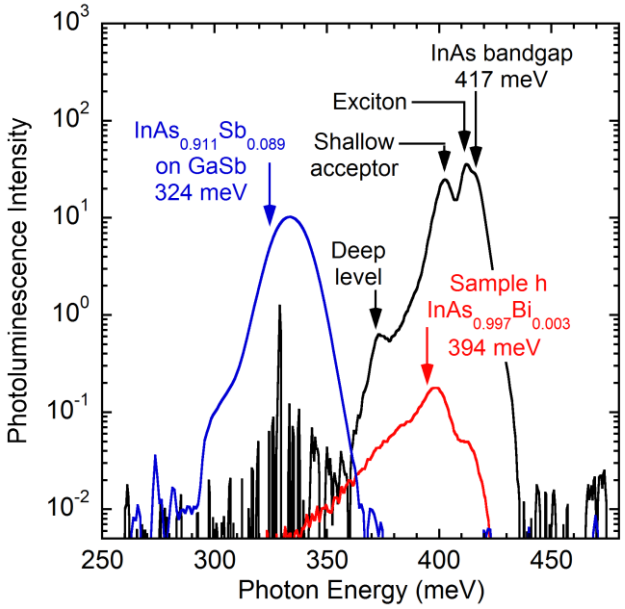


Figure 24: Low temperature (12-15 K) photoluminescence intensity as a function of photon energy for a 300 μm thick InAs substrate (black curve), an 89% relaxed 1 μm thick $InAs_{0.9967}Bi_{0.0033}$ layer on GaSb (red curve, sample h), and a 500 nm thick lattice-matched $InAs_{0.911}Sb_{0.089}$ layer on GaSb (blue curve). Low Bi incorporation in the InAsBi layer resulted in its relaxation and the formation of Bi surface droplets, both of which act to reduce the photoluminescence intensity.

## 3.7 Chapter 3 Summary

The optical constants and absorption coefficient of bulk $InAs_{0.936}Bi_{0.064}$ are measured using spectroscopic ellipsometry, and the bandgap energy of InAsBi is characterized as a function of mole fraction using the band anticrossing model and a Bi coupling parameter of 1.529 eV. Careful analysis of photoluminescence from InAs/InAsBi quantum wells indicates that the quantum well active regions operate with high internal quantum efficiency over most temperatures and excitation levels, in addition to providing a measurement of the Einstein single oscillator model temperature dependence parameters as a function of Bi mole fraction.

# 4. OPTICAL PROPERTIES OF *$InAs_{0.911}Sb_{0.089}$* AND *InAs/InAsSb*

The structural and optical properties of lattice-matched bulk $InAs_{0.911}Sb_{0.089}$ and strain-balanced InAs/InAsSb superlattices grown on (100)-oriented GaSb substrates by molecular beam epitaxy are examined using X-ray diffraction, spectroscopic ellipsometry and photoluminescence spectroscopy. The photoluminescence and ellipsometry measurements determine the ground state transition energy or bandgap energy and the X-ray diffraction measurements determine the layer thicknesses and mole fractions of the structures studied. Detailed modeling of the X-ray diffraction data is utilized to quantify the unintentional incorporation of approximately 1% Sb into the InAs layers of the superlattices. A Kronig-Penney model of the superlattice miniband structure is used to analyze the valence band offset between InAs and InAsSb, and hence the InAsSb band edge positions as a function of temperature and mole fraction. With the band alignment accurately established, the absorption coefficient of the superlattice is found to be directly proportional to the square of the electron-hole wavefunction overlap.

## 4.1 Growth and Characterization of $InAs_{0.911}Sb_{0.089}$

A single bulk $InAs_{0.911}Sb_{0.089}$ sample as well as two calibration samples are grown by molecular beam epitaxy at 430 °C on (100)-oriented, ¼ 50 mm GaSb substrates. The sample cross section is shown in Figure 25, and consists of a 500 nm thick InAsSb layer sandwiched between two 10 nm thick AlSb layers that provide carrier confinement for photoluminescence experiments, with a 10 nm thick GaSb cap to prevent oxidation of the upper AlSb layer. The precise composition of the InAsSb layer of each sample is

determined using a PANalytical X'Pert PRO Materials Research Diffractometer and the dynamical X-ray diffraction software X'pert Epitaxy [34]. The incident beam optics on the diffractometer consist of an X-ray mirror and a 2-crystal Ge (220) 4-bounce monochromator with a 0.25 degree divergence slit, and a 0.25 inch width mask is used to probe a large area of the sample. The diffracted beam optics utilize a triple axis monochromator and a 0.50 degree slit placed before the detector.

Coupled ω-2θ X-ray diffraction scans from the (004)-planes of the two calibration samples (dotted and dot-dashed black curves) and the lattice-matched sample (solid black curve) are shown in Figure 26. Sb mole fractions of 0.093 and 0.087 are determined from the diffraction patterns of two calibration samples, and the lattice-matched mole fraction of 0.089 is inferred from the diffraction pattern of the lattice-matched sample (solid black curve) as the coincident substrate and layer diffraction peaks are no broader than the diffraction peak from a bare GaSb wafer (solid grey curve). Pendellösung fringes which arise as a result of the 10 nm thick AlSb layers that sandwich the lattice-matched InAsSb attest that the layer thickness is 500 ± 20 nm. The same piece of the $InAs_{0.911}Sb_{0.089}$ sample on which X-ray diffraction is performed is then cleaved into photoluminescence and ellipsometry samples, and the ellipsometry sample is backside roughened with 400 grit sandpaper to diffusely scatter any light that may reach the backside of the semitransparent GaSb wafer during the ellipsometry measurement. The backside roughing procedure is detailed in Appendix A.

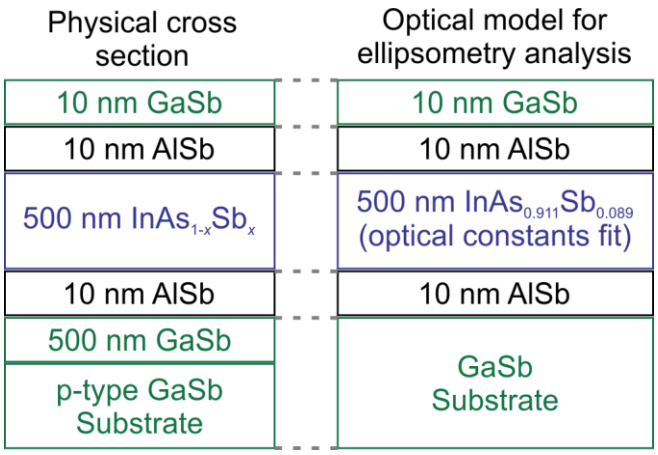


Figure 25. Left side shows the cross section schematic of the lattice-matched bulk InAsSb sample ($x = 0.089$) and the nearly lattice-matched calibration samples ($x \neq 0.089$). Right side shows optical model of the lattice-matched InAsSb sample used for ellipsometry analysis.

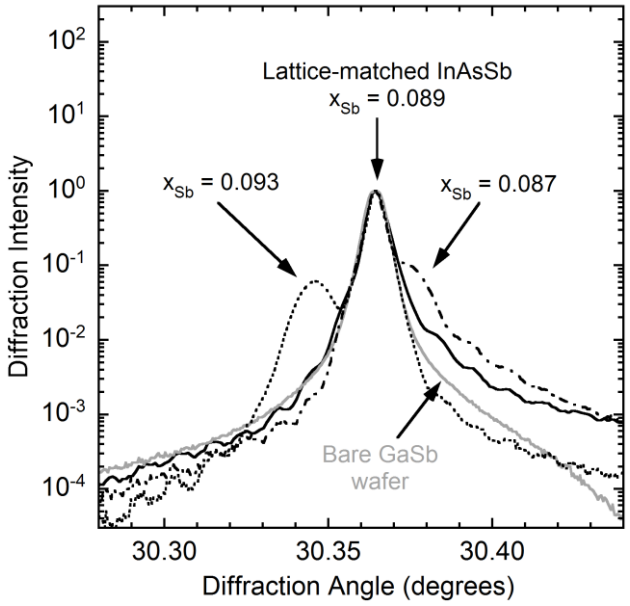


Figure 26. Coupled ω-2θ X-ray diffraction patterns from the (004)-planes of a series of calibration growths (dotted and dot-dashed black curves) used to precisely target the lattice-matched mole fraction for $InAs_{0.911}Sb_{0.089}$ on GaSb (solid black curve). X-ray diffraction from a bare GaSb wafer is shown for comparison (solid grey curve).

The optical constants of the lattice-matched bulk $InAs_{0.911}Sb_{0.089}$ layer are measured at room temperature using an infrared variable angle spectroscopic ellipsometer [38]. The optical constants are obtained from the measured ellipsometric parameters Ψ and Δ, using the basic point-by-point (wavelength-by-wavelength) analysis method [40] and the optical model for the layer structure shown in Figure 25. The WVASE software library provides optical constants of the surrounding AlSb and GaSb layers [39], and the model assumes that there are no reflections from the backside of the substrate. The point-by-point analysis provides the optical constants, $n$ and $k$, and the absorption coefficient ($\alpha = 4\pi k/\lambda$ for extinction coefficient $k$ and photon wavelength $\lambda$) of the bulk $InAs_{0.911}Sb_{0.089}$ layer. This results in the actual measured absorption coefficient unmodified by any particular fitting or smoothing model such as the general oscillator model and its various functional forms.

As the absorption coefficient is proportional to the optical joint density of states, its first derivative as function of photon energy is used to identify the maximum rate of change in the optical joint density of states and hence the energy at which the onset of optical transitions involving the continuum band edges occurs. The absorption coefficient of $InAs_{0.911}Sb_{0.089}$ is shown in Figure 27 (black curve) alongside its first derivative (grey curve) that shows two distinct absorption features occurring at 225 and 277 meV. The 225 meV feature is the cutoff in the below bandgap absorption, which is the point at which absorption in the 500 nm thick layer is no longer observable. The 277 meV feature is onset of optical transitions involving the continuum band edges of the fundamental bandgap.

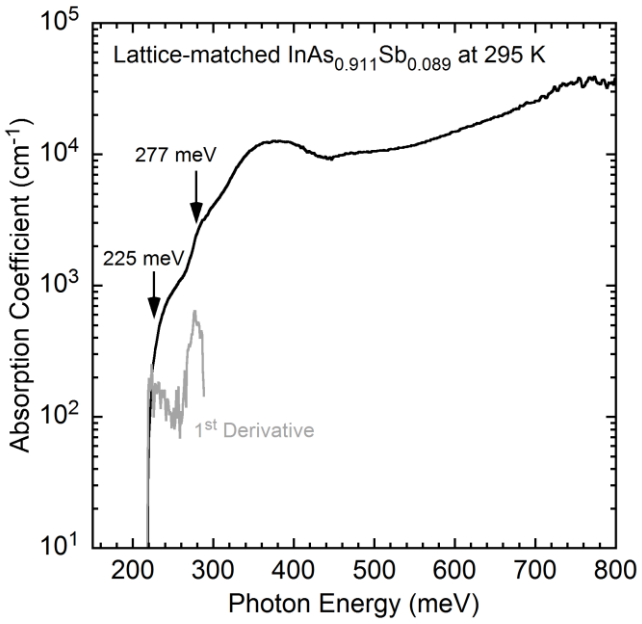


Figure 27. Absorption coefficient of bulk $InAs_{0.911}Sb_{0.089}$ (black curve) and its first derivative as a function of photon energy (grey curve). Two absorption onsets are identified at peaks in the first derivative, one at the onset of sample absorption (225 meV) and another at the bandgap energy (277 meV).

Photoluminescence is measured as a function of temperature (15 to 295 K) and pump power (0.1 to 200 mW) using a Nicolet Instrument Corporation Magna-IR 760 Fourier transform infrared spectrometer and an 808 nm pump laser with spot diameter of 183 μm. The corresponding pump power density at the upper InAsSb layer interface is 0.133 to 265 $W \cdot cm^{-2}$ and the corresponding carrier excitation density in the InAsSb layer is $1 \times 10^{22}$ to $2 \times 10^{25}$ $cm^{-3} \cdot s^{-1}$. The bandgap energy is determined at each temperature using two methods, both of which are demonstrated using the 30 K photoluminescence spectra plotted in Figure 28. In the peak method, the bandgap energy ($E_p$) is identified as the photoluminescence peak energy minus $kT/2$ [53]. This method assumes an idealized

parabolic band cutoff in the density of states of bulk material, ignoring the impact of localized states found near the continuum band edges in real material [52,54]. In the photoluminescence first derivative method, the bandgap energy ($E_g$) is identified as the maximum of the first derivative of the photoluminescence spectra (shown in the inset of Figure 28), which identifies the maximum change in the optical joint density of states at the bandgap energy. Note that both methods correctly identify the bandgap energy in the idealized case of a perfectly sharp band edge cutoff specified by the parabolic band model.

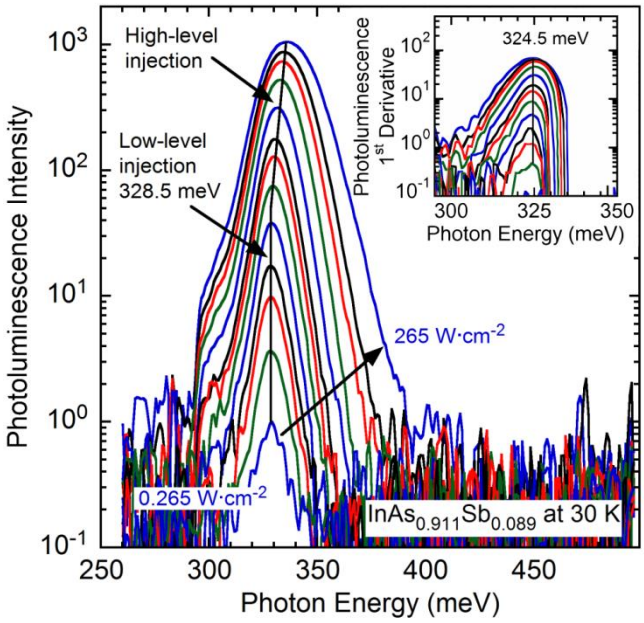


Figure 28. Photoluminescence spectra from lattice-matched $InAs_{0.911}Sb_{0.089}$ on GaSb at 30 K, excited using pump power densities ranging from 0.265 to 265 $W \cdot cm^{-2}$. The photoluminescence peak position is independent of pump power under low injection (0.265 to 2.65 $W \cdot cm^{-2}$) and blue shifts under high injection (2.65 to 265 $W \cdot cm^{-2}$). The inset shows the first derivative of the spectra and the position of their maxima (vertical black line).

Two injection level regimes are indicated in Figure 28; at high injection the photoluminescence peak blue shifts with increasing excitation density, while at low injection the photoluminescence peak energy is independent of excitation density. When identifying the bandgap energy using the peak minus $kT/2$ method, the low injection photoluminescence peak position is used and results in a 30 K bandgap energy ($E_p$ = 327.2 meV) specified by the peak position (328.5 meV) less $kT/2$ (1.3 meV). On the other hand, using the first derivative maximum, a 30 K bandgap energy ($E_g$ = 324.5 meV) is identified that is 2.7 meV smaller. The significance of the first derivative maximum method is that it indicates the energy at which the product of the optical joint density of states and photon occupation number increases at the greatest rate. Since the optical joint density of states rapidly increases at the onset of optical transitions involving the electron and hole continuum band edges (i.e. at the bandgap) and the occupation number decreases at a slower rate, the analysis has good sensitivity to the bandgap energy and is less sensitive to injection level. Whereas the InAs/InAsBi quantum wells possessed a significant density of below-bandgap states that had to be considered in the first derivative analysis, the tail state density in InAsSb is significantly lower as evidenced by the coincident first derivative peak positions in the inset of Figure 28 which are insensitive to the excitation rate.

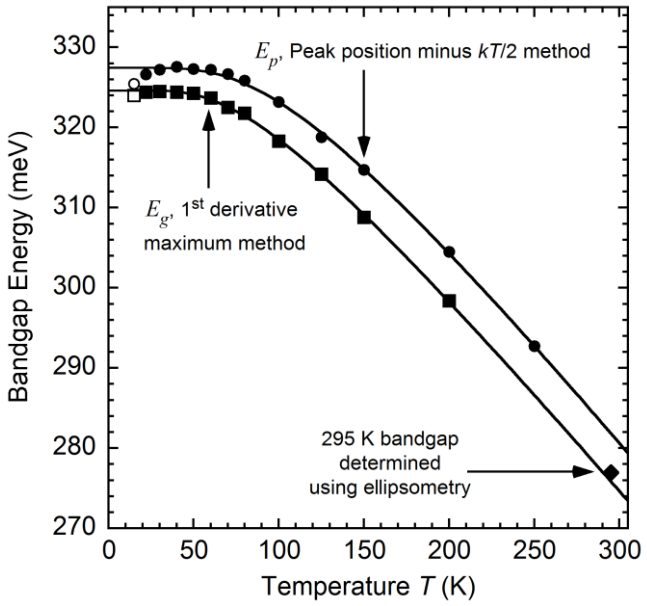


Figure 29. Bandgap energy as a function of temperature for lattice-matched $InAs_{0.911}Sb_{0.089}$ on GaSb determined from the photoluminescence peak energy minus $kT/2$ ($E_p$, circles) and the first derivative maximum of the photoluminescence spectra ($E_g$, squares). The Einstein single oscillator model (solid curves) is fit to the bandgap data. The room temperature bandgap energy (diamond) measured by spectroscopic ellipsometry is shown for comparison.

The $InAs_{0.911}Sb_{0.089}$ bandgap energies are plotted as a function of temperature in Figure 29 where the values given by the photoluminescence peak position minus $kT/2$ ($E_p$) are specified by the solid and open circles and those given by the first derivative maximum ($E_g$) are specified by the solid and open squares. Room temperature photoluminescence is observed, however the photoluminescence first derivative maximum cannot be accurately identified due to strong $CO_2$ absorption near 290 meV.[1]

[1] The room temperature bandgap of this sample is determined using the photoluminescence first derivative maximum by correcting the photoluminescence spectra for the optical throughput of the system in later work discussed in Chapter 5.

In its place, the room temperature bandgap energy determined by spectroscopic ellipsometry is shown with a solid diamond at 295 K. The solid curves in Figure 29 are fits of the Einstein single oscillator model [51,52] (Equation 7) to the temperature dependent data: $T$ is the absolute temperature, $k$ is the Boltzmann constant (0.0862 meV/K), and the fitting parameters are $E_0$ the 0 K bandgap energy, $T_E$ the Einstein temperature, and $S_0$ the dimensionless coupling parameter where $S_0 k$ is the slope of the high temperature linear asymptote.

$$E_g(T) = E_0 - \frac{S_0 k T_E}{\exp(T_E/T) - 1} \tag{7}$$

The best fit parameters for the bandgaps specified by each method ($E_p$ and $E_g$) are respectively 327.4 and 324.6 meV for $E_0$, 298.5 and 240.3 K for $T_E$, and 3.10 and 2.96 for $S_0$. For both methods, the open circle and square at 15 K are omitted from the fit as the decrease in bandgap energy with decreasing temperature is likely a result of a small degree of compositional inhomogeneity in the alloy. The Einstein single oscillator best fit parameters are summarized in Table 8; in addition to those mentioned above, the parameters with the room temperature bandgap value included are shown in the last row of the table. It is worth noting that the 327.4 meV value for $E_0$ determined using the photoluminescence peak position minus $kT/2$ is consistent with the bandgap value of 327 meV for $InAs_{0.9}Sb_{0.1}$ determined using the same method in [55]. The advantage of the first derivative method is that it systematically identifies the bandgap energy for both emission and absorption measurements as it is sensitive to the underlying material band structure; note the agreement of photoluminescence and ellipsometry experiments shown in Figure 29.

Table 8. Bandgap temperature dependence parameters ($E_0$, $S_0$, and $T_E$) for $InAs_{0.911}Sb_{0.089}$ as determined from the peak position minus $kT/2$ method ($E_p$) and the first derivative maximum method ($E_g$). For the first derivative maximum method, the fit is performed with and without the room temperature bandgap determined from spectroscopic ellipsometry.

| Method | $E_0$ (meV) | $S_0$ | $T_E$ (K) |
|---|---|---|---|
| Peak minus $kT/2$, $E_p$ | 327.4 | 3.10 | 298.5 |
| First derivative maximum, $E_g$ (without room temperature data) | 324.6 | 2.96 | 240.3 |
| First derivative maximum, $E_g$ (with room temperature data) | 324.7 | 2.85 | 230.7 |

Table 9. Comparison of the Einstein single oscillator model and Varshni equation fits to the temperature dependence of the $InAs_{0.911}Sb_{0.089}$ bandgap energy. The low temperature bandgap energy is $E_0$ for both models, the linear bandgap reduction rate in the high temperature region is $\alpha$ for the Varshni equation and $S_0 k$ for the single oscillator model, the intersection of the zero temperature bandgap energy and high temperature asymptote is $\beta$ for the Varshni equation and $\frac{1}{2}T_E$ for the single oscillator model, and the bandgap reduction due to the zero-point motion of the lattice is $\alpha\beta$ for the Varshni equation and $\frac{1}{2}S_0 k T_E$ for the single oscillator model.

| Model | $E_0$ (meV) | $S_0 k$; $\alpha$ (meV/K) | $\frac{1}{2}T_E$; $\beta$ (K) | $\frac{1}{2}S_0 k T_E$; $\alpha\beta$ (meV) |
|---|---|---|---|---|
| Einstein single oscillator | 324.7 | 0.246 | 115.4 | 28.3 |
| Varshni equation (All T) | 326.2 | 0.359 | 335.0 | 120.3 |
| Varshni equation (T > 80 K) | 329.7 | 0.256 | 128.1 | 32.8 |

Since the Varshni equation [56] (Equation 8) is commonly used to describe the temperature dependence of the bandgap energy in these materials [3], the Einstein single oscillator model (solid curve) and the Varshni equation (dotted and dashed curves) are compared in Figure 30 by way of best fits to the bandgap measurements, $E_g$, determined using the first derivative method (solid squares). This is same data shown in Figure 29 with the inclusion of the room temperature bandgap value determined using spectroscopic ellipsometry. The fit parameters are compared in Table 9, where the zero temperature bandgap is $E_0$ for both models, the high temperature linear slope is $\alpha$ for the Varshni equation and $S_0 k$ for the single oscillator model, the position of the knee (intersection of the zero temperature bandgap energy and the high temperature linear asymptote) is $\beta$ for the Varshni equation and $\frac{1}{2}T_E$ for the single oscillator model, and the bandgap reduction due to the zero-point motion of the lattice is $\alpha\beta$ for the Varshni equation and $\frac{1}{2}S_0 k T_E$ for the single oscillator model.

$$E_g(T) = E_0 - \frac{\alpha T^2}{T + \beta} \tag{8}$$

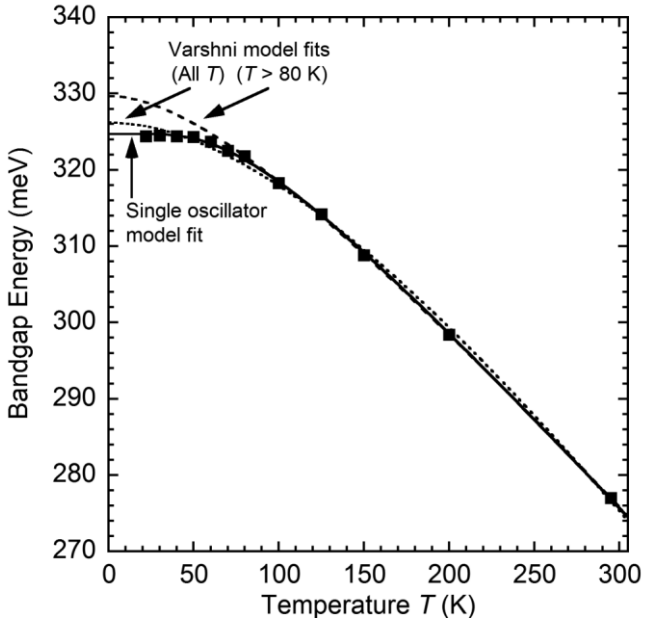


Figure 30. Bandgap energy as a function of temperature for lattice-matched bulk $InAs_{0.911}Sb_{0.089}$ on GaSb determined using the first derivative maximum method. The Einstein single oscillator model is shown as the solid curve and the Varshni equation as the dotted curve (all temperatures) and dashed curve (temperatures greater than 80 K).

The functional form of the empirical Varshni equation (dotted curve) does not describe the bandgap data in Figure 30 nearly as well as the physical Einstein single oscillator model (solid curve), particularly for the low temperature data where the Varshni equation is quadratic. This quadratic behavior overestimates the value of the low temperature bandgap and underestimates the curvature of the knee region where the thermal phonon occupation first starts to significantly shift the bandgap with temperature. Furthermore, the Varshni equation does not capture the linear dependence of bandgap at room temperature and beyond. When the low temperature data is excluded, the Varshni equation more accurately identifies the linear dependence of bandgap at room

temperature as illustrated by the dashed curve in Figure 30 fit to the data for temperatures greater than 80 K. The limitations of the Varshni equation have been previously noted by several authors [57-59]. The issue confronting empirical models is that they essentially require four parameters to describe the temperature dependence of the bandgap energy; (1) the low temperature bandgap, (2) the position of knee, (3) the curvature of the knee, and (4) the high temperature slope. A 4-parameter empirical model is shown to work well for many III-V materials [57]. However, since the Einstein single oscillator is a physical model, it precisely describes the temperature dependence of the bandgap using three fitting parameters, as the shape of the knee is effectively described by the functional form of the physical model.

In order to determine the bandgap of $InAs_{1-x}Sb_x$ as a function of temperature and Sb mole fraction $x$, the bandgap bowing parameter $b_g(T)$ in Equation 9 is fit as a function of temperature to the bandgaps of $InAs_{0.911}Sb_{0.089}$, InAs, and InSb. The resulting low and room temperature bandgap bowing parameters of 938 meV at 0 K and 750 meV at 295 K are obtained using the low and room temperature bandgaps of $InAs_{0.911}Sb_{0.089}$, InAs, and InSb; $E_{g\,InAsSb}(0.089,T)$ is 324.7 meV at 0 K and 277.0 meV at 295 K (this work), $E_{g\,InAs}(T)$ is 417.0 meV at 0 K [3] and 354.0 meV at 295 K (this work), and $E_{g\,InSb}(T)$ is 235.0 meV at 0 K [3] and 172.0 meV at 295 K (this work). The room temperature bandgap energies of InAs and InSb are determined from spectroscopic ellipsometry measurements of InAs and InSb substrates analyzed in a similar manner as the bulk $InAs_{0.911}Sb_{0.089}$ layer shown in Figure 27, and are consistent with those values reported in [3] and [60] of 355 and 352 meV for InAs and 175 and 176 meV for InSb.

The temperature dependence of the bandgaps $E_{g\,InSb}(T)$ and $E_{g\,InAs}(T)$ in Equation 9 are described by the single oscillator model given in Equation 7 and plotted in Figure 31 alongside the absorption coefficients of InAs and InSb from which the room temperature bandgap energies are derived. The resulting oscillator model parameters are listed in Table 10 where $E_0$ is the low temperature bandgap most commonly reported in [3], $S_0$ is the coupling parameter obtained from the high temperature linear asymptotes in [60], and $T_E$ is fit to obtain the bandgap energies measured by spectroscopic ellipsometry at room temperature. The temperature dependence of the bowing parameter $b_g(T)$ is accurately described using the double oscillator model in Equation 10, with the resulting parameters provided in Table 11.

$$E_{g\,InAsSb}(x,T) = x \cdot E_{g\,InSb}(T) + (1-x) \cdot E_{g\,InAs}(T) - x(1-x)b_g(T) \tag{9}$$

$$b_g(T) = b_0 - \frac{S_1 k T_1}{\exp(T_1/T) - 1} + \frac{S_2 k T_2}{\exp(T_2/T) - 1} \tag{10}$$

Table 10. Bandgap temperature dependent parameters ($E_0$, $S_0$, and $T_E$) for bulk InAs and InSb.

| Material | $E_0$ (meV) | $S_0$ | $T_E$ (K) |
|---|---|---|---|
| InAs | 417 | 3.20 | 145.0 |
| InSb | 235 | 3.13 | 133.0 |

Table 11. Bandgap bowing parameter temperature dependent parameters ($b_0$, $S_1$, $T_1$, $S_2$, and $T_2$) for bulk $InAs_{1-x}Sb_x$.

| Material | $b_0$ (meV) | $S_1$ | $T_1$ (K) | $S_2$ | $T_2$ (K) |
|---|---|---|---|---|---|
| InAsSb | 938 | 22.98 | 115.8 | 18.80 | 275.6 |

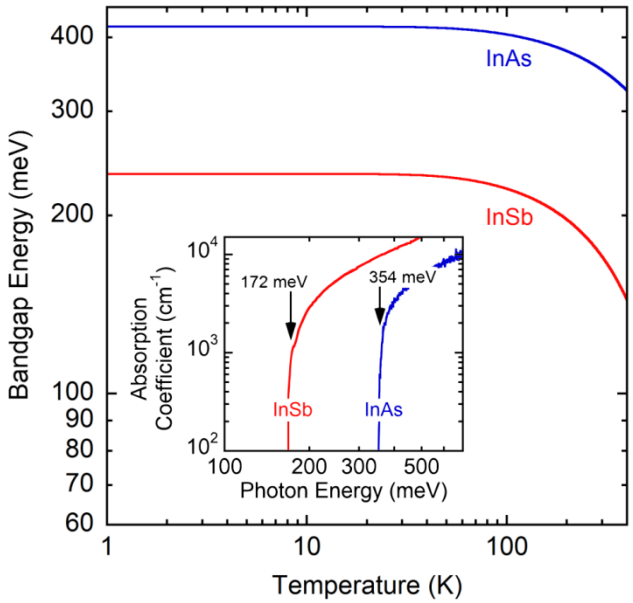


Figure 31. Bandgap temperature dependence of InAs (blue curve) and InSb (red curve) calculated using the Einstein single oscillator model and the model parameters detailed in Table 10. Inset shows the room temperature absorption coefficients used to determine the room temperature bandgaps of InAs and InSb.

## 4.2 Growth and Characterization of InAs/InAsSb Superlattices

The strain-balanced InAs/InAsSb superlattice samples studied are grown by molecular beam epitaxy on (100)-oriented ¼ and full 50 mm GaSb substrates at temperatures ranging from 400 to 450°C. The superlattice structures are composed of alternating thin layers of InAs and InAsSb with a total thickness of 0.5 to 11 μm sandwiched between 10 nm thick AlSb confinement layers with a 10 nm thick GaSb or InAs cap; the physical cross section of one 0.5 μm thick InAs/InAsSb superlattice (sample B) is shown schematically in Figure 32. The growth is performed using constant In- and As-fluxes with the superlattice defined by modulating the Sb-flux with the Sb shutter that is closed during the InAs layer and open during the InAsSb layer. For all samples, the In-flux is held constant throughout the structure at around 0.5 monolayers per second with a constant As/In flux ratio of 1.20, whereas the Sb/In flux ratio ranges from 0.25 to 2.00 for the various samples and is the determining factor for the Sb mole fraction for a given growth temperature. For an As/In flux ratio of 1.20, the sticking coefficient of Sb is about 40% for a growth temperature of 430 °C [11]; the sticking coefficient is temperature and As/In dependent and in particular decreases for higher temperature growths.

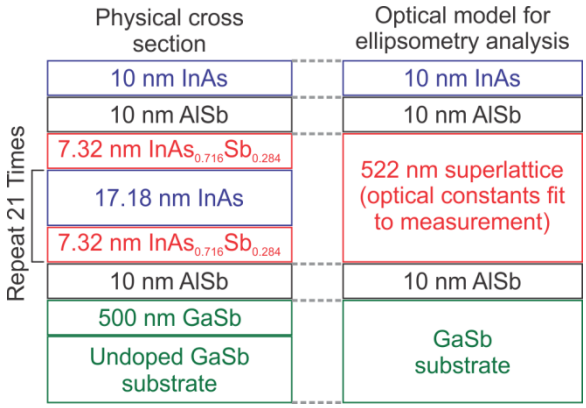


Figure 32. InAs/InAsSb superlattice sample cross section (sample B, left), alongside the optical model used for ellipsometry analysis (right), which combines the entire superlattice region into a single layer with a unique set of optical constants.

In total, ten InAs/InAsSb superlattices are studied and summarized in Table 12. Reciprocal space mapping in the vicinity of the (115)-reflection of the GaSb substrate is used to verify that the substrate and superlattice satellite diffraction peaks occur at the same in-plane reciprocal lattice vector, which indicates that the InAs and InAsSb layers of the superlattice all possess the same in-plane lattice constant and are therefore coherently strained. The only sample to show any degree of relaxation is sample A shown in Figure 33, which exhibits a substrate diffraction peak at 2.320 $nm^{-1}$ ($a_{GaSb}$= 0.60957 nm) and superlattice satellite peaks at 2.321 $nm^{-1}$ ($a_{SL}$= 0.60933 nm). As the expected reciprocal lattice vector for unstrained InAs is 2.334 $nm^{-1}$ ($a_{InAs}$= 0.60583 nm), these results suggest that the effective lattice constant of the superlattice has relaxed 6.4% towards the lattice constant of InAs due to the net tensile strain of 0.19% in this structure. This small degree of lattice relaxation is taken into account for the determination of the physical and electronic properties of this sample.

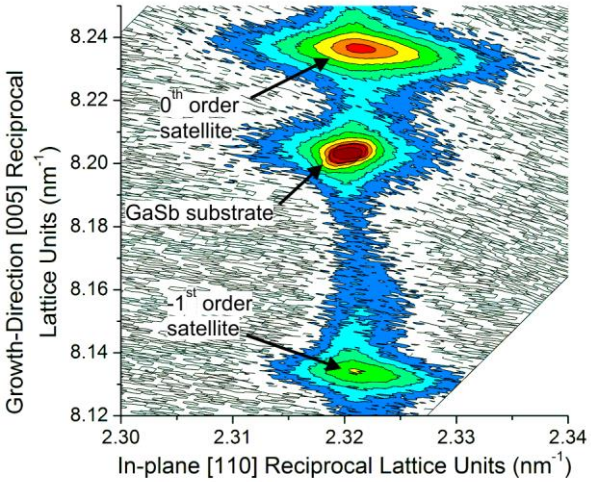


Figure 33. Reciprocal space map of an InAs/InAsSb superlattice (sample A) which exhibits approximately 6.4% relaxation towards the lattice constant of InAs.

Table 12. Growth temperature (1), effective bandgaps (2), structural properties (3) and (4), and optical properties (5) of strain-balanced InAs/InAsSb superlattices. The bandgap energies are measured by spectroscopic ellipsometry at room temperature and photoluminescence spectroscopy at low temperature. The structural parameters are determined by room temperature X-ray diffraction measurements, where the analysis utilizes a model without (3) and with (4) the incorporation of unintentional Sb in the InAs layer. The absorption coefficient is measured using spectroscopic ellipsometry and the wavefunction overlap and optical joint density of states are calculated using a Kronig-Penney model of the superlattice miniband structure.

| | (1) | (2) First derivative maximum method | | (3) Structural parameters: Assuming no unintentional Sb in InAs | | | (4) Structural parameters: Including unintentional Sb in InAs | | | | (5) Optical properties | | |
|---|---|---|---|---|---|---|---|---|---|---|---|---|---|
| Sample | Growth temp. (°C) | 295 K transition energy (meV) | 12 K transition energy (meV) | Sb mole fraction $x$ | InAs layer thickness (nm) | $InAs_{1-x}Sb_x$ layer thickness (nm) | Average unintentional Sb mole fraction in InAs | Sb mole fraction $x$ | InAs layer thickness (nm) | $InAs_{1-x}Sb_x$ layer thickness (nm) | Wavefunction overlap squared (%) | Ground state absorption coefficient ($cm^{-1}$) | Ground state optical joint density of states $\rho_0$ ($cm^{-3}\cdot eV^{-1}$) |
| A | 400 | 260 | 311 | 0.130 | 5.13 | 4.61 | 0.012 | 0.117 | 5.14 | 4.60 | 65.31 | 3571 | $4.14\times10^{18}$ |
| B | 405 | 103 | 156 | 0.284 | 17.18 | 7.32 | 0.008 | 0.263 | 17.16 | 7.34 | 10.25 | 456 | $3.72\times10^{18}$ |
| C | 410 | 76 | 128 | 0.312 | 18.64 | 5.70 | 0.006 | 0.291 | 18.66 | 5.68 | 8.05 | 455 | $3.71\times10^{18}$ |
| D | 450 | 136 | ... | 0.328 | 8.19 | 2.52 | 0.014 | 0.279 | 8.21 | 2.50 | 30.51 | 1400 | $4.14\times10^{18}$ |
| E | 410 | 74 | 122 | 0.343 | 15.21 | 4.67 | 0.006 | 0.322 | 15.23 | 4.65 | 12.12 | 517 | $3.43\times10^{18}$ |
| F | 410 | 56 | 98 | 0.360 | 18.59 | 5.72 | 0.006 | 0.338 | 18.60 | 5.70 | 7.74 | 422 | $3.68\times10^{18}$ |
| G | 410 | 51 | 102 | 0.367 | 15.29 | 4.71 | 0.006 | 0.345 | 15.31 | 4.69 | 10.77 | 572 | $3.64\times10^{18}$ |
| H | 410 | 64 | 106 | 0.370 | 14.83 | 4.56 | 0.006 | 0.348 | 14.84 | 4.56 | 12.36 | 577 | $3.43\times10^{18}$ |
| I | 410 | 107 | 162 | 0.392 | 7.93 | 2.46 | 0.012 | 0.351 | 7.94 | 2.45 | 29.73 | 1645 | $4.12\times10^{18}$ |
| J | 400 | 68 | 134 | 0.400 | 8.31 | 2.58 | 0.010 | 0.367 | 8.31 | 2.57 | 25.36 | 1395 | $4.22\times10^{18}$ |

The structural properties of the superlattices are determined using commercial dynamical X-ray diffraction software [34] and a self-consistent analysis of coupled ω-2θ X-ray diffraction scans from the (004)-planes of each sample. In this analysis, the satellite peak spacing determines the superlattice period thickness. The $0^{th}$ order satellite peak position is a function of the Sb mole fraction and the InAs/InAsSb thickness ratio, as both parameters modify the net strain in the superlattice. The InAs/InAsSb thickness ratio is determined from the Sb shutter times and the InAs and InAsSb growth rates, thus the Sb mole fraction is the sole fitting parameter to align the superlattice satellite peaks in the dynamical X-ray diffraction simulation. This conventional approach to modeling the X-ray data results in the first set of structural parameters shown in part 3 of Table 12.

Moreover, it is observed that the InAs/InAsSb interfaces are not perfectly abrupt due to the surface segregation of Sb that is subsequently incorporated into the InAs layer after the Sb shutter is closed [61-64]. Therefore to evaluate the impact of unintentional Sb in the InAs layer, the X-ray diffraction data is further analyzed using a model with a small amount of Sb in the InAs layers. As the average unintentional Sb in the InAs is increased, the InAs layers become less tensilely strained. This modifies the net strain of the superlattice, and therefore must be compensated by a reduction in the compressive strain of the InAsSb layers so as to maintain the same net strain, i.e. the same $0^{th}$ order satellite peak position. Furthermore, as the InAsSb layers are typically not as thick as the InAs layers, one unit increase of the unintentional Sb in the InAs layer must be accompanied by a correspondingly larger decrease in the Sb mole fraction in the InAsSb layer. During this analysis it is observed that the relative intensities of the satellite peaks are sensitive to changes in the strain and the thicknesses of the constituent layers, as this

influences the structure factor for the diffraction condition of the satellite peaks [65]. Therefore in addition to those parameters fit above, the average unintentional Sb mole fraction of the InAs layer is fit to the intensity profile of the satellite peaks.

In particular, a great deal of sensitivity is obtained when one or more satellite peaks are very weak as a result of strong destructive interference for the specific structure. This is shown in Figure 34 which compares the X-ray diffraction pattern of sample E (grey curves) to the diffraction patterns simulated using average unintentional Sb mole fractions of 0.004, 0.006, and 0.008 in the InAs layers (black curves). Of particular interest are the $0^{th}$ order satellite peaks $SL_0$ and the $4^{th}$ order satellite peaks $SL_4$ that exhibit a much lower intensity than the other satellite peaks. The simulated intensity of these peaks is very sensitive to small changes of the Sb mole fraction in the InAs layer, as the $0^{th}$ order satellite peak $SL_0$ experiences increasingly stronger destructive interference with increasing Sb mole fraction whereas the $4^{th}$ order satellite peak $SL_4$ experiences increasingly stronger destructive interference with decreasing Sb mole fraction. The model simulation with an average unintentional Sb mole fraction of 0.006 provides the best fit to the overall intensity profile of sample E with an InAsSb layer Sb mole fraction of 0.322, an InAsSb layer thickness of 4.65 nm, and an InAs layer thickness of 15.23 nm.

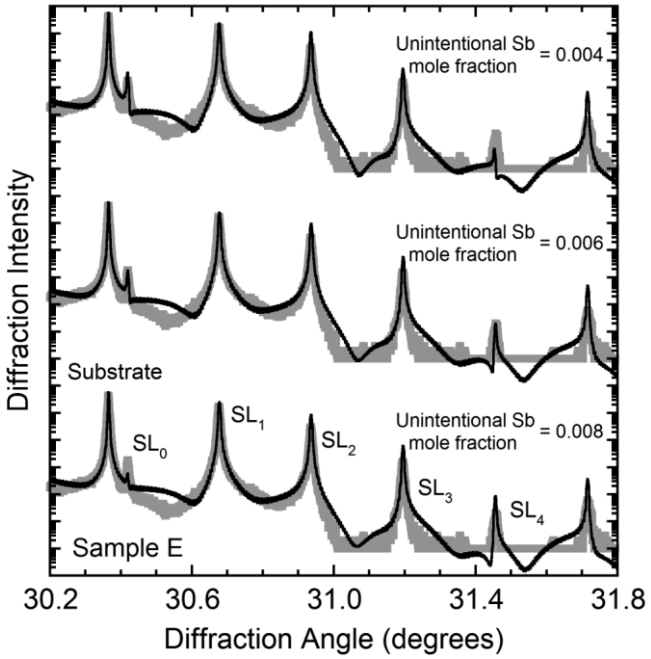


Figure 34. X-ray diffraction pattern of InAs/InAsSb superlattice sample E (grey curves) alongside diffraction patterns simulated using a structure model with average unintentional Sb mole fractions of 0.004, 0.006, and 0.008 in the InAs layers of the superlattice (black curves).

The best fit structural parameters and average unintentional Sb mole fractions of samples A through J are summarized in part 4 of Table 12. The average unintentional Sb mole fractions are about 0.006 for 15 and 18 nm thick InAs layers and are approximately double for the 5 to 8 nm thick InAs layers. The unintentional Sb is mainly incorporated near to the InAs-on-InAsSb interface [62,63] and hence decreases as the layer grows. The structural parameters that account for unintentional Sb incorporation in InAs (part 4 of Table V) are used in the assessment of the superlattice band offsets in all subsequent sections.

Photoluminescence from the InAs/InAsSb superlattice sample set is measured at 12 K using 68 mW of pump power from an 808 nm laser; this results in 90 $W \cdot cm^{-2}$ of pump power arriving at the upper superlattice interface and a carrier excitation density of $7.1 \times 10^{24}$ $cm^{-3} \cdot s^{-1}$. As the maximum in the photoluminescence first derivative with respect to photon energy accurately identifies the bandgap energies of InAsBi and InAsSb in Chapters 3 and 4, it is further utilized here to determine the 12 K ground state transition energies (effective bandgaps) of each superlattice. The normalized photoluminescence spectra of samples A, B, E, and F are plotted in Figure 35 as a function of photon energy (lower horizontal axis) and photon wavelength (upper horizontal axis). The vertical dotted lines show the ground state energy for each sample determined using the photoluminescence first derivative maximum. The ground state transition energies are listed in part 2 of Table 12 for the entire sample set expect for sample D where the photoluminescence signal is too noisy to accurately distinguish the first derivative maximum.

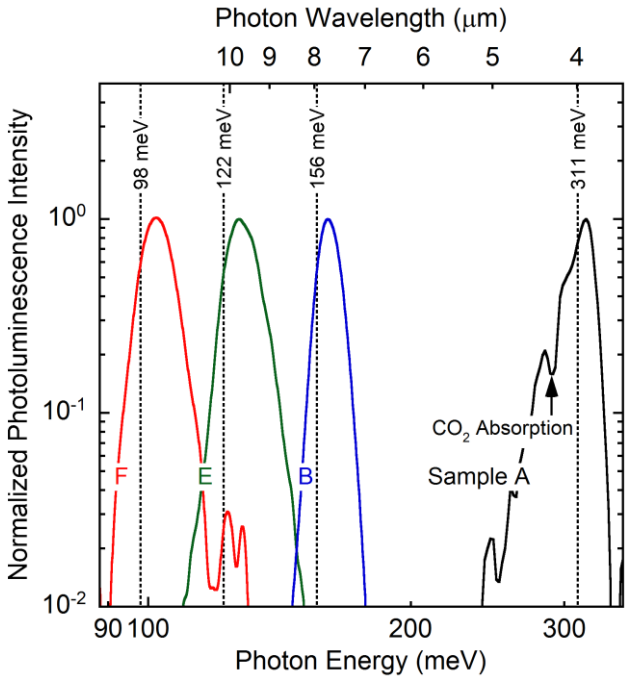


Figure 35. Normalized 12 K photoluminescence spectra from InAs/InAsSb superlattice samples A (black), B (blue), E (green), and F (red). The superlattice ground state transition energies identified from the photoluminescence first derivative maximum are indicated by vertical dotted lines.

The room temperature optical constants of the superlattice samples are measured using an infrared variable angle spectroscopic ellipsometer [38] that covers the 30 - 800 meV (40 - 1.55 μm wavelength) photon energy range. The GaSb substrate on which the superlattice is grown is transparent over much of this range, making the specular reflections from the backside of the substrate a significant concern as they are incoherent with respect to reflections from the epitaxial layers. Prior to measurement, the backside of the GaSb wafer is roughened with 400 grit sandpaper to reduce the depolarization due to backside reflections to less than 3% for all samples. A detailed description of the backside roughing procedure is given in Appendix A.

Since the superlattice region has distinctly different optical properties than the materials which compose it, the spectroscopic ellipsometry analysis utilizes a model in which the superlattice is modeled as a single layer with its own unique set of optical constants. The ellipsometric optical model of sample B is shown schematically alongside the physical cross-section in Figure 32. The WVASE software library provides optical constants of the AlSb layers, GaSb, and InAs layers [39], while the superlattice region is treated as a single layer whose optical constants are fit to the measured reflection. The process of modeling a superlattice as a single layer and fitting its optical constants has been shown to be successful in GaAs/AlGaAs [66,67] and InAs/GaInSb [68] superlattices. A point-by-point analysis [40] of the measured ellipsometric parameters, $\Psi$ and $\Delta$, provides the refractive index $n$, the extinction coefficient $k$, and the absorption coefficient $\alpha = 4\pi k/\lambda$ of the InAs/InAsSb superlattice.

The point-by-point optical constants are modeled using the general oscillator model with a PSEMI0 oscillator at the effective bandgap of the superlattice and Gaussian oscillators above the bandgap, producing another set of optical constants that are Kramers-Kronig consistent [41-43]. The point-by-point (black curves) and oscillator model (grey curves) optical constants of InAs/InAsSb superlattice sample B are compared in Figure 36, and close agreement between the two sets of curves indicates that the point-by-point fitted optical constants are Kramers-Kronig consistent. As the point-by-point optical constants have no built-in smoothing as the oscillator model does, the point-by-point optical constants are more closely related to the actual measurement and are therefore preferred and utilized exclusively in the analysis that follows. In particular, the room temperature ground state transition energies of the superlattice samples are

identified from the absorption coefficient spectra using the first derivative maximum that identifies the rapid increase in the optical joint density of states at the ground state transition of the superlattice. The room temperature ground state transition energies of each InAs/InAsSb superlattice determined using spectroscopic ellipsometry are summarized in part 2 of Table 12.

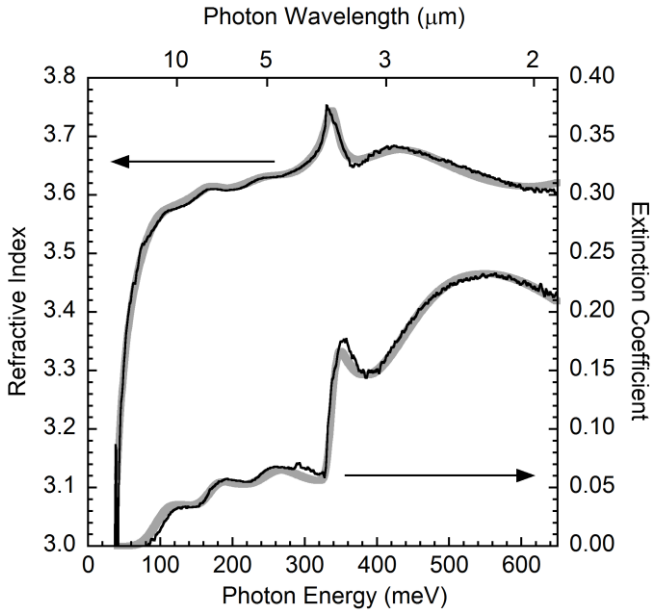


Figure 36. Refractive index (left-hand vertical axis) and extinction coefficient (right-hand vertical axis) of a strain-balanced InAs/InAsSb superlattice (sample B) plotted as a function of photon energy (lower horizontal axis) and photon wavelength (upper horizontal axis). The optical constants identified using point-by-point and oscillator fitting analyses are shown with black and grey curves.

## 4.3 InAs/InAsSb Superlattice Miniband Structure Modeling

The superlattice miniband structure and the electron and hole wavefunctions are calculated so that features in the measured room temperature absorption coefficient can be attributed to optical transitions in the superlattice. The band structure calculations utilize conventional III-V semiconductor parameters from [3], which are detailed in Table 13. The modification to the InAs and InAsSb bandgaps due to strain is accounted for using the Pikus-Bir Hamiltonian [46,47] and the superlattice miniband energies and wavefunctions are calculated using the Kronig-Penney model [69-71]. As the strained band alignment between InAs and InAsSb is not precisely known, the strained valence band offset is used as a fitting parameter to align the calculated ground state transition energy between the first electron and first heavy hole minibands to the effective bandgap measured using photoluminescence at low temperature and spectroscopic ellipsometry at room temperature.

Table 13. Material parameters for InAs and InSb used in the Kronig-Penney model of the InAs/InAsSb superlattice miniband structure. The bandgap of InAsSb is calculated using the 938 and 750 meV low and room temperature bowing parameters from Section 4.1, and the electron effective mass is calculated using a bowing parameter of 0.035 [3]. All other parameters are assumed to vary linearly with mole fraction between the respective values of InAs and InSb. The room temperature bandgap values are from this work (Section 4.1) and all other parameter values are taken from [3].

| Material parameter | InAs | InSb |
|---|---|---|
| Low temperature bandgap (meV) | 417 | 235 |
| Room temperature bandgap (meV) | 354 | 172 |
| Low and room temperature valence band edge (meV) | -590 | 0 |
| Poisson's ratio | 0.3521 | 0.3530 |
| Conduction band deformation potential (eV) | -5.08 | -6.94 |
| Valence band deformation potential (eV) | -1.00 | -0.36 |
| Shear deformation potential (eV) | -1.80 | -2.00 |
| Electron effective mass | 0.0260 | 0.0135 |
| Heavy hole effective mass | 0.3333 | 0.2632 |
| Lattice constant (nm) | 0.60582 | 0.64792 |

The room temperature energy band diagram of one InAs/InAsSb superlattice is shown in Figure 37. The structure of this superlattice is that of sample B in Table 12 with the 0.8% unintentional Sb included in the analysis of the band alignment and miniband structure. The conduction band edges of InAs and InAsSb are represented with dotted green lines, and the electron minibands that form due to the periodic potential in the conduction band are represented by green bands that extend in the growth direction $z$. The electron minibands are labeled $e_1$, $e_2$, and $e_3$ to indicate the first, second, and third electron minibands in the superlattice. Similarly in the valence band, the heavy and light hole band edges of InAs and InAsSb are represented with dotted dark blue and light blue lines respectively, and the heavy and light hole minibands ($hh_1$, $hh_2$, $lh_1$, etc.) are represented by solid dark blue and light blue bands. Transition energies are calculated between electron and hole minibands based on crystal momentum conservation shown on the right-hand side of the figure as a function of the superlattice reciprocal lattice vector $k_z$. The electron-hole wavefunction overlap integral reveals which transitions are active in absorption, and several high wavefunction overlap optical transitions are shown on the figure. The selection rule which would forbid some of these transitions in an infinite quantum well is not a factor in the type-II superlattice because the carriers are primarily localized in different layers; electrons in InAs and holes in InAsSb.

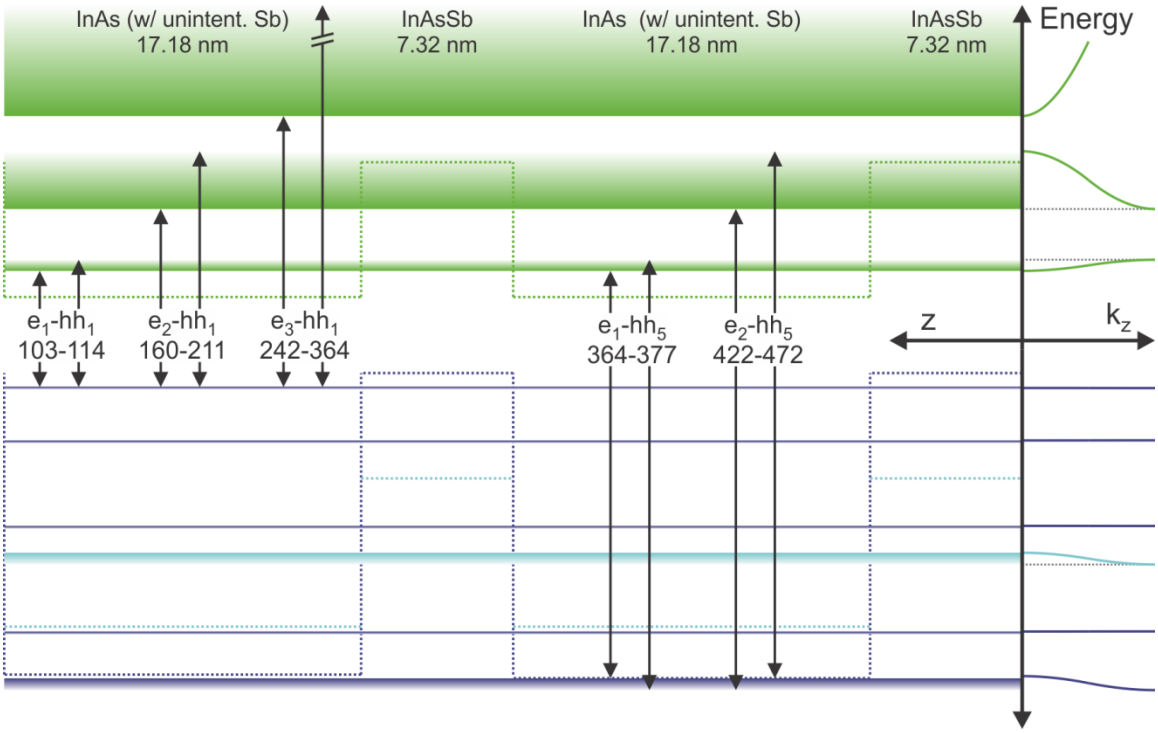


Figure 37. Room temperature energy band diagram (left) and dispersion relation (right) of a strain-balanced InAs/InAsSb superlattice (sample B). The bulk conduction band edge is represented with the dotted green line and the electron minibands ($e_1$, $e_2$, $e_3$) with the solid green bands. The heavy and light hole bulk band edges are represented with the dotted dark blue and light blue lines, and the heavy and light hole minibands ($hh_1$, $hh_2$, $lh_1$, etc.) with the solid dark blue and light blue bands respectively. Optical transitions between minibands with high wavefunction overlap are labeled in the figure, and the dispersion relationship (right-hand side of the figure) shows the crystal momentum of the electron-hole pair that interacts with the photon.

Figure 38 shows the absorption coefficient of the same superlattice (sample B) measured by spectroscopic ellipsometry, with the same high wavefunction overlap optical transitions present in the band structure of Figure 37 indicated in Figure 38. The onset of absorption occurs at the ground state transition between the first electron and first heavy hole minibands, labeled $e_1 - hh_1$ in each figure. The square of the wavefunction overlap integral at the ground state of sample B is 10.25%, which enables the absorption coefficient to rise sharply to 456 $cm^{-1}$ at which point the absorption coefficient plateaus. With increasing energy, the absorption coefficient increases in steps with the onsets of higher order optical transitions ($e_2 - hh_1$, $e_3 - hh_1$, $e_1 - hh_5$, etc.) just as the density of states increases in steps which are broadened by the bandwidths of the minibands [72]. The wavefunctions within a miniband are modified with increasing energy through the miniband, resulting in wavefunction overlap integrals which exhibit peak values at the energies indicated in the figure and generally approach zero with increasing or decreasing photon energy; this characteristic of the wavefunction overlap integral is indicated in Figure 38 via the red color gradient of each transition.

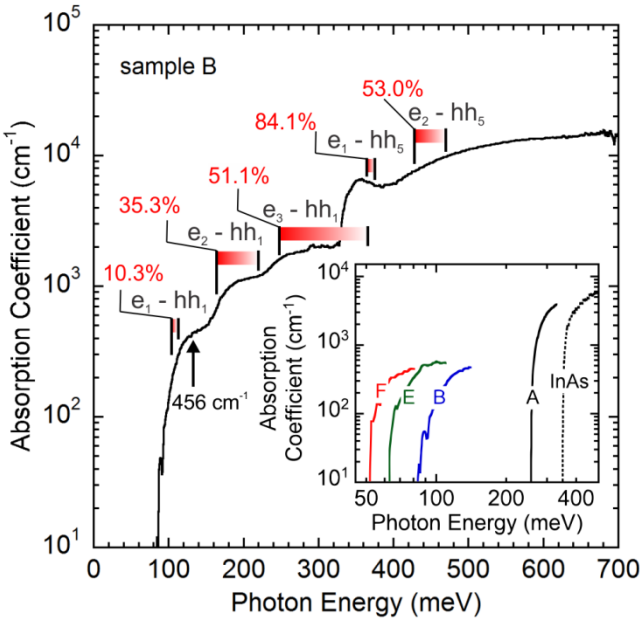


Figure 38. Room temperature absorption coefficient of strain-balanced InAs/InAsSb superlattice sample B measured using spectroscopic ellipsometry. The optical transitions with significant wavefunction overlap square are indicated as a percentage in red, with the red color gradient showing how the wavefunction overlap changes with energy. The inset shows the absorption onsets of selected superlattice samples alongside bulk InAs.

The inset to Figure 38 shows the absorption onsets of selected samples from Table 12 (solid curves) which demonstrates a 56 to 260 meV range of superlattice effective bandgaps. In addition, the absorption coefficient of bulk InAs measured and discussed in Section 4.1 is shown as a dotted line for comparison. For a constant period thickness, increasing Sb mole fraction in the InAsSb layers has the effect of increasing the offset of the type-II band alignment between InAsSb and InAs, thereby reducing the superlattice ground state transition energy. The unintentional Sb content (0.006 to 0.008) and period thicknesses (20 – 25 nm) of samples B, E, and F are comparable, and the

energy shift to decreasing energies is due to the increasing Sb mole fraction of each sample (0.263 Sb for sample B, 0.322 Sb for sample E, and 0.338 Sb for sample F). Furthermore, the square of the wavefunction overlap integrals of these three samples are also close in magnitude (10.25% for sample B, 12.12% for sample E, and 7.74% for sample F) owing to the similar period thicknesses of the three samples. The ground state absorption coefficients are also similar in magnitude, with sample E (10.25% wavefunction overlap square) attaining the highest absorption coefficient of the three.

In general, shorter period thickness superlattice designs allow for stronger coupling of the electron and hole wavefunctions and larger wavefunction overlap. Sample D (0.279 Sb) has an Sb mole fraction between that of samples B (0.263 Sb) and E (0.322 Sb), but has a larger cutoff energy (136 meV) and larger wavefunction overlap square (30.51%) than samples B or E owing to its significantly shorter period thickness of 10.7 nm. Similar to sample D, sample A also has a relatively shorter period thickness (9.9 nm compared to 10.7 nm) but with a smaller Sb mole fraction (0.117 Sb compared to 0.279 Sb) resulting in a larger cutoff energy and wavefunction overlap square (260 meV compared to 136 meV, 65.31% compared to 30.51% wavefunction overlap square).

## 4.4 InAs/InAsSb Superlattice Band Alignment

In the analysis of the InAs/InAsSb superlattice miniband structure discussed thus far, the strained band alignment between InAs and InAsSb has been utilized as a fitting parameter to align the calculated superlattice ground state transition energies to those measured experimentally using spectroscopic ellipsometry at room temperature. The

same analysis is also performed at low temperature using the 12 K ground state transition energies measured using photoluminescence spectroscopy in part 2 of Table 12. The strained band alignment is characterized by the strained valence band offset, $\Delta E_v(x)$, between the $InAs_{1-x}Sb_x$ heavy hole valence band edge $E_v(x)$ and the InAs heavy hole valence band edge $E_v(0)$; see Figure 39 inset. The strained valence band offsets, $\Delta E_v(x) = E_v(x) - E_v(0)$, determined at low temperature (blue squares) and room temperature (red circles) are plotted as a function of Sb mole fraction in Figure 39.

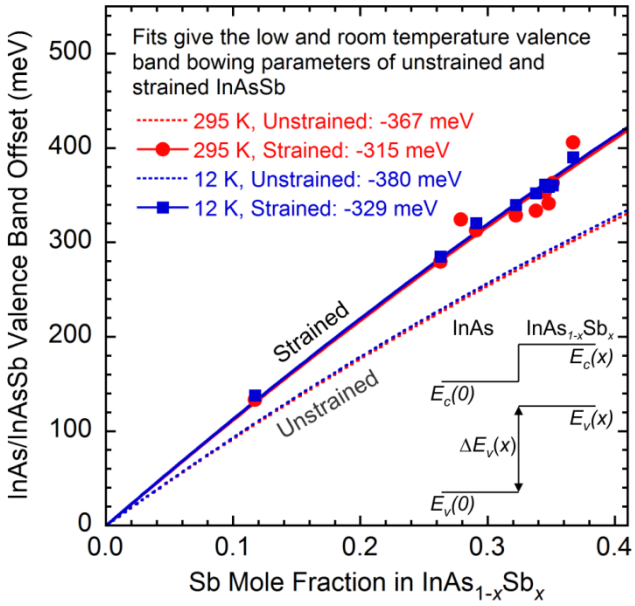


Figure 39. Heavy hole valence band edge of $InAs_{1-x}Sb_x$ relative to InAs, $\Delta E_v(x)$ shown by the inset diagram, plotted as a function of Sb mole fraction at 295 K (red circles) and 12 K (blue squares). The solid curves represent bowing model fits to the strained band offset data. The analysis for unstrained bulk material is shown as dotted curves obtained by backing out the effect of strain to the GaSb substrate.

The valence band edge bowing model shown in Equation 11 is fit to the strained data in Figure 39; the best fits are shown as the solid red curve for the room temperature result and the solid blue curve for the low temperature result. Since the valence band edges of InAs and InSb, $E_v(0)$ and $E_v(1)$, are known [3,46,47], the valence band bowing parameter, $b_v$, is a fitting parameter whose best fit values are given in Table 14. The unstrained valence band offsets (dotted curves) are determined by backing out the effects of the InAs tensile strain and the InAsSb compressive strain on the valence band using the Pikus-Bir Hamiltonian [46,47]. The resulting low and room temperature InAsSb band alignment is shown in Figure 40; (a) unstrained and (b) coherently strained on GaSb.

$$\Delta E_v(x) = x\Delta E_v(1) - x(1-x)b_v \tag{11}$$

Table 14: Bowing parameters for the bandgap ($b_g$), valence band ($b_v$), and conduction band ($b_c$) of unstrained bulk InAsSb and coherently strained InAsSb on GaSb.

| | | Bowing parameters | |
|---|---|---|---|
| | | at 295 K (meV) | at 12 K (meV) |
| Unstrained | $b_g$ | 750 | 938 |
| | $b_v$ | -367 | -380 |
| | $b_c$ | 383 | 558 |
| Strained on GaSb | $b_g$ | 783 | 971 |
| | $b_v$ | -315 | -329 |
| | $b_c$ | 468 | 642 |

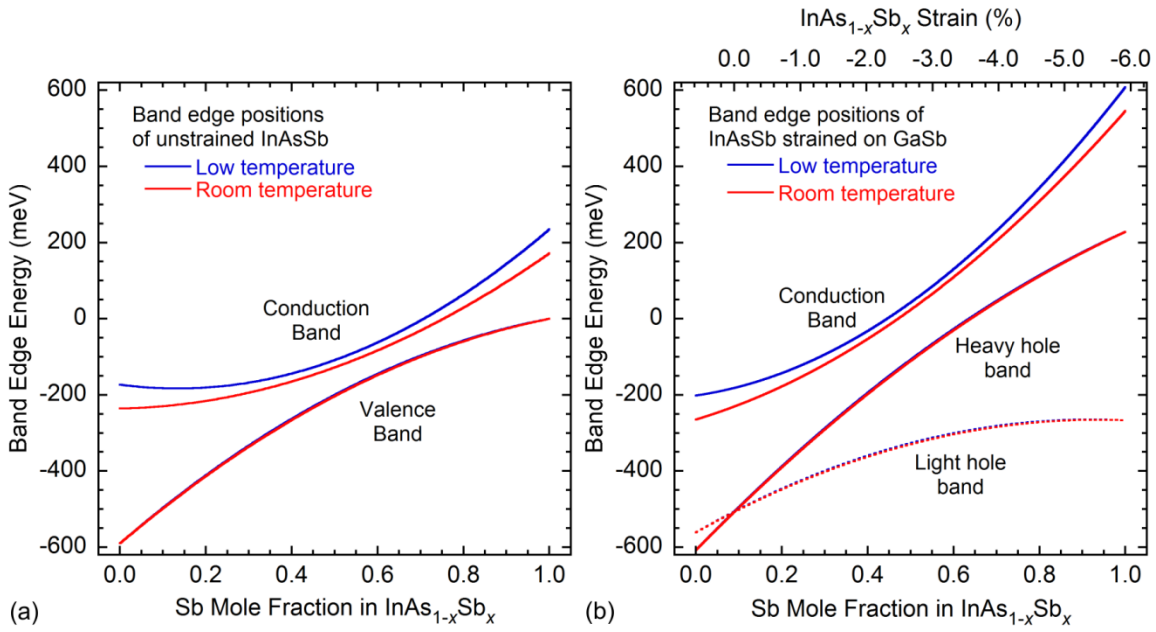


Figure 40. Conduction and valence band edge positions relative to the unstrained InSb valence band edge for bulk InAsSb at low temperature (blue curves) and at room temperature (red curves). (a) shows the band alignments for unstrained InAsSb as a function of Sb mole fraction and (b) shows the band alignments for InAsSb coherently strained on GaSb as a function of Sb mole fraction (lower horizontal axis) and strain (upper horizontal axis).

The valence band bowing parameters ($b_v$) determined in Figure 39, the bandgap bowing parameters ($b_g$) determined in Section 4.1, and the resulting conduction band bowing parameters given by $b_c = b_v + b_g$, are summarized in Table 14. The band bowing is upward (negative) for the valence band and downward (positive) for the conduction band, with a resultant downward (positive) bowing for the bandgap. Figure 40a shows the unstrained band edge positions of InAsSb as a function of mole fraction. In the absence of strain, InAsSb forms a weak type-I band alignment with InAs

for low Sb mole fractions and a type-II band alignment at higher mole fractions. The percentage of the total bandgap bowing attributed to the valence band at low temperature is 41%, which is consistent with other reports [73,74].

When the material is coherently strained on GaSb the band bowing decreases in the valence band and increases in the conduction band and bandgap. In general, for ternary materials, the shift in the band edges with biaxial strain is not linear as the strain, the deformation potentials, and Poisson's ratio all are typically functions of mole fraction. In coherently strained InAsSb on GaSb, the variation in the deformation potentials with mole fraction is the dominant factor that modifies the strained bowing parameters. In the conduction band for example, the conduction band deformation potential changes from -5.08 eV for InAs to -6.94 eV for InSb. As a result, the strained conduction band edge moves to higher energies with increasing Sb mole fraction at a greater rate than it would if the deformation potential were constant. The same is true in the valence band which is modified by a combination of the valence band and shear deformation potentials. This results in a larger strained band edge bowing parameter and a stronger type-II band alignment in strain-balanced InAs/InAsSb (see Figure 40b).

If the structural parameters (InAs/InAsSb thicknesses and mole fractions) that assume no unintentional Sb incorporation (part 3 of Table 12) are used for this analysis, the measured band offsets would remain virtually unchanged; however, the Sb mole fractions of the InAsSb layers would all increase by 0.01 to 0.05. This would produce a horizontal right shift in the data in Figure 39 that would result in a significant change in the distribution of the band edge bowing. In particular, 12% of the bandgap bowing

would transfer from the valence band to the conduction band at low temperature and 18% at room temperature. These results indicate that the unintentional incorporation of Sb into the InAs layers of the superlattice should not be ignored in this analysis.

The InAsSb bandgap and band edge bowing parameters in Table 14 are programmed into the Kronig-Penney software model, allowing more accurate miniband structure calculations to be performed. Table 15 compares the ground state transition energies of the superlattice samples detailed in Table 12 alongside the transition energies calculated in the updated Kronig-Penney model. Close agreement is obtained between theory and experiment, ultimately indicating that this software is capable of making accurate band structure predictions; these functionalities will be further explored in Chapter 5.

Table 15: Low and room temperature ground state transition energies of InAs/InAsSb type-II superlattices. The experimental values are determined using photoluminescence spectroscopy at low temperature and spectroscopic ellipsometry at room temperature (see Table 12), and the calculated values are determined using a Kronig-Penney model and the material parameters detailed in Tables 13 and 14.

| | Low temperature transition energies (meV) | | Room temperature transition energies (meV) | |
|---|---|---|---|---|
| Sample | Experimental | Calculated | Experimental | Calculated |
| A | 311 | 314.0 | 260 | 261.5 |
| B | 156 | 157.5 | 103 | 102.2 |
| C | 128 | 136.5 | 76 | 80.3 |
| D | ... | 207.9 | 136 | 156.0 |
| E | 122 | 121.0 | 74 | 65.9 |
| F | 98 | 94.8 | 56 | 38.4 |
| G | 102 | 101.0 | 51 | 45.8 |
| H | 106 | 100.5 | 64 | 45.5 |
| I | 162 | 156.6 | 107 | 105.5 |
| J | 134 | 139.4 | 68 | 87.9 |

## 4.5 InAs/InAsSb Superlattice Absorption Properties

In addition to providing a measurement of the ground state transition energy, spectroscopic ellipsometry also gives information on the absorption properties of the superlattice, an important design consideration. The absorption coefficient of each InAs/InAsSb superlattice (provided in part 5 of Table 12) is used to determine the transition strength $S$ [75], a dimensionless quantity which provides a measure of the strength of the optical transition independent of the optical joint density of states. The transition strength can be expressed as a function of either the momentum matrix element

$\langle \Psi_h | \mathbf{p} | \Psi_e \rangle$ in Equation 12a or the dipole matrix element $\langle \Psi_h | \mathbf{r} | \Psi_e \rangle$ in Equation 12b [76]. On the other hand, the absorption coefficient is also a function of the matrix element, as well as the refractive index $n$, the speed of light $c$, the vacuum permittivity $\varepsilon_0$, the rest mass of the electron $m_0$, and the electron charge $e$. By rearranging the expression for the absorption coefficient $\alpha$ given in Equations 13a or 13b [76], the transition strength can be determined experimentally from the absorption data by dividing the absorption coefficient by the optical joint density of states $\rho$ as shown in Equation 14.

$$S = \left(\frac{2}{m_0}\right) \frac{|\langle \Psi_h | \mathbf{p} | \Psi_e \rangle|^2}{h\nu} \tag{12a}$$

$$S = \left(\frac{2m_0}{\hbar^2}\right) (h\nu) |\langle \Psi_h | \mathbf{r} | \Psi_e \rangle|^2 \tag{12b}$$

$$\alpha = \left(\frac{\pi \hbar e^2}{nc\varepsilon_0 m_0^2}\right) \left(\frac{1}{h\nu}\right) (\rho) |\langle \Psi_h | \boldsymbol{p} | \Psi_e \rangle|^2 \tag{13a}$$

$$\alpha = \left(\frac{\pi e^2}{\hbar nc\varepsilon_0}\right) (h\nu)(\rho) |\langle \Psi_h | \boldsymbol{r} | \Psi_e \rangle|^2 \tag{13b}$$

$$S = \left(\frac{2nc\varepsilon_0 m_0}{\pi \hbar e^2}\right) \left(\frac{\alpha}{\rho}\right) \tag{14}$$

The refractive index in the vicinity of the superlattice ground state is ~3.6 for all samples examined. For each sample of period thickness $d$, the transition strength is determined at the photon energy at which the optical joint density of states $\rho$ reaches its ground state constant level $\rho_0$ given by Equation 15 [72]. The reduced mass of the electron-hole pair, $m_r^{-1} = m_e^{-1} + m_{hh}^{-1}$, is calculated using the miniband edge electron and heavy hole effective masses; however since the heavy hole effective mass is much larger than the electron effective mass, the reduced mass is essentially just the electron

effective mass, $m_r = m_e$. The electron effective mass is calculated using Equation 16 in which $p$ is the electron momentum $\hbar k$, $v_g$ is the group velocity $\frac{1}{\hbar} \times \frac{dE_k}{dk}$, and $E_k$ is the dispersion relation in the ground state electron miniband with bandwidth $E_e$ given by Equation 17 [13]. Substituting Equation 17 into Equation 16 and performing the first derivative results in the electron effective mass given by Equation 18. By substituting this expression for the electron effective mass into Equation 15, a simplified expression for $\rho_0$ is obtained in Equation 19 which is only a function of the superlattice period thickness $d$ and the ground state electron bandwidth $E_e$ which is calculated in the Kronig-Penney model. Finally, by incorporating this expression for the ground state density of states into Equation 14, the transition strength can be written in terms of these same parameters and the measured ground state absorption coefficient in Equation 20.

$$\rho_0 = {}^{m_r}/_{\hbar^2 \pi d} = {}^{m_e}/_{\hbar^2 \pi d} \tag{15}$$

$$m_e = \frac{p}{v_g} = \frac{(\hbar k)}{\left(\frac{1}{\hbar} \times \frac{dE_k}{dk}\right)} \tag{16}$$

$$E_k = E_e(1 - \cos(kd))/2 \tag{17}$$

$$m_e = \frac{\hbar^2 k}{\left(\frac{E_e d}{2}\right)\sin(kd)}\Bigg|_{k=0} = \frac{2\hbar^2}{E_e d^2} \tag{18}$$

$$\rho_0 = {}^{m_e}/_{\hbar^2 \pi d} = {}^{2}/_{\pi E_e d^3} \tag{19}$$

$$S = \left(\frac{m_0}{m_e}\right)\left(\frac{2\hbar n c \varepsilon_0}{e^2}\right)(\alpha_0 d) = \left[\frac{nc\varepsilon_0 m_0}{\hbar e^2}\right](\alpha E_e d^3) \tag{20}$$

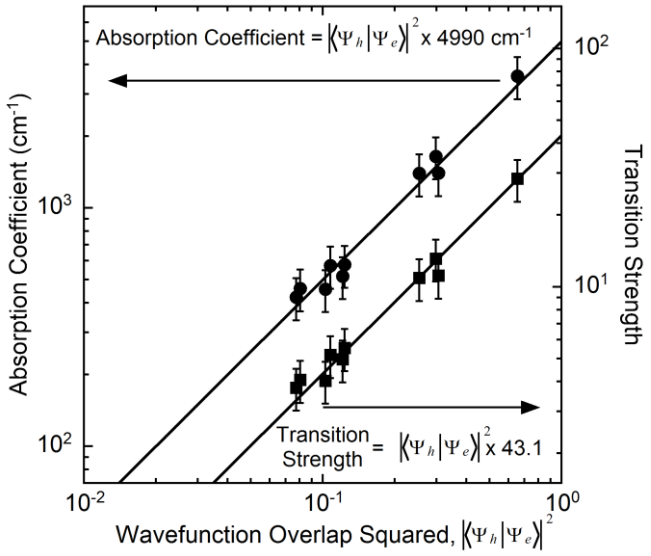


Figure 41. Room temperature absorption coefficient for the ground state optical transition in strain-balanced InAs/InAsSb superlattices plotted on the left-hand vertical axis (circles) as a function of the square of the wavefunction overlap integral. The transition strength, which is proportional to the absorption coefficient over the optical joint density of states, is plotted on the right-hand vertical axis (squares). A unity power law is observed for both sets of data, indicating that the ground state absorption coefficient is mainly proportional to wavefunction overlap squared.

Figure 41 shows the measured ground state absorption coefficient (left-hand vertical axis) and transition strength (right-hand vertical axis) plotted as a function of the square of the wavefunction overlap at the ground state for the samples presented in Table 12. The calculated values of $\rho_0$ from which the transition strengths are determined are listed in part 5 of Table 12. The solid lines are linear fits to the absorption coefficient (solid circles) and transition strength (solid squares), with best fit slopes 4990 ± 317 cm$^{-1}$ and 43.1 ± 2.7, respectively. The error bars indicate an uncertainty of ± 20% in the measured absorption coefficient and the inferred transition strength. This uncertainty is

estimated from the sensitivity of the magnitude of the superlattice absorption to the transparency of the GaSb substrate used in the ellipsometric model. For example, the superlattice ground state absorption coefficient increases by ~10% per 100 $cm^{-1}$ increase in the absorption coefficient of the substrate. Since the database used in the analysis assumes the GaSb is transparent over the wavelength range of interest, the presence of any free carrier absorption in the GaSb introduces a small uncertainty in the analysis of the fraction of radiation absorbed in the superlattice. Nevertheless, since it is observed that roughening the substrate backside greatly reduces the intensity of the long wavelength radiation reflected from the backside of the substrate, the GaSb substrates are at least partially transparent (< 100 $cm^{-1}$), and the presence of free carrier absorption in the substrate is not expected to significantly impact the results.

It is observed that the absorption coefficient and transition strength are proportional to the square of the wavefunction overlap, indicating that the variation in the optical joint densities of states at the top of the minibands is small; the calculations show that the average value of the density of states varies less than 10% between samples. An increase in the period thickness of the superlattice, which lies in the denominator of the expression for the superlattice density of states (Equation 19), is partially compensated by the miniband bandwidth which simultaneously decreases due to reduced wavefunction coupling. This compensating effect explains why the densities of states do not change significantly from sample to sample over the range of period thicknesses examined in this study. The validity of this equation breaks down if the period thickness is very long or very short as the effective mass is no longer accurately described by the bandwidth of the first electron miniband, and instead converges to the effective mass of bulk material.

Extrapolation of the absorption coefficient data in Figure 41 indicates that as the wavefunction overlap approaches 100%, the ground state absorption coefficient and transition strength of the superlattice approach 4990 $cm^{-1}$ and 43.1 respectively. The optical joint density of states is weakly dependent on the superlattice period thickness and Sb mole fraction and is similar in magnitude to that of bulk material.

These results indicate that the optical joint density of states is a minor design parameter in optimizing superlattice absorption. While decreasing the superlattice period thickness of a strain-balanced InAs/InAsSb superlattice does in general lead to improved wavefunction overlap, it also increases the confinement offsets which act to increase the ground state transition energy. As a result, a larger Sb mole fraction is required to keep the ground state transition energy constant while maintaining strain-balance. Increasing Sb mole fraction in the InAsSb layers of the superlattice will increase the confinement of electrons and holes in the superlattice, causing a reduction in wavefunction overlap. Thus there are two competing effects in the design, increasing wavefunction overlap with decreasing period thickness and decreasing wavefunction overlap with increasing Sb mole fraction, leading to an optimal superlattice design which does not necessarily utilize the smallest period thickness and largest Sb mole fraction to maximize wavefunction overlap. By utilizing wavefunction overlap as a design parameter, the set of superlattice designs which achieve maximum absorption strength can be determined as a function of ground state transition energy.

## 4.6 Chapter 4 Summary

Several InAs/InAsSb superlattices are examined that have period thicknesses ranging from 10 to 25 nm, Sb mole fractions ranging from 12% to 37%, and bandgap energies that range from 98 to 311 meV (12.7 to 4.0 μm) at low temperature and 51 to 260 meV (24.3 to 4.8 μm) at room temperature. An average unintentional incorporation of ~1% Sb in the InAs layer is taken into consideration in the analysis of the InAs/InAsSb band offset for each sample composition determined using X-ray diffraction, spectroscopic ellipsometry, and photoluminescence spectroscopy, and measurements of the bandgap energy of bulk $InAs_{0.911}Sb_{0.089}$. The composition dependent InAsSb bandgap and InAs/InAsSb band edge positions are parameterized using bowing models, and it is found that ignoring the small amount of unintentional Sb in the InAs layer results in a significant change in the observed band edge bowing. The superlattice absorption coefficient is proportional to the square of the wavefunction overlap in the superlattice, indicating that the ground state absorption strength is not strongly dependent on the optical joint density of states of the particular superlattice design. It is observed that InAs/InAsSb superlattices are capable of attaining absorption coefficients comparable to bulk material despite relying on type-II band alignment to reach longer wavelengths, and that wavefunction overlap should be the principle design consideration for optimizing absorption in these structures.

# 5. OPTIMIZATION OF SUPERLATTICE DESIGNS

A software package is developed which calculates the miniband structure of semiconductor superlattices and identifies optimal designs in terms of maximizing wavefunction overlap as a function of ground state transition energy. By sweeping alloy compositions and layer thicknesses which are selected to obtain strain-balance or lattice-match to the underlying substrate, only designs that can be grown with zero net in-plane strain are considered. The result is a set of designs at a single lattice constant having at least two free parameters, which may then be further reduced to a smaller subset of designs which maximize wavefunction overlap as a function of transition energy. These functionalities are demonstrated by mapping the design spaces of lattice-matched GaSb/$InAs_{0.911}Sb_{0.089}$ and GaSb/$InAs_{0.932}Bi_{0.068}$ superlattices and strain-balanced InAs/InAsSb, InAs/GaInSb, and InAs/InAsBi superlattices on GaSb substrates. Optimal design criteria are identified at key photon wavelengths which are utilized in the growth and characterization of a strain-balanced InAs/InAsSb superlattice designed for optimal absorption in the mid-wave infrared.

## 5.1 Optimal Design Software

A software package designed to optimize superlattice absorption properties is built around the calculations utilized to examine the InAs/InAsSb superlattice band structure in Chapter 4. In this software, the bulk material parameters needed to calculate the superlattice miniband structure are the bandgap energy, valence band edge, lattice

constant, Poisson's ratio, deformation potentials, and effective masses of each of the superlattice constituents. The design calculations utilize conventional III-V semiconductor parameters taken from a review article published in 2001 [3], and other parameters detailed in this section.

The bandgaps and valence band edges of InAsSb and GaInSb are characterized by bowing model relationships. The bandgap and valence band bowing parameter of InAsSb are determined as a function of temperature in Chapter 4 of this work; the bandgap bowing parameter of InAsSb is 938 meV at low temperature and 750 meV at room temperature, and the valence band bowing parameter of InAsSb is -380 meV at low temperature and -367 meV at room temperature [4]. The bandgap bowing parameter of GaInSb is 413 meV at low temperature and 398 meV at room temperature [78]. The valence band bowing parameter of GaInSb is zero, which implies that the bandgap bowing occurs entirely in the conduction band of GaInSb; no temperature dependence has been reported [3]. The InAsBi material parameters are determined in Chapter 3 of this work (see Tables 4 and 5), and the Bi coupling parameter is assumed to be independent of temperature to calculate the InAs/InAsBi band alignment at low temperature.

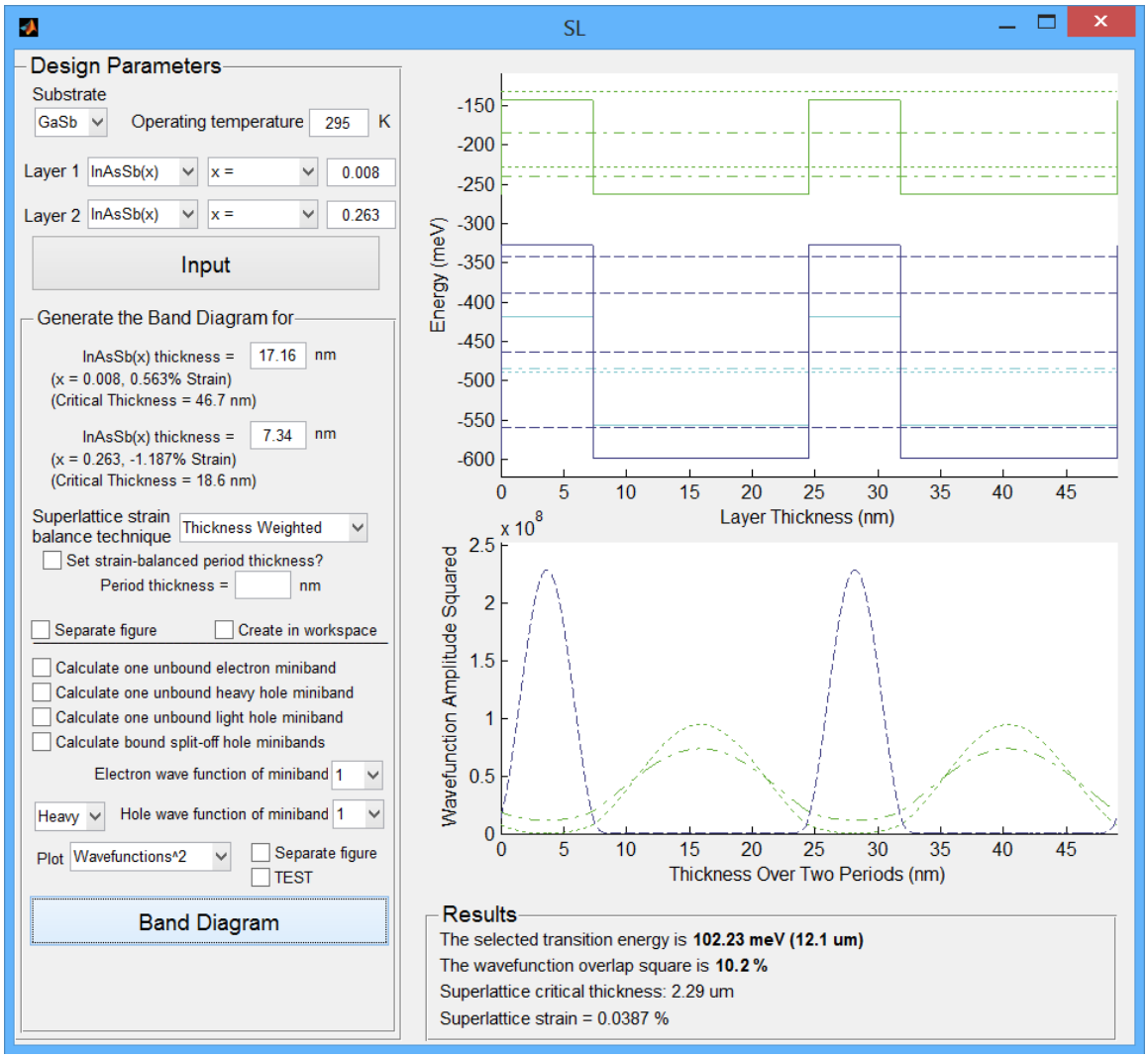


Figure 42. Graphical user interface of the software tool which calculates the ground state and higher order miniband transitions in the band structure of semiconductor superlattices. Design parameters such as the substrate, superlattice constituents, and thicknesses are input to the left. The superlattice band alignment, wavefunctions, and other key results are output to the right.

The strained band alignment of the superlattice is established using the Pikus-Bir Hamiltonian [46,47], and the electron, heavy hole, and light hole miniband energies and wavefunctions are calculated using the Kronig-Penney model [69-71]. These

functionalities are written into functions called by a graphical user interface developed in the Graphical User Interface Design Environment in MATLAB [79]. Figure 42 shows this software tool, referred to as the *Superlattice Miniband Structure Tool*, which calculates the superlattice band edge diagram and the electron and hole wavefunctions. Design parameters such as the substrate, the superlattice constituents, the layer thicknesses, etc. are input in the editable text fields on the left side of the user interface, and the band edge diagram and wavefunctions are plotted in the space to the right. The particular design parameters shown in Figure 42 are the ones which produce the band diagram of InAs/InAsSb superlattice sample B in Figure 37, however the tool has the capability to calculate the miniband structure of any conceivable III-V, II-VI, or group IV semiconductor superlattice on any desired substrate.

For a superlattice composed of a binary and a ternary alloy, the ternary composition and the individual layer thicknesses of the two repeating layers constitute three design parameters. However in order to grow an arbitrarily thick superlattice region without lattice relaxation, either a lattice-matched or strain-balanced superlattice must be utilized [18] which reduces the number of free parameters to two. In the case of lattice-matched structures the free parameters are the thicknesses of the two lattice-matched layers, and in the case of strain-balanced structures the free parameters are the ternary layer composition and the superlattice period thickness. Using the superlattice, only one of the two remaining design parameters is necessary to tune the ground state transition energy, leaving the second parameter available for the optimization of the electron-hole wavefunction overlap, which is proportional to the absorption coefficient [19]. Therefore

in a superlattice system with at least two free design parameters the absorption coefficient can be optimized as a function of detector wavelength.

While the *Superlattice Miniband Structure Tool* is useful for evaluating the detailed optical performance of a single superlattice design, the actual design space calculation is performed using two other software tools, referred to as the *Strain-Balanced* and *Lattice-Matched Design Tools,* which calculate the ground state transition energy (effective bandgap) and wavefunction overlap square as a function of the free design parameters in strain-balanced and lattice-matched material systems. The interfaces to the these software tools are shown in Figures 43 and 44, both of which utilize editable text fields in the upper part of the interface to define the free design parameters of the superlattice and generate the design curves in the lower part of the interface which give a quick "at a glance" view of the limits of ground state absorption and emission in the design space. The calculated results are saved in matrix format in the MATLAB workspace for design optimization using the fourth software tool referred to as the *Superlattice Optimal Design Tool*.

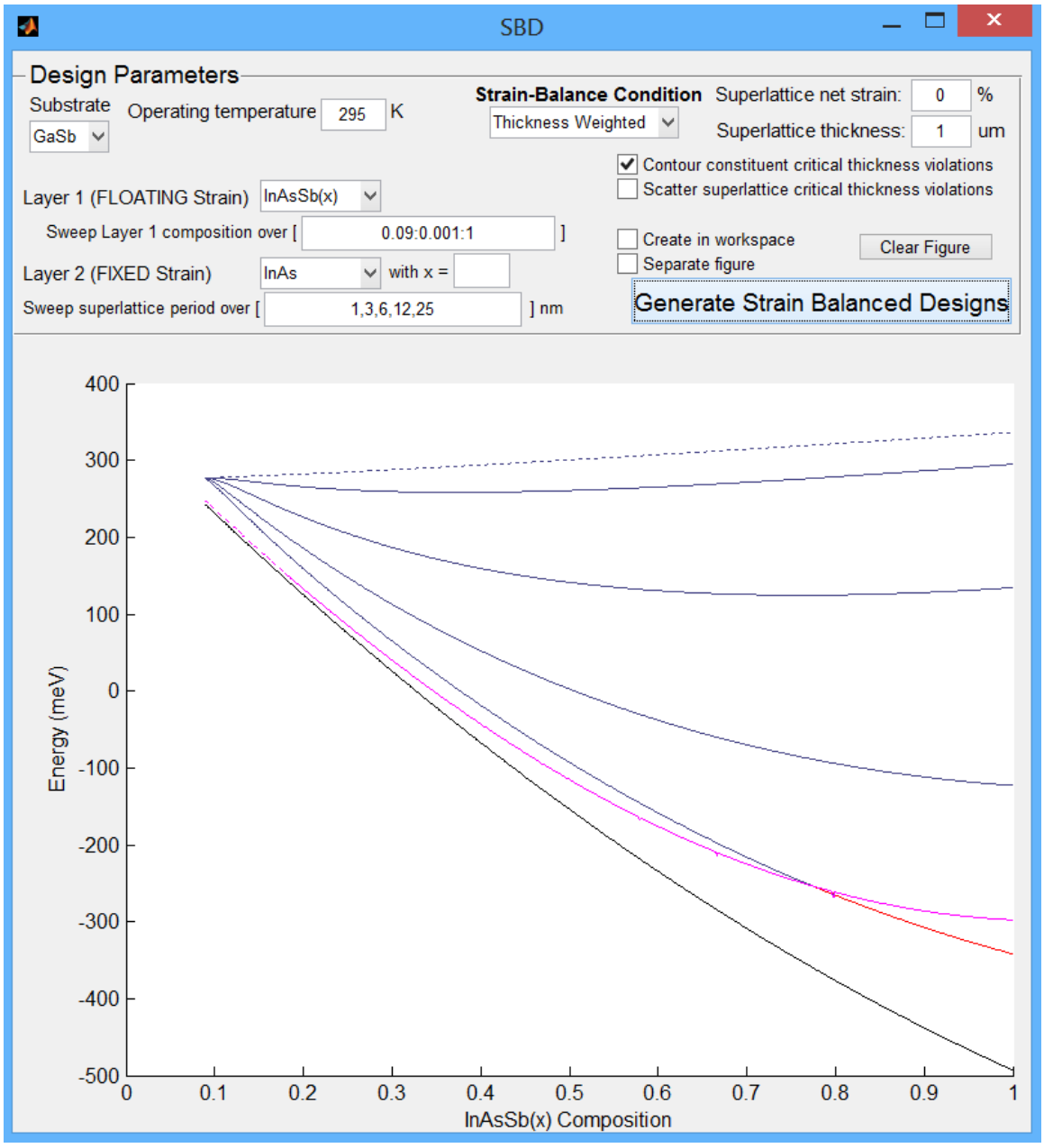


Figure 43. Graphical user interface of the software tool which calculates the ground state transition energy and wavefunction overlap of strain-balanced semiconductor superlattices. Design parameters are input at the top of the interface. The lower part of the interface shows a quick "at a glance" look at the calculated results which are stored in matrix format in the MATLAB workspace.

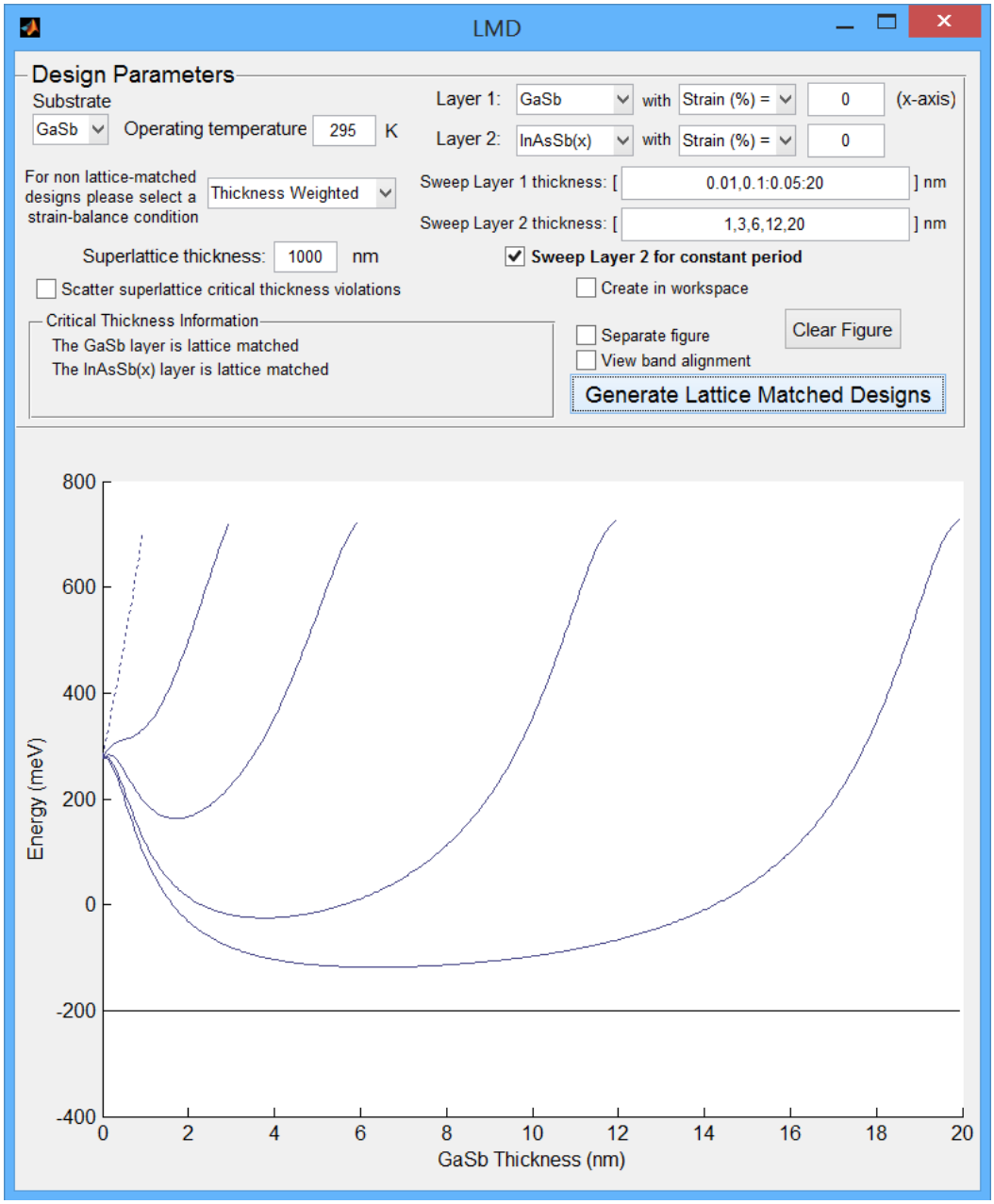


Figure 44. Graphical user interface of the software tool which calculates the ground state transition energy and wavefunction overlap of lattice-balanced semiconductor superlattices. Design parameters are input at the top of the interface. The lower part of the interface shows a quick "at a glance" look at the calculated results which are stored in matrix format in the MATLAB workspace.

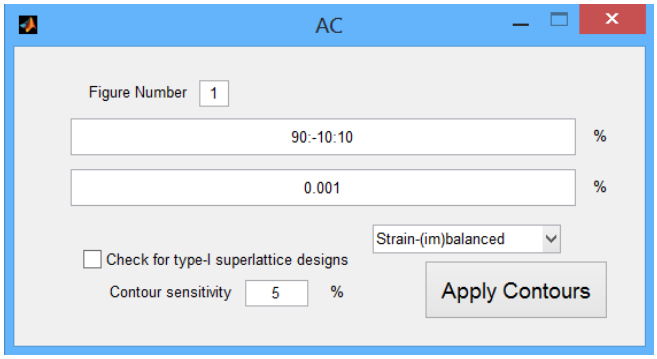


Figure 45. Graphical user interface of the software tool which identifies the subset of superlattice designs which obtain maximum absorption (wavefunction overlap square) as a function of ground state transition energy.

The *Superlattice Optimal Design Tool* utilizes the matrix outputs of the *Lattice-Matched* and *Strain-Balanced Design Tools*, primarily the ground state transition energy and wavefunction overlap square, to determine the optimal superlattice design. The user interface for the *Superlattice Optimal Design Tool* is shown in Figure 45, within which the user inputs a set of target wavefunction overlap square values. The software then locates all transition energies and corresponding design parameters for each target wavefunction overlap square within a user-defined allowable error. These contours of constant wavefunction overlap square are then utilized in plots of the superlattice design space referred to as design space maps for the purpose of visualizing the optimal superlattice design. In the design space maps of strain-balanced material systems, the ground state transition energy is plotted on the vertical axis, alloy composition is plotted on the horizontal axis, and contours of constant period thickness are displayed in the plot. Similar figures are generated for lattice-matched systems, except that the horizontal axis is represented by one of the two constituent layer thicknesses; generally the larger

bandgap material for figure clarity. By overlaying the contours of constant wavefunction overlap square onto the figures, optimal superlattice designs are readily identified as a function of ground state transition energy. In particular, the optimal design for any given transition energy will be located at the minimum of a wavefunction overlap square contour, as this point represents the maximum possible absorption that can be achieved for the targeted optical transition.

All of the superlattice designs discussed in this work possess two free design parameters. For a strain-balanced superlattice composed of two ternary alloys, the second alloy composition can act as a third design parameter. A third degree of design freedom could be used to optimize another characteristic of the superlattice, such as the density of states. No additional design freedom is gained by using ternary alloys in the lattice-matched superlattice; however lattice-matched quaternaries would provide additional design freedom.

## 5.2 Lattice-Matched GaSb/$InAs_{0.911}Sb_{0.089}$ and GaSb/$InAs_{0.932}Bi_{0.068}$

The low and room temperature design space maps of the lattice-matched GaSb/$InAs_{0.911}Sb_{0.089}$ superlattice system are presented Figures 46a (0 K) and 46b (295 K), which plot the ground state transition energy of the superlattice as a function of the GaSb layer thickness for 1, 3, 5, 8, 10, 12, and 15 nm period thicknesses (solid blue curves). The bandgap energies of GaSb and $InAs_{0.911}Sb_{0.089}$ are indicated in the figures (horizontal dash-dot lines); it can be seen that (1) as the GaSb layer thickness approaches zero the ground state transition energy of the superlattice approaches the bandgap energy

of $InAs_{0.911}Sb_{0.089}$ and (2) when the $InAs_{0.911}Sb_{0.089}$ layer thickness approaches zero (the GaSb layer thickness constitutes the full period thickness) the ground state transition energy of the superlattice approaches the bandgap energy of GaSb. For intermediate thickness combinations, transition energies can be obtained anywhere between the bandgap energy of GaSb to zero and even negative (semimetallic) transitions as a result of the type-II band alignment between GaSb and $InAs_{0.911}Sb_{0.089}$.

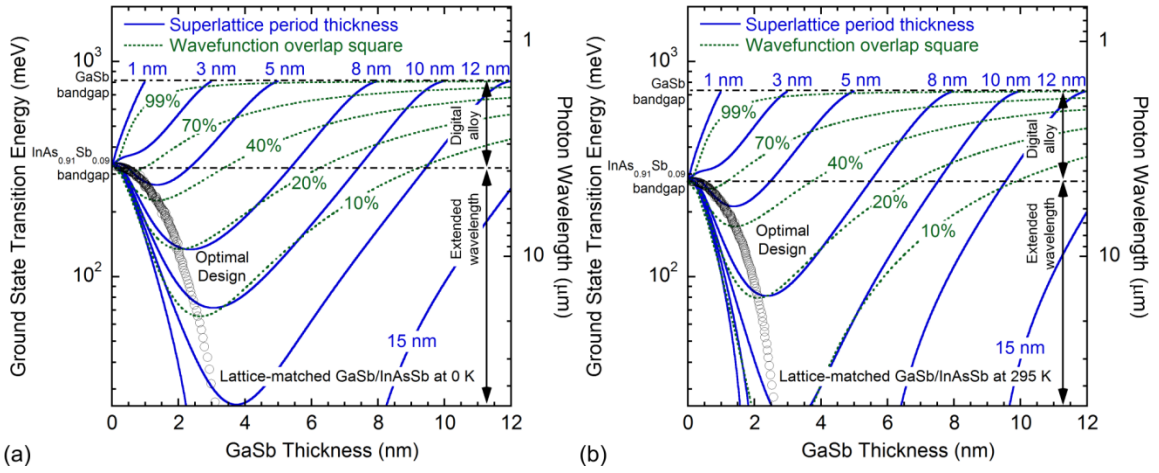


Figure 46. Ground state transition energy of the lattice-matched GaSb/$InAs_{0.911}Sb_{0.089}$ type-II superlattice as a function of the GaSb layer thickness; (a) low temperature and (b) room temperature. The solid blue curves are contours of constant superlattice period thickness. The dotted green curves are contours of constant electron-hole wavefunction overlap squared expressed as a percentage. The minima in the wavefunction overlap square contours represent designs that provide maximum absorption for a given transition energy shown by the open circles.

In order to identify which design will provide maximum absorption for a given transition energy, contours of constant wavefunction overlap square are overlaid onto the figures (dotted green curves). 100% wavefunction overlap occurs at the bandgap energies of GaSb and $InAs_{0.911}Sb_{0.089}$ representing limiting cases that arise when one layer constituent comprises the full period thickness of the superlattice. Between the bandgap energies of GaSb and $InAs_{0.911}Sb_{0.089}$, wavefunction overlap is increasing with decreasing period thickness and 100% wavefunction overlap occurs in the limit that the period thickness approaches zero. This region of the design space is defined as the digital alloy regime because the optimal design for a cutoff in this spectral range is an infinitesimally short period superlattice that is a digital analog [80,81] of the lattice-matched random quaternary alloy $(GaSb)_{1-z}(InAs_{0.911}Sb_{0.089})_z$ that covers the same photon energy range with 100% wavefunction overlap [3].

Perhaps more interesting however are the superlattice designs below the bandgap energy of $InAs_{0.911}Sb_{0.089}$, much of which cannot be accessed using lattice-matched $(GaSb)_{1-z}(InAs_{0.911}Sb_{0.089})_z$. In this region, defined as the extended wavelength regime, longer wavelength transitions become accessible as a result of the type-II band alignment between GaSb and $InAs_{0.911}Sb_{0.089}$, but do so at the expense of wavefunction overlap. For a given transition energy in the extended wavelength regime, the design with maximum wavefunction overlap occurs at the minimum of a wavefunction overlap square contour, as any deviation to the left or right of the wavefunction overlap minimum can only result in less wavefunction overlap for that transition energy. Therefore the set of optimal designs which achieve maximum wavefunction overlap square as a function of transition energy can be identified at the wavefunction overlap square minima (open circles).

Another design option at the GaSb lattice constant is the lattice-matched GaSb/$InAs_{0.932}Bi_{0.068}$ superlattice shown in Figures 47a (0 K) and 47b (295 K). Similar to the GaSb/$InAs_{0.911}Sb_{0.089}$ superlattice, the GaSb/$InAs_{0.932}Bi_{0.068}$ system also forms a type-II broken gap band alignment and as a result the two design spaces bear many similarities. There is a digital alloy regime between the bandgap energies of GaSb and $InAs_{0.932}Bi_{0.068}$, an extended wavelength regime for energies below the bandgap of $InAs_{0.932}Bi_{0.068}$, and a non-trivial optimal design in the extended wavelength regime. The key difference between the two superlattice systems is that a greater spectral range falls into the high wavefunction overlap digital alloy regime in the GaSb/$InAs_{0.932}Bi_{0.068}$ superlattice due to the significantly smaller bandgap energy of $InAs_{0.932}Bi_{0.068}$.

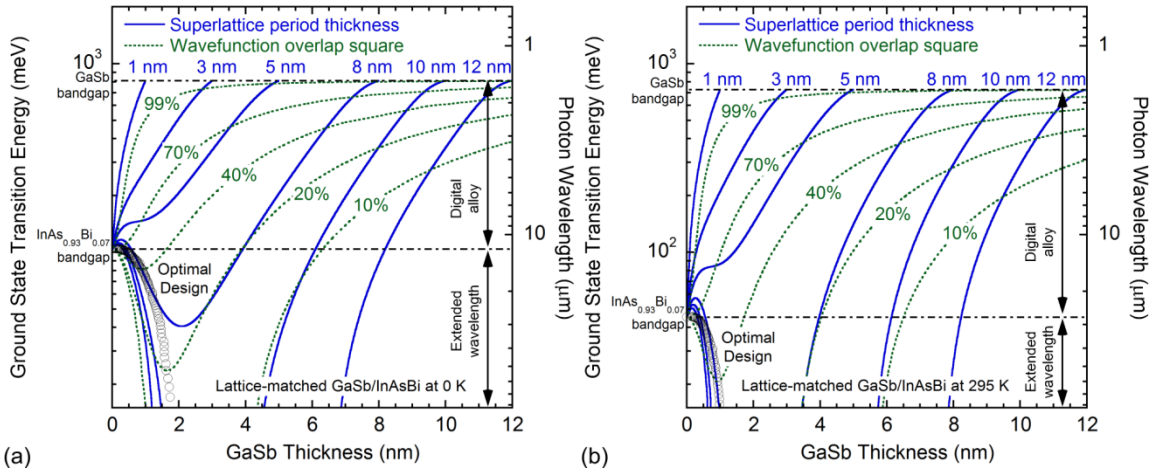


Figure 47. Ground state transition energy of the lattice-matched GaSb/$InAs_{0.932}Bi_{0.068}$ type-II superlattice as a function of the GaSb layer thickness; (a) low temperature and (b) room temperature. The solid blue curves are contours of constant superlattice period thickness. The dotted green curves are contours of constant electron-hole wavefunction overlap squared expressed as a percentage. The minima in the wavefunction overlap square contours represent designs that provide maximum absorption for a given transition energy shown by the open circles.

## 5.3 Strain-Balanced InAs/InAsSb, InAs/GaInSb, and InAs/InAsBi

In addition to lattice-matched designs, a variety of strain-balanced superlattice systems can be grown at the GaSb lattice constant including InAs/InAsSb, InAs/GaInSb, and InAs/InAsBi. In each of these three material systems, the InAs layers are under tensile strain which is compensated by compressively strained InAsSb, GaInSb, or InAsBi layers. Strain is balanced using the thickness-weighted technique in which the magnitudes of the strain-thickness products of the tensile and compressive layers are made equal [18]. Equation 21 shows the thickness weighted strain-balance expression for an InAs/InAsSb superlattice with layer thicknesses $d_{InAs}$ and $d_{InAsSb}$ and strains $\varepsilon_{InAs}$ and $\varepsilon_{InAsSb}$.

$$\varepsilon_{InAs} \times d_{InAs} + \varepsilon_{InAsSb} \times d_{InAsSb} = 0 \tag{21}$$

The design space map of the strain-balanced InAs/InAsSb superlattice system is presented in Figures 48a (0 K) and 48b (295 K), which plot the ground state transition energy of the superlattice as a function of the InAsSb layer composition for 0 (infinitesimal), 4, 7, 9, 12, and 20 nm period thicknesses (solid blue curves). Also shown with a solid blue curve is a critical thickness limit [8] which provides a suggested maximum period thickness that can be utilized before the individual InAs or InAsSb layers themselves could begin to relax. Wavefunction overlap square contours are represented with dotted green curves which show that a digital alloy regime is formed between the bandgap energies of tensilely strained InAs on GaSb and lattice-matched InAsSb, within which the optimal design follows the infinitesimal (0 nm) period thickness design contour. Additionally, an extended wavelength regime is formed below

the bandgap energy of lattice-matched InAsSb within which the optimal design follows the minima of the wavefunction overlap square contours (open circles).

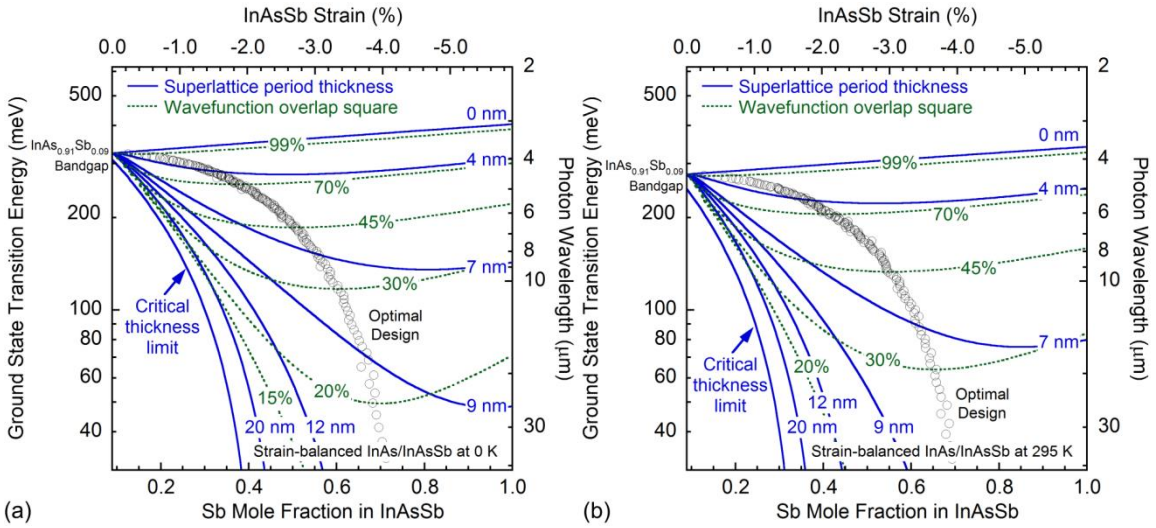


Figure 48. Ground state transition energy of the strain-balanced InAs/InAsSb type-II superlattice as a function of the InAsSb layer mole fraction on the lower horizontal axis and strain on the upper horizontal axis; (a) low temperature and (b) room temperature. The solid blue curves are contours of constant superlattice period thickness and the critical thickness limit indicates the maximum period thickness that can be grown before the constituent InAs or InAsSb layers could begin to relax. The dotted green curves are contours of constant electron-hole wavefunction overlap squared expressed as a percentage. The minima in the wavefunction overlap square contours represent designs which provide maximum absorption for a given transition energy shown by the open circles.

Like the digital alloy regimes of the lattice-matched designs discussed in Section 5.2, the digital alloy regimes of the strain-balanced superlattice designs are bounded by the bandgap energies of the superlattice constituents; this particular characteristic of the design is a direct result of the strain-balance condition [18] given in Equation 21. For example, the lower energy limit of the InAs/InAsSb digital alloy regime coincides with the bandgap energy of $InAs_{0.911}Sb_{0.089}$. From the point of view of strain-balance, reducing the Sb mole fraction (InAsSb strain) produces a corresponding decrease in the ratio of the InAs to InAsSb layer thickness $d_{InAs}/d_{InAsSb}$. In the limit that the InAsSb layer strain approaches zero, the InAs layer thickness is zero and the InAsSb layer (lattice-matched $InAs_{0.911}Sb_{0.089}$) constitutes the full period thickness of the design. The structure of the superlattice becomes independent of period thickness as it converges to bulk lattice-matched $InAs_{0.911}Sb_{0.089}$, and the superlattice effective bandgap converges to the bandgap energy of bulk $InAs_{0.911}Sb_{0.089}$; note the convergence of all period thickness contours at the lattice-matched Sb mole fraction of 8.9%.

Similarly, the upper energy limit of the digital alloy regime approaches the heavy hole bandgap energy of tensilely strained InAs. In this case, increasing the Sb mole fraction (InAsSb strain) produces a corresponding decrease in the ratio of the InAsSb to InAs layer thickness $d_{InAsSb}/d_{InAs}$. If the InAsSb layer strain could be made to be arbitrarily large, then the InAsSb layer thickness would approach zero and the superlattice would converge to bulk, tensilely strained InAs on GaSb for all period thicknesses. In practice, the InAsSb layer strain is limited to -5.91% for a unity Sb mole fraction. As the InAs layer strain is 0.61%, the ratio $d_{InAsSb}/d_{InAs}$ can be no smaller

than 0.1 and as a result, the superlattice converges to bulk, tensilely strained InAs on GaSb only for very short period thicknesses.

The next design space considered is that of the strain-balanced InAs/GaInSb superlattice seen in Figures 49a (0 K) and 49b (295 K). The ground state transition energy of the superlattice is plotted as a function of the GaInSb layer composition for 0 (infinitesimal), 5, 7, 9, and 10 nm period thicknesses (solid blue curves). Critical thickness limited designs produce negative transition energies not seen in Figure 49 due to the type-II broken gap band alignment between InAs and GaInSb. The digital alloy regime is formed between the GaSb and tensilely strained InAs heavy hole bandgap energies between which the optimal design follows the infinitesimal (0 nm) period thickness design contour. The optimal design in the extended wavelength regime originates at the bandgap energy of tensilely strained InAs and extends to zero and negative (semimetallic) transition energies.

Two important characteristics of the strain-balanced type-II superlattice are observed in Figures 48 and 49; that (1) the digital alloy regimes are bounded by the bandgap energies of the fixed strain binary layers (tensile InAs) and the lattice-matched compositions of the variable strain alloy layers ($Ga_{1.0}In_{0.0}Sb$ and $InAs_{0.911}Sb_{0.089}$) and (2) the extended wavelength regime originates at the lower energy end of the digital alloy regime with 100% wavefunction overlap. This suggests that improved wavefunction overlap could be obtained in the extended wavelength regime if a material with a smaller lattice-matched bandgap energy were used in place of InAsSb or GaInSb.

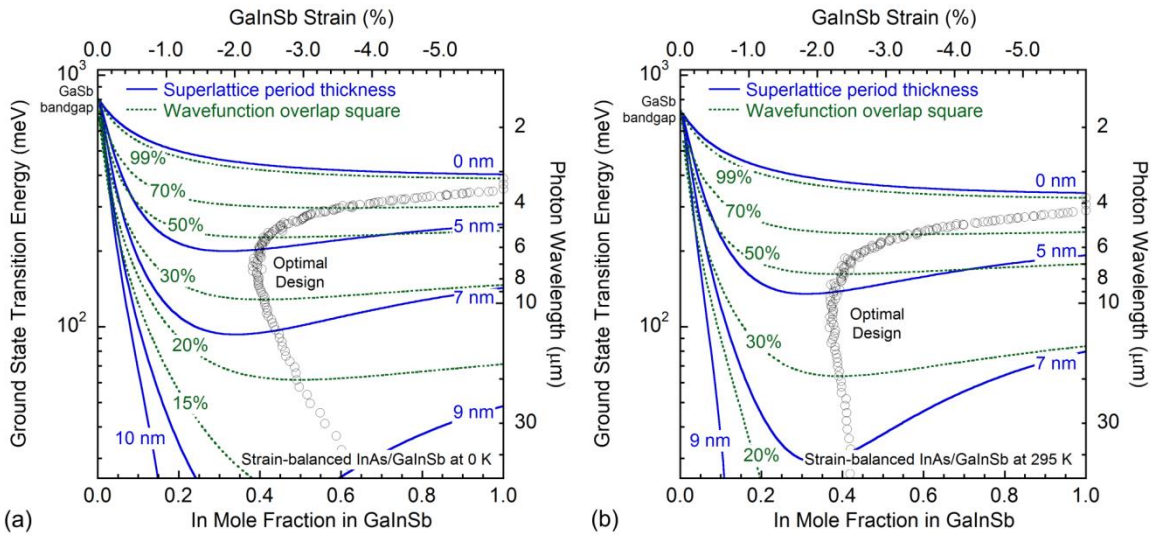


Figure 49. Ground state transition energy of the strain-balanced InAs/GaInSb type-II superlattice as a function of the GaInSb layer mole fraction on the lower horizontal axis and strain on the upper horizontal axis; (a) low temperature and (b) room temperature. The solid blue curves are contours of constant superlattice period thickness. The dotted green curves are contours of constant electron-hole wavefunction overlap squared expressed as a percentage. The minima in the wavefunction overlap square contours represent designs that provide maximum absorption for a given transition energy shown by the open circles.

Referring back to Figures 1 and 12, it can be seen that InAsBi possesses several appealing features for superlattice applications. InAsBi layers are compressively strained on GaSb for Bi mole fractions > 0.068, its bandgap decreases at a greater rate than either GaInSb or InAsSb, and it forms a type I band alignment with InAs (see Figure 12 inset). Furthermore, the InAs/InAsBi superlattice is defined solely by the presence of Bi in the InAsBi layers and the absence of Bi in the InAs layers, as the group-III sublattice is composed exclusively of In atoms throughout the superlattice. As a result, the InAs/InAsBi superlattice possesses a relatively simple interface configuration and may

therefore be expected to exhibit long minority carrier lifetimes just as in the InAs/InAsSb superlattice [15]. The design space map of the strain-balanced InAs/InAsBi superlattice system is presented in Figures 50a (0 K) and 50b (295 K).

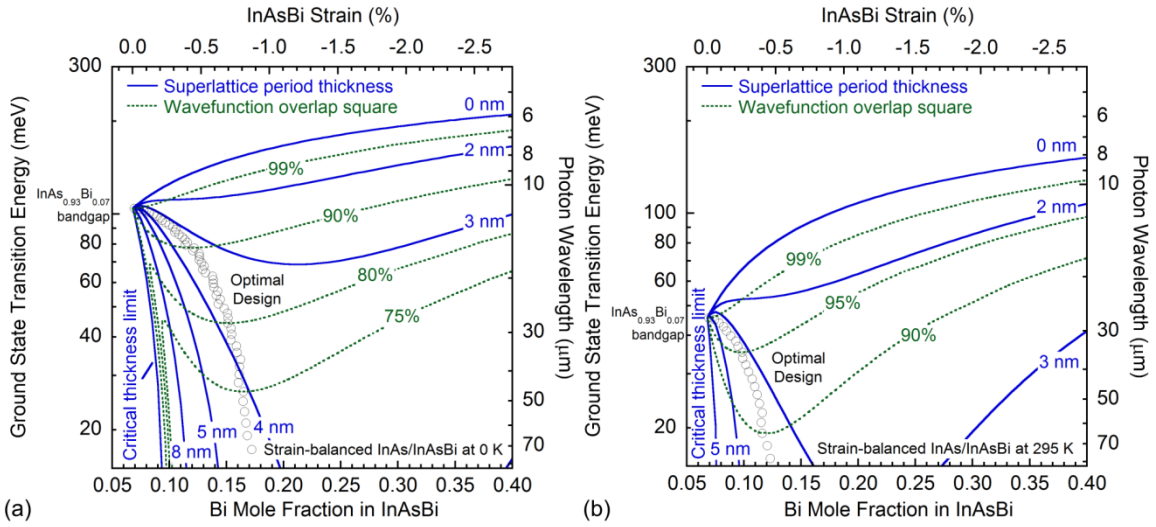


Figure 50. Ground state transition energy of the strain-balanced InAs/InAsBi type-I superlattice as a function of the InAsBi layer mole fraction on the lower horizontal axis and strain on the upper horizontal axis; (a) low temperature and (b) room temperature. The solid blue curves are contours of constant superlattice period thickness and the critical thickness limit indicates the maximum period thickness that can be grown before the constituent InAs or InAsBi layers could begin to relax. The dotted green curves are contours of constant electron-hole wavefunction overlap squared expressed as a percentage. The minima in the wavefunction overlap square contours represent designs that provide maximum absorption for a given transition energy shown by the open circles.

## 5.4 Temperature Dependence of the Optimal Designs

In this section, the low and room temperature optimal designs are compared so as to determine whether or not it is necessary to calculate the optimal design parameters as a function of temperature. In Figure 51, wavefunction overlap square is plotted as a function of ground state transition energy in the extended wavelength regime of the optimal InAs/InAsSb superlattice. The solid blue curve represents the low temperature optimal design from Figure 48a and the solid red curve represents the room temperature optimal design from Figure 48b. Next, the transition energies and wavefunction overlap square of the low temperature optimal design are calculated at an operating temperature 295 K, resulting in the dashed blue curve which closely follows the room temperature optimal design (red curve) with virtually no loss in wavefunction overlap.

These results indicate that the optimized InAs/InAsSb superlattice design parameters are not a strong function of temperature; the same conclusion is drawn from the temperature dependent analysis of the optimal InAs/GaInSb, InAs/InAsBi, GaSb/$InAs_{0.911}Sb_{0.089}$, and GaSb/$InAs_{0.932}Bi_{0.068}$ superlattice systems. This characteristic of the superlattice can be understood by considering how temperature modifies the bulk band structure of the superlattice constituents. When the temperature is changed, the conduction bands of the two superlattice constituents generally shift in the same direction and often by roughly the same amount. As a result, the repeating potential in the conduction band is virtually unchanged; the electron minibands shift with the bulk band structure while the wavefunctions are essentially unaltered. The same is true of the hole minibands formed in the valence band, and thus what is ultimately observed is that the

ground state transition energy primarily shifts with the bulk band structure while wavefunction overlap is unchanged. Therefore it is only necessary to calculate the design space map of a superlattice at a single temperature in order to determine the optimal layer thicknesses and mole fractions as a function of wavefunction overlap. The ground state transition energy of the optimal design is the only parameter that is a strong function of temperature.

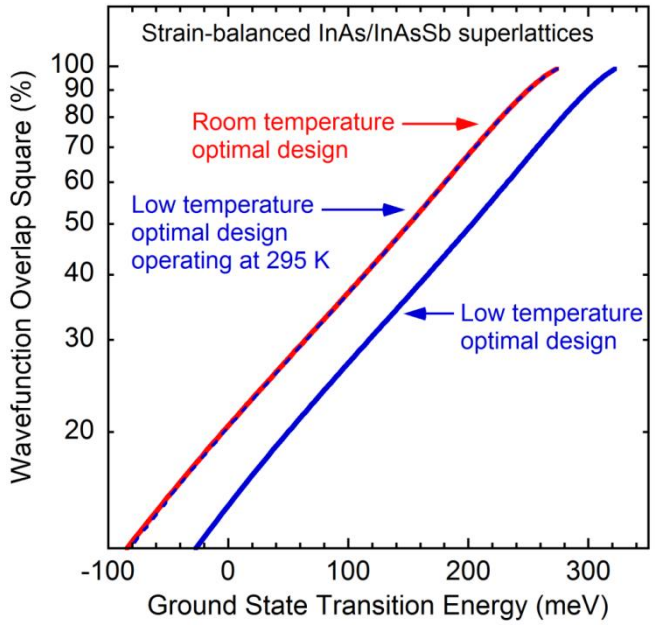


Figure 51. Wavefunction overlap square plotted as a function of the ground state transition energy of the strain-balanced InAs/InAsSb superlattice. Solid curves represent designs optimized at low temperature (blue) and at room temperature (red). The dashed blue curve represents the low temperature optimal design operating at 295 K.

## 5.5 Superlattice Absorption Coefficient

The ground state absorption coefficient of each superlattice ($\alpha_{SL}$) is computed as a function of wavefunction overlap square $\left|\Psi_h^*\Psi_e\right|^2$ using Equation 22 derived from Figure 41. The proportionality constant $\alpha_1$ in Equation 22 is the ground state absorption coefficient realized in the superlattice when the wavefunction overlap is unity. This constant can be determined experimentally from absorption coefficient measurements, and for example is 4990 $cm^{-1}$ for the strain-balanced InAs/InAsSb superlattice system (see Section 4.5). In the InAs/InAsSb superlattice design space (see extended wavelength regime of Figure 48), the 100% wavefunction overlap superlattice design converges to bulk $InAs_{0.911}Sb_{0.089}$ in the limit that the InAs layer thickness approaches zero and the Sb mole fraction approaches the lattice-matched condition with unstrained InAsSb constituting the full period thickness.

$$\alpha_{SL} = \alpha_1 \times \left|\Psi_h^*\Psi_e\right|^2 \tag{22}$$

For bulk material, there is only one analytical point in the optical joint density of states at which the bandgap absorption coefficient $\alpha_g$ is well defined. For a superlattice there are two critical points; one at the lowest energy and one at the highest energy transition formed between the ground state electron and hole minibands [72]. The lowest energy transition defines the effective bandgap of the superlattice that is marked by a steep rate of increase in the optical joint density of states and the absorption coefficient, whereas at the highest energy transition the superlattice density of states is constant in photon energy and the absorption coefficient plateaus at $\alpha_{SL}$ until the onset of the next set of miniband transitions. The maximum of the first derivative of the absorption

coefficient identifies the point at which the optical joint density of states increases at the greatest rate and hence provides measure of the superlattice effective bandgap. However, the steep rate of increase in the superlattice absorption coefficient at this point makes it difficult to accurately determine the magnitude of superlattice absorption coefficient at the effective bandgap. On the other hand, since the optical joint density of states and the absorption coefficient plateau at $\alpha_{SL}$, it can be reliably and reproducibly determined. There is no bulk analog for $\alpha_{SL}$ as it is unique to the superlattice optical joint density of states.

The room temperature absorption coefficient of bulk $InAs_{0.911}Sb_{0.089}$ has been measured as a function of photon energy using spectroscopic ellipsometry in Section 4.1, and the absorption coefficient first derivative maximum identifies the bandgap absorption coefficient $\alpha_g$ as 2240 $cm^{-1}$. The structure of the strain-balanced InAs/InAsSb superlattice is convergent on bulk $InAs_{0.911}Sb_{0.089}$ in the limit that wavefunction overlap approaches 100%, at which point the absorption coefficient $\alpha_{SL} = \alpha_1 = 4990$ $cm^{-1}$. The bandgap absorption coefficient $\alpha_g$ is smaller than $\alpha_1$ as it is measured at a lower density of states. For comparison, the absorption coefficient of $InAs_{0.911}Sb_{0.089}$ reaches 4990 $cm^{-1}$ ($\alpha_1$) when the photon energy is 30 meV greater than the bandgap, which is consistent with the width of the ground state electron miniband in the typical strain-balanced InAs/InAsSb superlattice.

Equation 22 can be utilized to determine the absorption coefficient of a given superlattice design from the calculated wavefunction overlap, provided the unity wavefunction overlap absorption coefficient $\alpha_1$ is known; to date $\alpha_1$ has been measured

for strain-balanced InAs/InAsSb superlattices [19]. Comparison of the measured bandgap absorption coefficient of bulk $InAs_{0.911}Sb_{0.089}$ $\alpha_g$ = 2240 $cm^{-1}$ and $\alpha_1$ indicates that $\alpha_1 = C_{SL} \times \alpha_g$ with the constant of proportionality $C_{SL}$ = 2.228. Provided this relationship is true in other material systems, the unity wavefunction overlap absorption coefficient $\alpha_1$ in Equation 22 can be replaced with the product of $C_{SL}$ and $\alpha_g$ as shown in Equation 23. The significance of this relationship is the bulk bandgap absorption coefficient $\alpha_g$ is simpler to determine than $\alpha_1$.

$$\alpha_{SL} = (C_{SL} \times \alpha_g) \times \left|\Psi_h^* \Psi_e\right|^2 \tag{23}$$

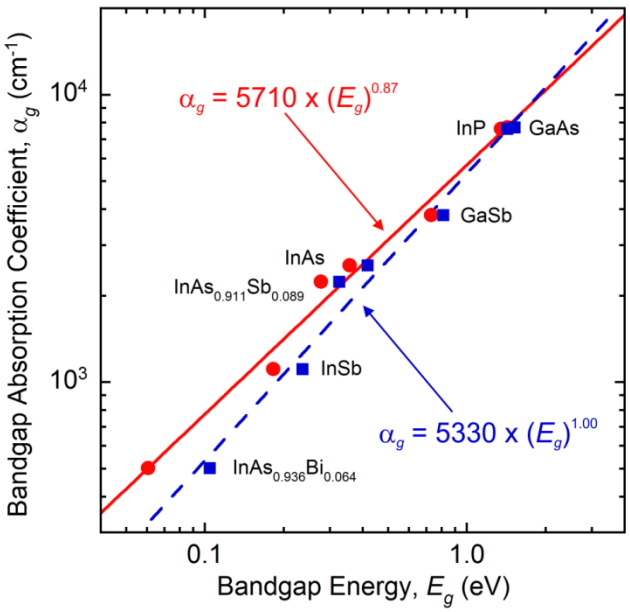


Figure 52. Bandgap absorption coefficient of various bulk III-V semiconductors as a function of bandgap energy at low temperature (blue squares) and at room temperature (red circles). For all materials the bandgap energy shifts left to lower energies as the temperature increases. The dashed and solid lines are power law fits to the low and room temperature data, with the best fit values shown.

Table 16. Bandgap energy $E_g$ and bandgap absorption coefficient $\alpha_g$ of bulk III-V binary and ternary alloys determined using spectroscopic ellipsometry.

| Material | $E_g$ at 295 K (eV) | $E_g$ at 0 K (eV) | $\alpha_g$ ($cm^{-1}$) |
|---|---|---|---|
| GaAs | 1.425 | 1.519 | 7700 |
| InP | 1.348 | 1.424 | 7615 |
| GaSb | 0.730 | 0.812 | 3820 |
| InAs | 0.357 | 0.417 | 2550 |
| InSb | 0.182 | 0.235 | 1112 |
| $InAs_{0.911}Sb_{0.089}$ | 0.277 | 0.325 | 2240 |
| $InAs_{0.936}Bi_{0.064}$ | 0.060 | 0.104 | 503 |

The bandgap absorption coefficient $\alpha_g$ is plotted in Figure 52 as a function of the low temperature (blue squares) and room temperature (red circles) bandgap energy for bulk GaAs, InP, GaSb, InAs, $InAs_{0.911}Sb_{0.089}$, InSb, and $InAs_{0.936}Bi_{0.064}$. The dashed and solid lines are power law equations fit to the respective low and room temperature results, with power law 1.00 observed at low temperature and power law 0.87 at room temperature. The bandgap energies and bandgap absorption coefficients are summarized in Table 16. In these materials, the functional form and magnitude of the optical joint density of states is insensitive to temperature, while the accompanying bandgap energy is strongly temperature dependent.

The bandgap absorption coefficient $\alpha_g$ and room temperature bandgap energy are obtained from spectroscopic ellipsometry measurements and analysis of each material's absorption coefficient as a function of energy. In the analyses, the bandgap absorption coefficient and energy are determined at the absorption coefficient first derivative maximum. The low temperature bandgap energies are obtained from the literature for the binary materials [3], and from this work (Sections 4.1 and 3.1) for $InAs_{0.911}Sb_{0.089}$ and $InAs_{0.932}Bi_{0.064}$.

These results show that the bandgap absorption coefficient significantly decreases with bandgap energy, which is primarily due to a strong reduction in the optical joint density of states in small bandgap bulk III-V material. In contrast, superlattices maintain a relatively constant optical joint density of states within a set of miniband transitions, and the reduction observed in the superlattice absorption coefficient with effective bandgap energy is mainly due to a reduction in the wavefunction overlap square [19].

## 5.6 Comparing Absorption and Practical Design Considerations

The absorption coefficients of the superlattice systems from Sections 5.2 and 5.3 are calculated as a function of wavefunction overlap square using Equation 23, the constant of proportionality $C_{\mathrm{SL}} = 2.228$, and the bandgap absorption coefficients $\alpha_g$ listed in Table 16. The 100% wavefunction overlap designs of the lattice-matched $GaSb/InAs_{0.911}Sb_{0.089}$ and strain-balanced InAs/InAsSb superlattices both converge to bulk $InAs_{0.911}Sb_{0.089}$ (see Figures 46 and 48) and thus the measured value of $\alpha_1 = C_{\mathrm{SL}} \times$

$\alpha_g$ = 4990 cm$^{-1}$ for InAs/InAsSb superlattices is used. For lattice-matched GaSb/InAs$_{0.936}$Bi$_{0.068}$ and strain-balanced InAs/InAsBi superlattices the bandgap absorption coefficient for bulk InAs$_{0.936}$Bi$_{0.064}$ is used with $\alpha_1 = C_{\mathrm{SL}} \times \alpha_g$ = 1120 cm$^{-1}$. Likewise for strain-balanced InAs/GaInSb superlattices the bandgap absorption coefficient for bulk InAs is utilized with $\alpha_1 = C_{\mathrm{SL}} \times \alpha_g$ = 5680 cm$^{-1}$. In the digital alloy regimes the absorption coefficients are calculated by interpolating $\alpha_1$ as a function of energy between the two endpoint materials of the digital alloy, and scaling the resultant absorption coefficient by the wavefunction overlap square.

The absorption coefficients of the strongest possible absorbing superlattice designs in the extended wavelength regime are provided in Figure 53 as a function of the low temperature ground state transition energy (lower horizontal axis) and the corresponding wavelength cutoff (upper horizontal axis). The overall optimal designs are shown in Figure 53a and the practical designs limited by achievable material strain and thicknesses are shown in Figure 53b. The three strain-balanced systems (InAs/InAsSb, InAs/GaInSb, and InAs/InAsBi) are shown with solid curves and the two lattice-matched systems (GaSb/InAs$_{0.911}$Sb$_{0.089}$ and GaSb/InAs$_{0.936}$Bi$_{0.068}$) are shown with dotted curves. To compare the absorption strength of the optimal superlattice designs with that of bulk material, the power law fit for low temperature bulk material shown in Figure 52 is scaled by the proportionality constant $C_{\mathrm{SL}}$ and displayed by the dashed line; the resulting equation is 2.228 × 5.330 cm$^{-1}$/meV × $E_g$, where $E_g$ is the ground state transition energy in units of meV.

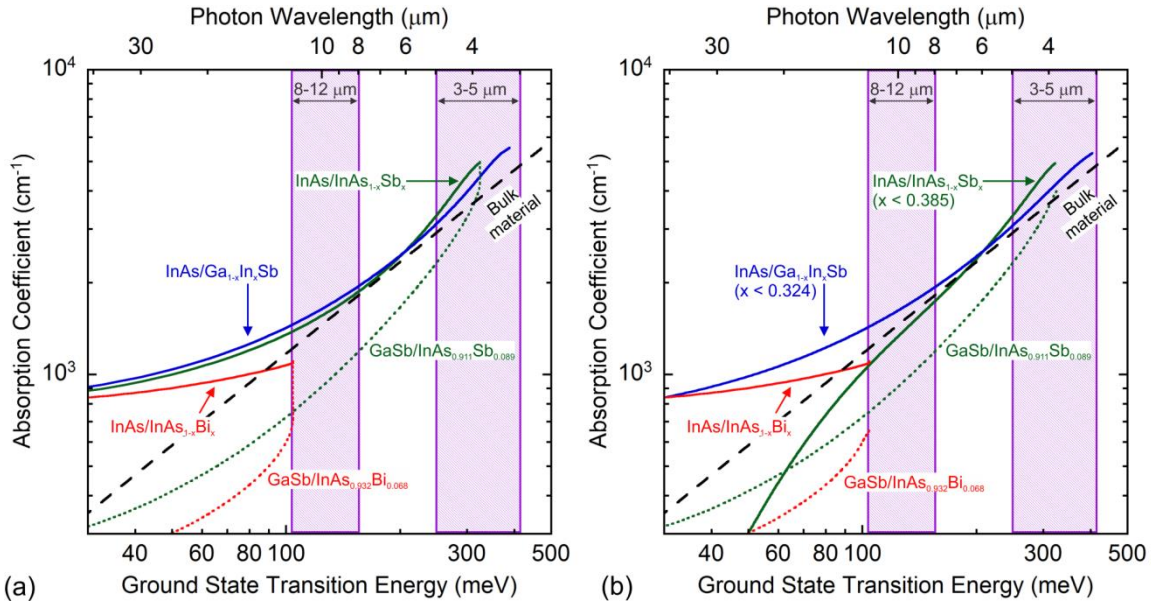


Figure 53. Absorption coefficient of optimized superlattice designs as a function of ground state transition energy on the lower horizontal axis and photon wavelength on the upper horizontal axis; (a) optimal designs and (b) strain- and thickness-limited practical designs. Strain-balanced designs are shown by solid curves, lattice-matched designs are shown by dotted curves, and bulk material is shown by a dashed line. The technologically relevant 3 to 5 and 8 to 12 μm wavelength ranges are indicated by purple shaded bands.

For the InAsSb- and InAsBi-based superlattices, the strain-balanced systems provide stronger absorption as a function of transition energy than their lattice-matched counterparts. Physically, this occurs because the strain-balanced systems utilize the ternary layer mole fraction as a free design parameter which allows more favorable band alignments to be established. For all five superlattice systems, the absorption coefficient decreases as the wavefunction overlap becomes weaker with increasing wavelength cutoff, and the rate at which the absorption coefficient decreases is lowest for the strain-balanced InAs/InAsBi superlattice due to its type-I band alignment. In fact for very long

wavelengths (> 12 μm), the rate at which the strain-balanced superlattice absorption coefficients decrease with photon energy due to decreasing wavefunction overlap (solid curves) is significantly less than the rate at which the bulk absorption coefficient decreases (dashed line), indicating that superlattice-based designs may be preferable to bulk material in terms of absorption strength for longer wavelength applications.

While the optimal designs discussed thus far are useful as a design guide, the practical design must abide by additional constraints inherent to epitaxial growth. For example, the magnitude of the strain on the constituent layers becomes a practical design concern as the optical quality degrades rapidly when the material is heavily strained, even if the layer is pseudomorphic. Figure 53b shows the practical design curves in which the magnitude of the ternary layer strain in the strain-balanced superlattice systems is limited to 2.0%, which limits the Sb mole fraction to 0.385 in InAsSb and the In mole fraction to 0.324 in GaInSb. With this added constraint, the strain-balanced InAs/InAsSb superlattice is most impacted; however it still outperforms its lattice-matched counterpart GaSb/$InAs_{0.911}Sb_{0.089}$. On the other hand, the strain-balanced InAs/GaInSb superlattice is less impacted because the wavefunction overlap square contours in this system are relatively flat in the vicinity of the optimal design (see Figure 49) resulting in an optimal design that is relatively insensitive to In-content. Nevertheless, the strain-balanced InAs/InAsSb superlattice possesses a significantly longer minority carrier lifetime compared to the strain-balanced InAs/GaInSb superlattice [15]. Absorption in the strain-balanced InAs/InAsBi superlattice is not impacted by the strain limit as the InAsBi layer strain in the optimal design never exceeds -1% (see Figure 50 upper horizontal axis).

While none of the optimal designs investigated exceed the critical thickness limit which would effectively limit the maximum layer thicknesses that could be utilized, several designs do converge upon the infinitesimal (0 nm) period thickness limit. In addition to the strain limit, the practical design also enforces a minimum layer thickness of 0.50 nm as a practical limit of how thin these layers could be grown. This constraint mainly appears in the digital alloy regimes of the superlattice designs investigated, however it also limits the utility of the two lattice-matched systems which require GaSb thicknesses $< 0.50$ nm to reach near-unity wavefunction overlap. The optimal and practical design parameters for the lattice-matched GaSb/$InAs_{0.911}Sb_{0.089}$ and GaSb/$InAs_{0.932}Bi_{0.068}$ superlattices and strain-balanced InAs/InAsSb, InAs/GaInSb, and InAs/InAsBi superlattice systems are presented for several key wavelengths in Appendix B.

## 5.7 Verification of the InAs/InAsSb Mid-Wave Optimal Design

The optimal design criteria in Appendix B are utilized in the design and growth of one optimized mid-wave infrared strain-balanced InAs/InAsSb superlattice. The sample is composed of alternating InAs (2.16 nm) and $InAs_{0.802}Sb_{0.198}$ (1.51 nm) layers with a total thickness of 1 μm sandwiched between 10 nm thick AlSb confinement layers with a 10 nm thick GaSb cap. The sample is grown at 425 °C on a (100)-oriented GaSb substrate by molecular beam epitaxy using a 0.5 monolayer per second InAs growth rate and a constant 1.20 As/In flux ratio. The structural properties of the superlattice are measured using X-ray diffraction. The unintentional Sb in the InAs layers of the

superlattice was not quantifiable due to the short period thickness of this sample, therefore an unintentional Sb mole fraction of 0.024 is assumed based on the unintentional Sb measured in other InAs/InAsSb superlattices grown under the similar conditions in Table 12. The sample cross section is shown in the inset of Figure 54.

The *Superlattice Miniband Structure Tool* is used to calculate the ground state transition energy of the superlattice at 305.9 meV (4.1 μm wavelength) at low temperature and 258.1 meV (4.8 μm wavelength) at room temperature, and the square of the electron-hole wavefunction overlap at the ground state is 94.3%. Spectroscopic ellipsometry is used to measure the room temperature absorption coefficient of the superlattice shown in Figure 54. The ground state transition energy (effective bandgap) of the superlattice is identified at the absorption coefficient first derivative maximum at 257 meV (within 0.5% of the calculated value of 258.1 meV), at which point the absorption coefficient increases rapidly to $\alpha_{SL} = 4750$ cm$^{-1}$.

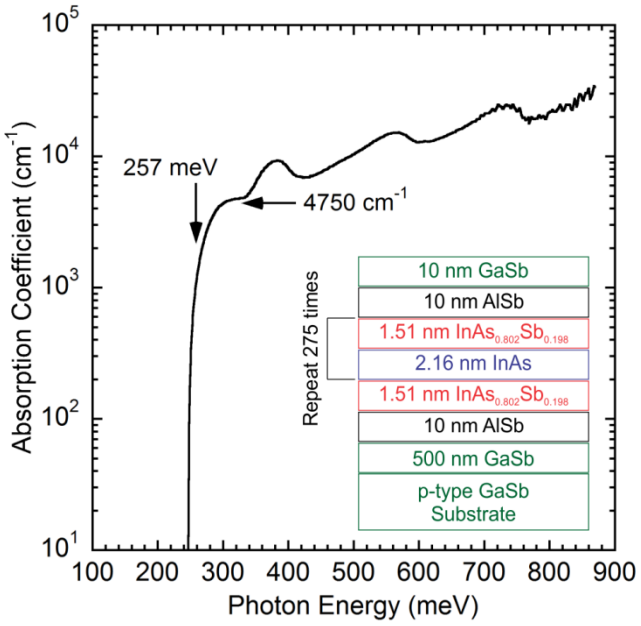


Figure 54. Absorption coefficient of a strain-balanced InAs/InAsSb superlattice optimized for maximum absorption at its ground state transition energy of 257 meV (4.8 μm wavelength). Inset shows the sample cross section.

Figure 55 shows the absorption coefficient of strain-balanced InAs/InAsSb superlattices as a function of the wavefunction overlap squared. The data represented by open black circles and the power law fit given by the solid line is the same data that was presented in Figure 41. The solid blue circle shows the absorption coefficient of the optimized practical design in Figure 54 at 94.3% wavefunction overlap square which agrees with the fitted line to within 1%.

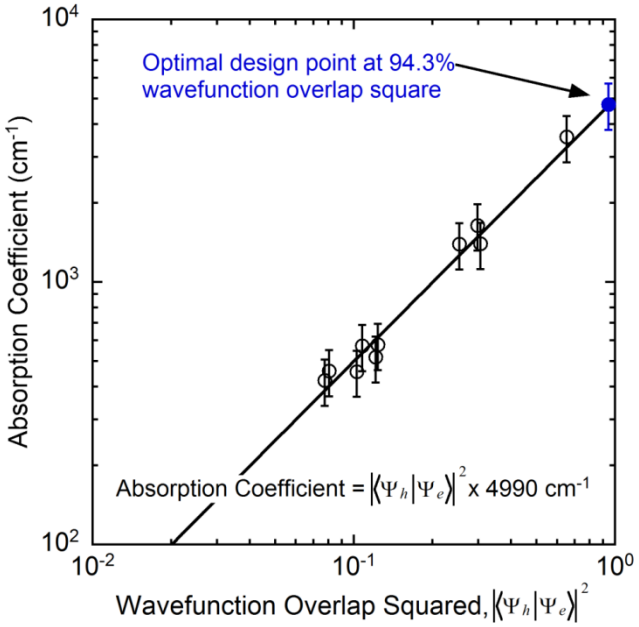


Figure 55. Ground state absorption coefficient as a function of the square of the electron-hole wavefunction overlap integral in strain-balanced InAs/InAsSb superlattices. The solid line shows the unity power law fit to the data from Figure 41 and Table 12 (open black circles). The solid blue circle shows the optimized 4.8 μm wavelength optimized design with 94.3% wavefunction overlap square.

A Nicolet Instrument Corporation Magna-IR 760 Fourier transform infrared spectrometer is used to measure room temperature photoluminescence from the 1.0 μm thick optimal superlattice grown at 425 °C as well as the 0.5 μm thick bulk lattice-matched $InAs_{0.911}Sb_{0.089}$ sample grown at 430 °C [4] from Section 4.1 of this work. The samples are excited using an 808 nm pump laser and 200 mW of laser power. The pump power density reaching the active region of each sample is 265 W·cm$^{-2}$ which corresponds to an excitation density of $1\times10^{25}$ cm$^{-3}$·s$^{-1}$ in the superlattice and $2\times10^{25}$ cm$^{-3}$·s$^{-1}$ in the bulk $InAs_{0.911}Sb_{0.089}$ sample. The raw photoluminescence from the superlattice (dotted blue curve) and the bulk $InAs_{0.911}Sb_{0.089}$ layer (dotted green curve) are

plotted as a function of photon energy (lower horizontal axis) and photon wavelength (upper horizontal axis) in Figure 56. The raw photoluminescence spectra exhibit an absorption feature near 290 meV due to the presence of $CO_2$ in the air which is removed in the solid blue and green curves by correcting the spectra for the optical throughput of the system.

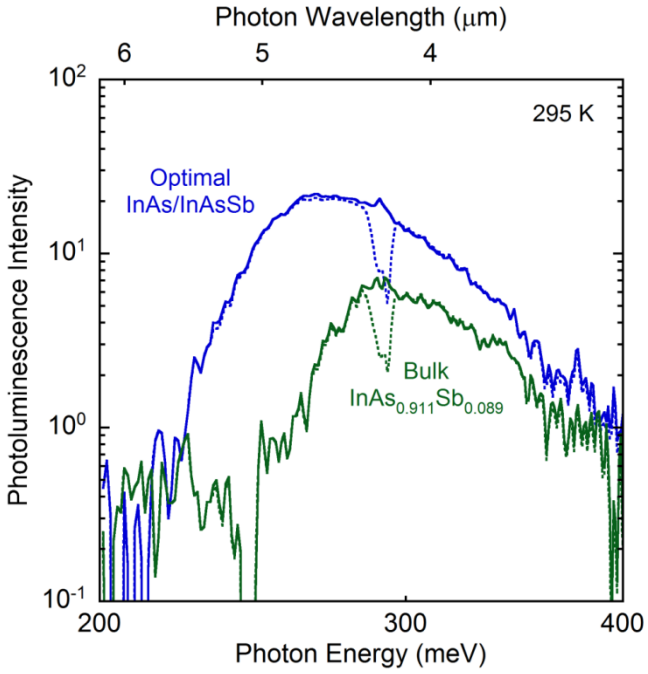


Figure 56. Room temperature photoluminescence from bulk lattice-matched $InAs_{0.911}Sb_{0.089}$ (green curves) and an InAs/InAsSb superlattice designed to provide optimal wavefunction overlap square at 4.8 μm wavelength (blue curves). Dotted curves show the raw photoluminescence spectra while solid curves show the spectra after correcting for the optical throughput of the system.

The photoluminescence first derivative maximum is used to identify the room temperature bandgap energy of the bulk $InAs_{0.911}Sb_{0.089}$ sample at 275 meV, which closely agrees with the room temperature bandgap energy of 277 meV measured using spectroscopic ellipsometry from Section 4.1. Using the same analysis on the superlattice, the photoluminescence first derivative maximum identifies an effective bandgap of 249 meV, which likewise agrees with the 257 meV bandgap measured using spectroscopic ellipsometry in Figure 54. By integrating the photoluminescence spectra as a function of photon energy, a relative measure of the total optical output and general optical quality is obtained. The total integrated intensity of 1664 from the optimized superlattice is more than a factor of three greater than the integrated intensity of 507 from the bulk $InAs_{0.911}Sb_{0.089}$ sample which emits at a shorter wavelength. The superior optical quality of the superlattice is attributed to the high wavefunction overlap of the optimized design and the long minority carrier lifetimes inherent to this material system [15].

## 5.8 Chapter 5 Summary

A software tool is developed that calculates the miniband structure of semiconductor superlattices using a Kronig-Penney model, and identifies the optimal strain-balanced and lattice-matched designs that maximize wavefunction overlap as a function of the ground state transition energy. The functionality of the software is demonstrated on lattice-matched $GaSb/InAs_{0.911}Sb_{0.089}$ and $GaSb/InAs_{0.932}Bi_{0.068}$ superlattices and on strain-balanced InAs/GaInSb, InAs/InAsSb, and InAs/InAsBi

superlattices on GaSb substrates, and the absorption coefficients of the optimized superlattice designs are determined as a function of transition energy. The optimized strain-balanced InAs/InAsSb superlattice design for a 4.8 μm wavelength detector cutoff at room temperature (4.1 μm at low temperature) is grown using molecular beam epitaxy. The optimized superlattice design exhibits excellent optical quality and achieves the ground state absorption level predicted by the model.

# 6. *Bi* AS A SURFACTANT IN *InAs/InAsSb* SUPERLATTICES

In addition to improving the optical quality of a superlattice by optimizing the design, the optical quality can be independently enhanced by optimizing the growth conditions through the use of a surfactant during growth. Several optimal and non-optimal strain-balanced InAs/InAsSb superlattices are grown by molecular beam epitaxy at growth temperatures ranging from 425 to 475 °C using Bi/In flux ratios ranging from 0.0 to 10.0%. The structural properties of these samples are assessed using reflection high-energy electron diffraction, X-ray diffraction, atomic force microscopy, and transmission electron microscopy, and the optical properties are assessed using photoluminescence spectroscopy. InAs/InAsSb superlattices grown at 425 and 430 °C exhibit improved integrated photoluminescence intensity for Bi/In flux ratios up to 1.0%. Optical quality continues to improve with increasing growth temperature up to 475 °C and Bi/In flux ratios up to 5.0% at the higher growth temperatures.

## 6.1 Growth and Structural Properties of InAs/InAsSb with Bi Surfactant

The impact of Bi as a surfactant is examined during the molecular beam epitaxy growth of strain-balanced InAs/InAsSb superlattices on (100)-oriented GaSb substrates. The sample cross sections provided in Figure 57 show the nominal layer structure for five different Bi surfactant sample sets. For each sample set, several strain-balanced InAs/InAsSb superlattices are grown using varying amounts of Bi as a surfactant throughout the entire superlattice layer structure (sample sets A and B) and during only

the InAs layers of the superlattice (sample sets C, D, and E). Samples are designated by the Bi/In flux ratio used during the growth of that sample expressed as a percentage, followed by the letter designation of the sample set to indicate from which surfactant study the sample is from. For example, a sample grown using a Bi/In flux ratio of 1.0% from sample set A is designated as sample 1.0-A. The growth conditions for the Bi surfactant samples are summarized in Table 17.

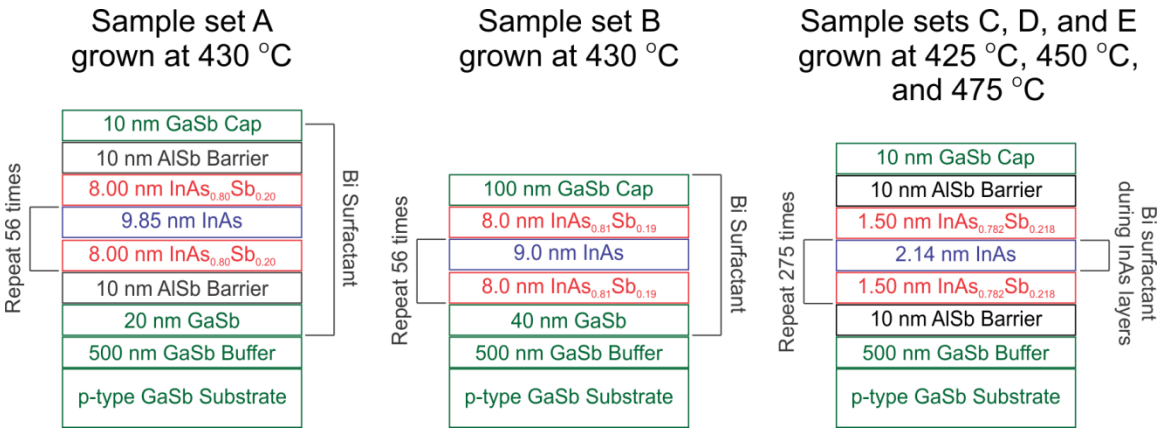


Figure 57. Cross section schematics of strain-balanced InAs/InAsSb superlattices grown using various growth temperatures and Bi/In flux conditions.

Table 17. Growth conditions (1) and structural properties (2) of the InAs/InAsSb superlattices grown with and without Bi as a surfactant. Sample names designate the Bi/In flux ratio used during growth as a percentage followed by the letter that identifies which surfactant sample set the sample belongs to in Figure 57.

| | (1) Growth conditions | | | (2) Structural properties | | | | |
|---|---|---|---|---|---|---|---|---|
| Sample | Growth temp. (°C) | Bi/In flux ratio | Sb/In flux ratio | Average unintentional Sb mole fraction in InAs | Sb mole fraction $x$ | InAs layer thickness (nm) | $InAs_{1-x}Sb_x$ layer thickness (nm) | Superlattice thickness (μm) |
| 0.0-A | 430 | 0.000 | 0.400 | 0.016 | 0.1680 | 9.17 | 7.43 | 0.94 |
| 0.5-A | 430 | 0.005 | 0.400 | 0.008 | 0.1645 | 9.14 | 7.40 | 0.93 |
| 1.0-A | 430 | 0.010 | 0.400 | 0.008 | 0.1690 | 9.12 | 7.38 | 0.93 |
| 2.0-A | 430 | 0.020 | 0.400 | 0.008 | 0.1635 | 9.09 | 7.36 | 0.93 |
| 0.0-B | 430 | 0.000 | 0.480 | 0.006 | 0.1825 | 9.01 | 7.99 | 0.96 |
| 0.3-B | 430 | 0.003 | 0.480 | 0.004 | 0.1840 | 9.01 | 7.99 | 0.96 |
| 1.0-B | 430 | 0.010 | 0.480 | 0.004 | 0.1780 | 9.03 | 8.01 | 0.96 |
| 3.0-B1 | 430 | 0.030 | 0.480 | 0.004 | 0.1760 | 8.98 | 7.96 | 0.96 |
| 3.0-B2 | 430 | 0.030 | 0.510 | 0.004 | 0.1850 | 9.01 | 7.99 | 0.96 |
| 0.0-C | 425 | 0.000 | 0.305 | 0.024 | 0.1970 | 2.15 | 1.51 | 1.01 |
| 0.5-C | 425 | 0.005 | 0.305 | 0.024 | 0.2010 | 2.15 | 1.52 | 1.01 |
| 2.0-C | 425 | 0.020 | 0.305 | 0.024 | 0.2040 | 2.15 | 1.51 | 1.01 |
| 5.0-C | 425 | 0.050 | 0.305 | 0.024 | 0.2170 | 2.14 | 1.51 | 1.01 |
| 0.0-D | 450 | 0.000 | 0.280 | 0.024 | 0.1470 | 2.15 | 1.51 | 1.01 |
| 0.5-D | 450 | 0.005 | 0.280 | 0.024 | 0.1900 | 2.13 | 1.50 | 1.00 |
| 2.0-D | 450 | 0.020 | 0.280 | 0.024 | 0.2050 | 2.15 | 1.52 | 1.01 |
| 5.0-D | 450 | 0.050 | 0.280 | 0.024 | 0.2130 | 2.16 | 1.52 | 1.01 |
| 10.0-D | 450 | 0.100 | 0.280 | 0.024 | 0.2170 | 2.15 | 1.52 | 1.01 |
| 0.0-E | 475 | 0.000 | 0.300 | 0.024 | 0.2220 | 2.06 | 1.45 | 0.99 |
| 5.0-E | 475 | 0.050 | 0.300 | 0.024 | 0.2280 | 2.06 | 1.45 | 0.97 |

The growths of Bi surfactant sample sets A and B are performed at 430 °C using a 1.20 As/In flux ratio which is calibrated during the growth of GaAs on GaAs at 590 °C by identifying the As-flux at which Ga-droplets begin to form on the surface for a fixed Ga-flux. The As/In flux ratio is obtained by comparing the unity As/Ga flux ratio to the In-flux which produces the 0.5 monolayer per second growth rate utilized during the InAs/InAsSb superlattice growths. Reflection high-energy electron diffraction is used to study the surface reconstructions of the InAs/InAsSb superlattices grown under these As-flux conditions with and without Bi surfactant. The InAs layers of the superlattice exhibit a faint (2×1) surface reconstruction which changes to a strong (1×3) with the presence of Bi on the surface during growth, whereas the InAsSb layers exhibit a (2×3) surface reconstruction with and without Bi as seen in Figure 58.

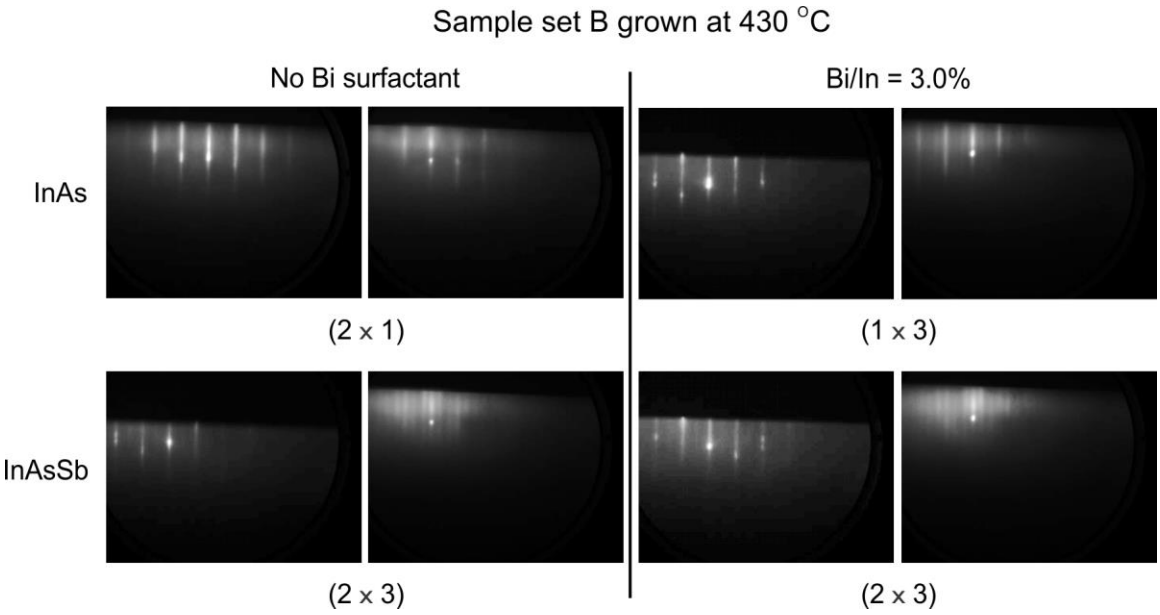


Figure 58. Surface reconstructions of InAs and InAsSb grown at 430 °C with and without a 3.0% Bi/In flux ratio measured using reflection high-energy electron diffraction.

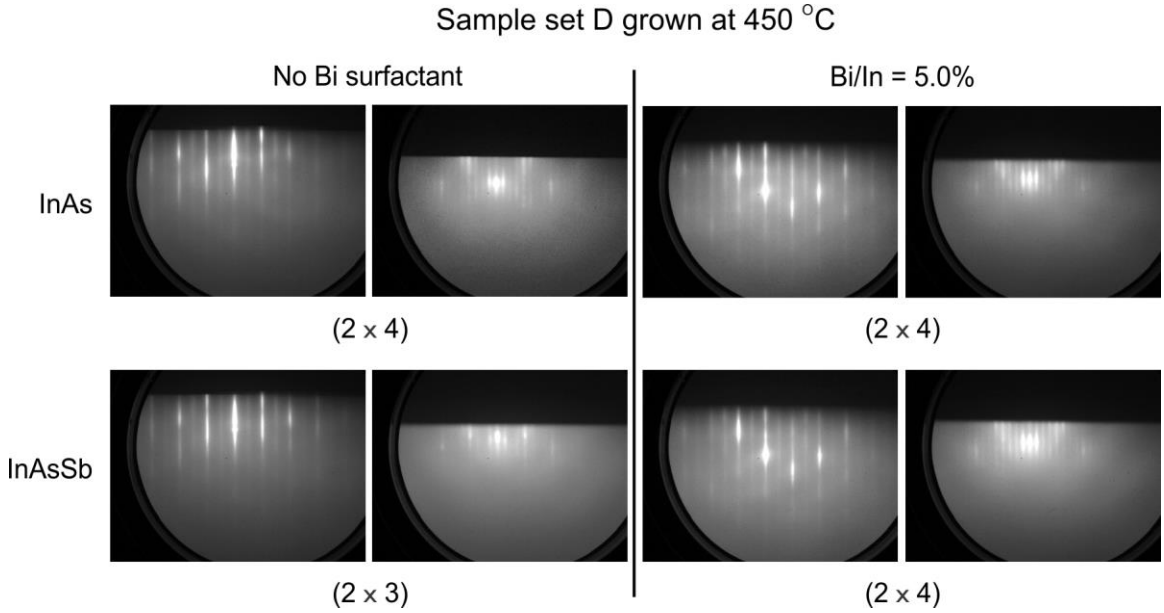


Figure 59. Surface reconstructions of InAs and InAsSb grown at 450 °C with and without a 5.0% Bi/In flux ratio measured using reflection high-energy electron diffraction.

On the other hand, Bi surfactant sample sets C, D, and E are grown at 425, 450, and 475 °C using a 1.20 As/In flux ratio which is calibrated during the growth of InAs on InAs at 450 °C by identifying the As-flux at which the InAs surface reconstruction changes from the As-rich (2×4) to the In-rich (4×2). This calibration method produces a unity As/In flux ratio which calls for less As than is required when utilizing the flux calibrated during the growth of GaAs at 590 °C. This is evident by the fact that samples grown in sample sets C, D, and E using a 1.20 As/In flux ratio calibrated by reflection high-energy electron diffraction exhibit the As-rich (2×4) surface reconstruction [32], whereas the (2×1) surface reconstruction is only observed for larger As-fluxes. For the samples grown under these As-flux conditions, the InAs layers grow with a (2×4) surface

reconstruction without and with a Bi/In flux ratio of 5% at 425 °C (sample set C) and 10% at 450 °C (sample set D). The InAsSb layers exhibit a (2×3) surface reconstruction without Bi and a (2×4) surface reconstruction when Bi is present even though the Bi shutter is only open during the growth of the InAs layers. This indicates that the surfactant Bi layer remains on the surface throughout the growth of the 1.5 nm thick InAsSb layer while the Bi shutter is closed. These surface reconstructions are shown in Figure 59.

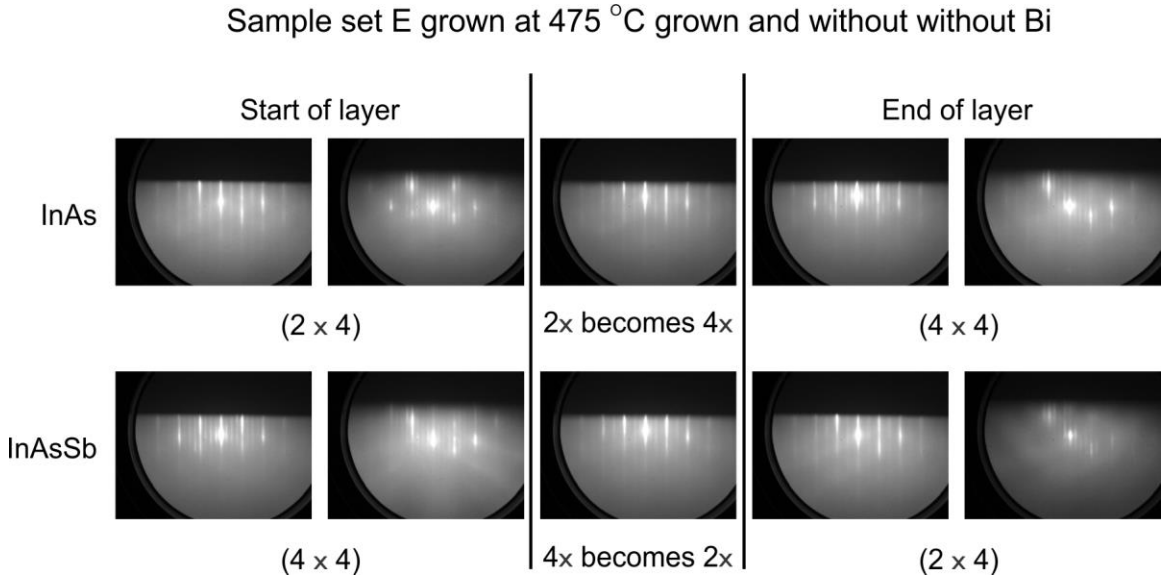


Figure 60. Surface reconstructions of InAs and InAsSb grown at 475 °C measured using reflection high-energy electron diffraction. The surface reconstructions change over the growth of each layer, and are unchanged with the presence of Bi.

The unity As/In flux is constant for temperatures below 450 °C, however more As is required to prevent the formation of In-droplets at higher growth temperatures. For the samples grown at 475 °C (sample set E), the surface reconstruction changes from the As-rich (2×4) to a (4×4) during the growth of the InAs layers of the superlattice, and subsequently changes back to a (2×4) at the start of each InAsSb layer as Sb restores the growth surface to group-V rich conditions as shown in Figure 60. The surface reconstructions at 475 °C are independent of Bi for Bi/In flux ratios up to 5.0%, however the frequent transitions from group-V to group-III rich growth during the InAs layers resulted in these samples getting slightly rough due to the formation of In-droplets.

Although the presence of Bi modifies the surface reconstructions during growth, there is no observed change in the surface morphology of the completed samples. Tapping-mode atomic force microscope measurements performed on the InAs/InAsSb superlattices in sample set B show that the surfaces are very smooth with a root mean square roughness of 0.05 nm over 1x1 $\mu m^2$ areas for all samples grown with and without Bi as surfactant. Bright field transmission electron micrographs of samples 0.0-B (no Bi) and 0.3-B (0.3% Bi/In) in Figure 61 show that the layers grown with and without Bi are exceptionally smooth, uniform, and free of extended defects over large lateral distances. The upper micrograph shows the full cross-sectional profile of the sample grown without Bi from the GaSb buffer to the 100 nm thick GaSb cap. The lower micrograph shows a higher magnification view of the GaSb buffer and superlattice interfaces for the sample grown using a 0.3% Bi/In flux ratio.

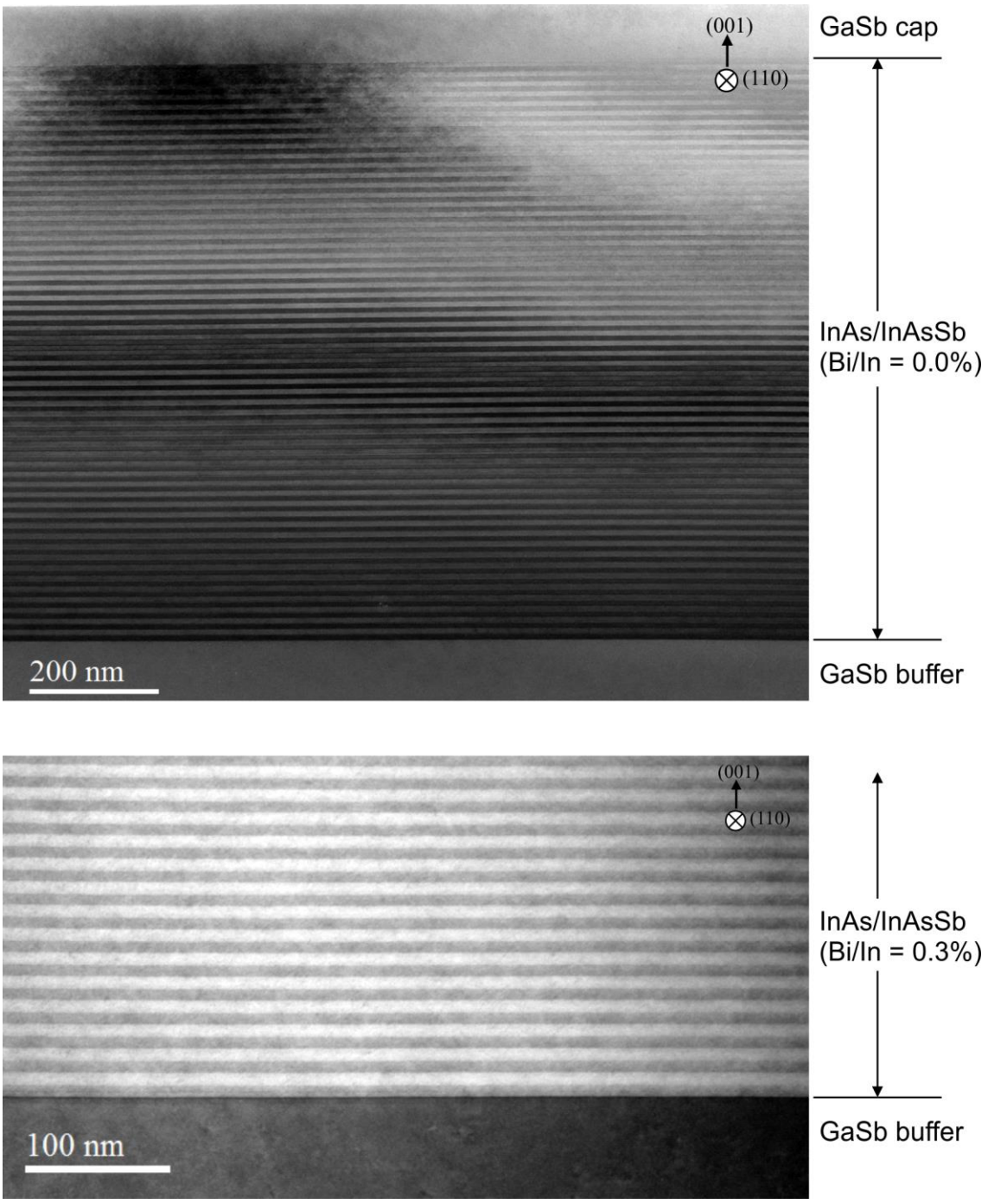


Figure 61. Bright field transmission electron micrographs of strain-balanced InAs/InAsSb superlattices grown without (upper, sample 0.0-B) and with (lower, sample 0.3-B) Bi as a surfactant, showing smooth, uniform layers and no extended defects over large lateral distances. **Image acquired by Jing Lu and Dr. David J. Smith at Arizona State University* [11].

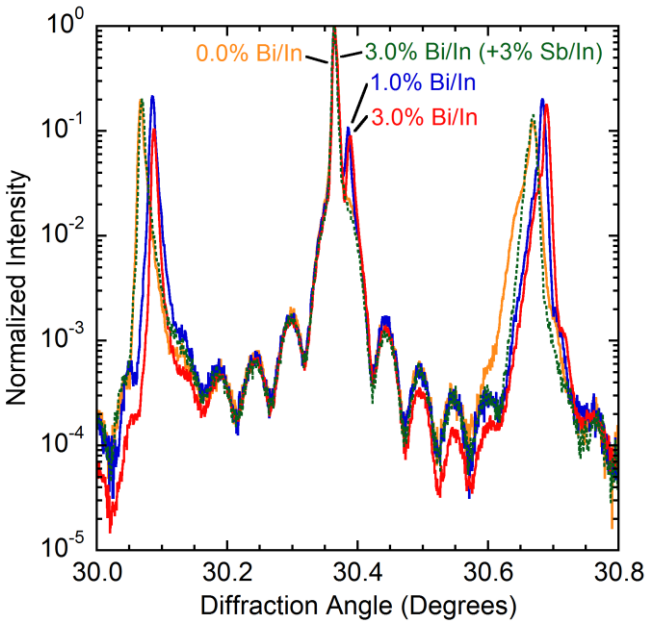


Figure 62. X-ray diffraction patterns of InAs/InAsSb superlattices grown using Bi as a surfactant (sample set B). With increasing Bi/In flux, the superlattice satellite peaks shift to the right indicating decreasing Sb incorporation (solid curves). The sample with 3.0% Bi/In is repeated using a 3% larger Sb/In flux to restore strain-balance (dotted green curve).

The structural parameters given in part 2 of Table 17 are determined from the analysis of the (004)-plane X-ray diffraction patterns of each sample and the analysis method described in Section 4.2 to quantify the unintentional Sb incorporation in the InAs layers of the superlattices. Figure 62 plots the X-ray diffraction patterns of the samples in sample set B which shows a right-shift in the superlattice satellite peaks with increasing Bi/In flux and a constant Sb/In flux ratio (samples 0.0-B, 1.0-B, and 3.0-B1). A right-shift to larger diffraction angles indicates increasing tensile strain in the structure corresponding to a reduction in the incorporation of Sb due to the presence of Bi on the

growth surface. The growth of the 3.0% Bi/In sample is repeated (sample 3.0-B2) using 3.0% additional Sb/In flux in order to compensate for the reduced incorporation of Sb in the InAsSb layers of the superlattice, and restore strain-balance as seen in the reciprocal space map in Figure 63. Figure 64 plots the Sb sticking coefficient (Sb mole fraction divided by Sb/In flux ratio) as a function of Bi/In flux ratio, which shows that the Sb sticking coefficient is approximately 40% at 430 °C, and decreases by a few percent when Bi is present on the surface. This sticking coefficient is consistent with the sticking coefficient determined from sample set A grown at the same temperatures using the same As-flux conditions.

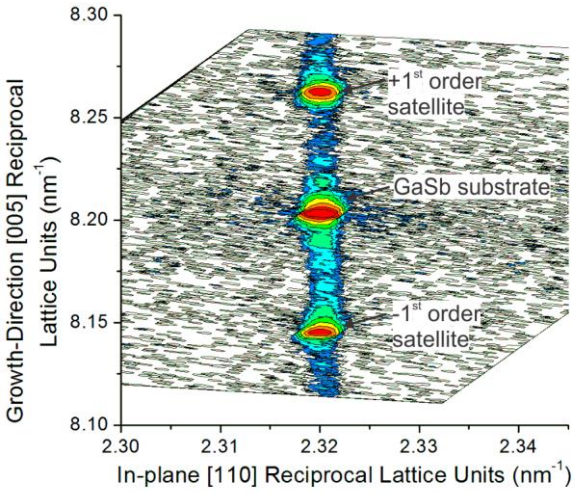


Figure 63. Reciprocal space map of an InAs/InAsSb superlattice (sample 3.0-B2) which demonstrates perfect strain-balance on the GaSb substrate.

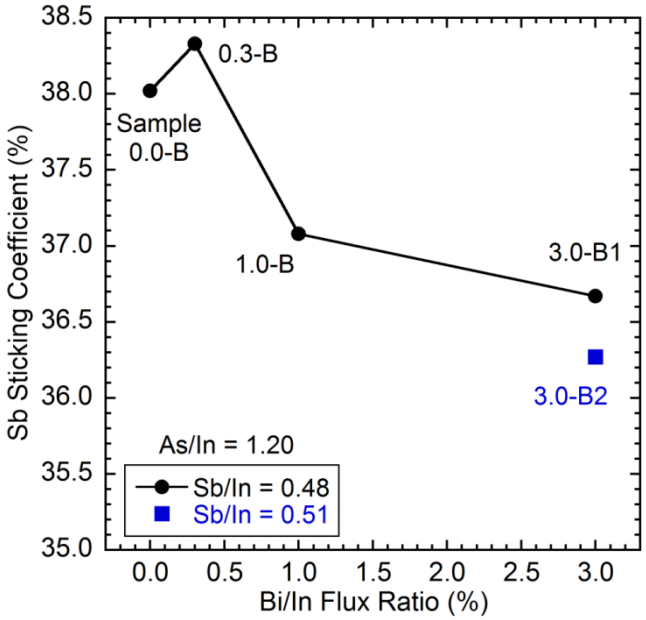


Figure 64. Sticking coefficient of Sb during the growth of InAs/InAsSb superlattices at 430 °C as a function of the Bi/In flux ratio. The results from samples grown using a 0.48 Sb/In flux ratio are shown by the black circles and indicate that the presence of Bi on the surface reduces the Sb sticking coefficient slightly. A fifth sample grown using a 3% Bi/In flux ratio and a 0.51 Sb/In flux ratio results in a similar Sb sticking coefficient and restored strain-balanced due to the increased Sb-flux (blue square).

For sample sets C, D, and E, there is relatively less As/In on the surface compared to sample sets A or B, which allows Sb to incorporate more readily. The unintentional Sb in the InAs layers of the superlattice was not precisely quantifiable using X-ray due to the short period thickness of this sample structure which resulted in there being very few satellite peaks to analyze. An unintentional Sb mole fraction of 0.024 is assumed based on the observation that the average unintentional Sb mole fractions roughly doubled from 0.006 to 0.012 upon halving the InAs layer thickness of samples in Table 12 from 16 to 8 nm. In addition, the Bi surfactant is only supplied during the InAs layers and given that

Bi reduces the sticking coefficient of Sb, the Bi surfactant may aid in reducing the unintentional Sb incorporation into the InAs layers of the superlattice. More work is needed to accurately quantify the average unintentional Sb incorporation in InAs as a function of Bi/In flux ratio.

## 6.2 Optical Properties of InAs/InAsSb with Bi Surfactant

Photoluminescence from the InAs/InAsSb Bi surfactant sample sets is measured at 12 K using a Nicolet Instrument Corporation Magna-IR 760 Fourier transform infrared spectrometer and 68 mW of pump power from an 808 nm laser. The photoluminescence spectra of sample sets A (solid curves) and B (dotted curves) are plotted as a function of photon energy in Figure 65a. The horizontal shifts in the photoluminescence peak positions are consistent with the reduced incorporation of Sb due to the Bi surfactant supplied throughout the entire superlattice region during the growth of these samples. The photoluminescence is integrated as a function of photon energy to assess the impact of Bi on the optical quality of these samples in Figure 65b. The integrated photoluminescence intensity increases with increasing Bi/In flux ratio up to 1.0%, indicating that there is an improvement in the optical quality due the presence of a small amount of Bi on the surface of the growing film at 430 °C. The two samples grown using a Bi/In flux ratio of 3.0% (samples 3.0-B1 and 3.0-B2) both exhibit reduced intensity compared to the sample grown without Bi, indicating that small deviations from the strain-balance condition do not significantly impact the photoluminescence intensity. Under these growth conditions at 430 °C, the optimal Bi/In flux ratio is around 1.0%.

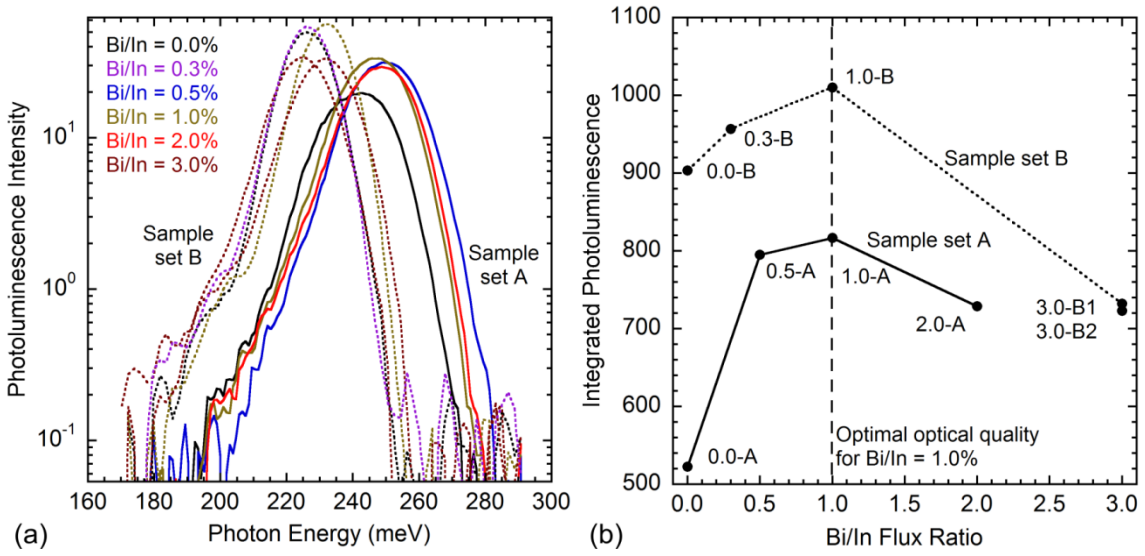


Figure 65. Photoluminescence from strain-balanced InAs/InAsSb superlattices grown at 430 °C using Bi as a surfactant; (a) spectra and (b) integrated photoluminescence as a function of Bi/In flux ratio. Solid curves represent samples from surfactant set A and dotted curves represent samples from surfactant set B. The maximum integrated photoluminescence intensity occurs for a Bi/In flux ratio of 1% (vertical dashed line) for both sample sets.

Photoluminescence from sample sets C, D, and E is of particular interest because the design given in Figure 57 is the mid-wave infrared optimal design for the strain-balanced InAs/InAsSb superlattice system. Furthermore, sample 0.0-C is the same optimized InAs/InAsSb superlattice sample examined using spectroscopic ellipsometry in Section 5.7. The low temperature photoluminescence spectra measured using 100 mW of power are compared in Figure 66a; solid curves for sample set C, dotted curves for sample set D, and dashed curves for sample set E.

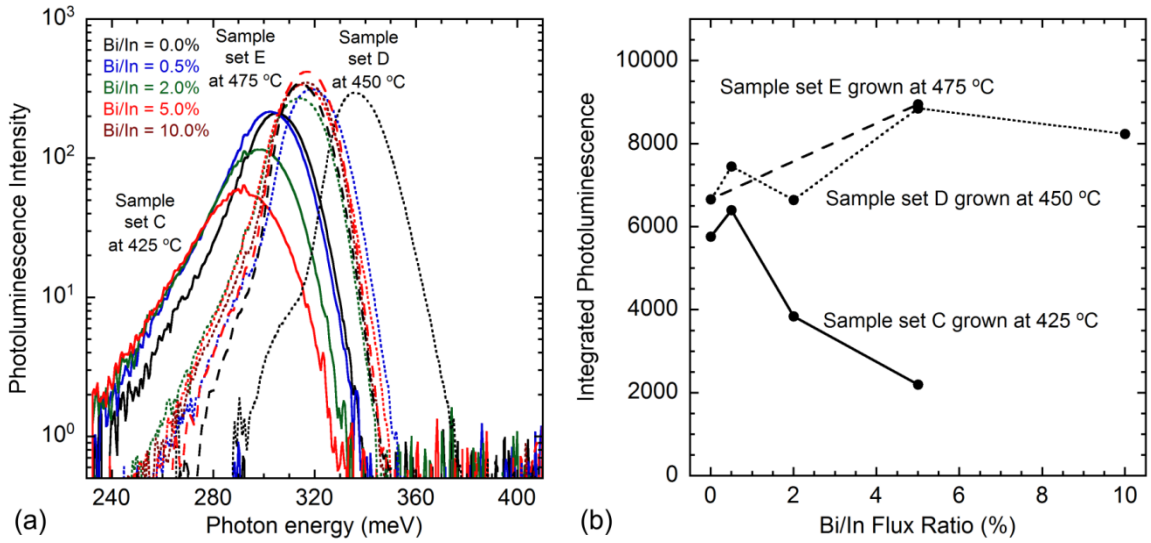


Figure 66. Photoluminescence from strain-balanced InAs/InAsSb superlattices grown at temperatures ranging from 425 to 475 °C using Bi as a surfactant; (a) spectra and (b) integrated photoluminescence as a function of Bi/In flux ratio. Solid curves represent samples from surfactant set C, dotted curves represent samples from surfactant set D, and dashed curves represent samples from surfactant set E. The maximum integrated photoluminescence intensity occurs for a Bi/In flux ratio of 1% for samples grown at 425 °C and 5% for samples grown at 450 and 475 °C.

When Bi is utilized as a surfactant during the growth of the optimized mid-wave infrared designs at 425 °C, there is an improvement to the optical quality of the material as evidenced by the increase in integrated photoluminescence intensity for a Bi/In flux ratio of 0.5% which is consistent with what is observed from the non-optimal superlattice designs grown at 430 °C in Figure 65. The optical quality of the superlattice is further improved by growing the samples at 450 and 475 °C, and moreover the use of higher growth temperatures allows for larger Bi/In flux ratios to be utilized as the optical quality continues to improve for Bi/In flux ratios in excess of 5.0% at these temperatures. In

addition, the two samples grown at 475 °C were rough due to the formation of In-droplets during growth, yet the photoluminescence intensity remains high indicating that higher growth temperatures may yield even better results if the growth conditions are further explored.

## 6.3 Chapter 6 Summary

The use of Bi as a surfactant during the growth of strain-balanced InAs/InAsSb superlattices is studied using reflection high-energy electron diffraction, X-ray diffraction, atomic force microscopy, transmission electron microscopy, and photoluminescence spectroscopy. The surface reconstruction of InAs is modified by the presence of Bi on the growth surface, and excellent structural quality is observed from the transmission electron micrographs. A Bi/In flux ratio of 1% results in optimal photoluminescence efficiency for superlattices grown at 425 °C, and optical quality is further enhanced by the use of higher growth temperatures and Bi/In flux ratios up to 5%.

# 7. CONCLUSIONS

Extending the spectral range over which III-V optoelectronic devices operate is of great scientific and technological importance. Bulk alloys, quantum wells, and superlattice systems utilizing InAsSb and InAsBi are attractive candidates due to their small bandgap energies and the wide range of design freedom afforded by the nearby InAs and GaSb lattice constants which enable low defect pseudomorphic growth of these materials on commercially-available binary substrates. In particular, InAsSb and InAsBi can be utilized as lattice-matched constituents on GaSb, as strained or unstrained quantum wells on InAs or GaSb, or as strain-balanced or lattice-matched constituents in superlattices on InAs or GaSb.

Smooth, droplet-free bulk layers of InAsBi are grown on GaSb substrates using molecular beam epitaxy. The growth conditions for InAsBi with and without the formation of Bi-droplets are explored, resulting in the identification of a growth window for high-quality droplet-free material. Detailed analysis of the flux conditions indicates that As behaves as a reactive surfactant during the growth of InAsBi, where an optimal amount of As on the growth surface produces the most efficient incorporation of Bi in the growing film. InAsBi layers with Bi mole fractions as large as 6.4%, nearly lattice-matched to the underlying GaSb substrate, are obtained. The bandgap of this material is measured using spectroscopic ellipsometry and is utilized in a valence band anticrossing model of the InAsBi band structure to characterize the 1.529 eV coupling strength of the valence band anticrossing interaction in InAsBi. The optical properties of InAsBi are

assessed using InAs/InAsBi quantum wells grown on GaSb, which exhibit radiative recombination limited photoluminescence over most temperatures and excitation levels.

The strain-balanced InAs/InAsSb superlattice is another ternary material system at the GaSb lattice constant that is capable of covering the mid- to long-wavelength infrared. During molecular beam epitaxy growth, surface segregated Sb continues to incorporate into the InAs layers of the superlattice after the Sb-flux has been blocked by the closed shutter. The approximately 1% unintentional Sb in the InAs layers of the superlattice must be accounted for to obtain an accurate measurement of the temperature and composition dependent InAs/InAsSb band alignment. The period thickness and Sb mole fraction of the superlattice strongly affect the effective bandgap and electron-hole wavefunction overlap, but only weakly affect the optical joint density of states. The superlattice absorption coefficient is found to be proportional to the square of the wavefunction overlap, indicating that wavefunction overlap is an important design parameter for maximizing absorption in these structures. Superior absorption properties and optical quality is observed from InAs/InAsSb superlattices that are optimized to establish maximum wavefunction overlap. Optical quality is further improved in these structures with the use of Bi as a surfactant during molecular beam epitaxy growth; an optimal Bi/In flux ratio of 1% is identified for growth at 430 °C and an optimal Bi/In flux ratio of 5% is identified for growth at 450 °C and higher.

A software tool is developed that calculates the miniband structure of semiconductor superlattices and identifies optimized designs in terms of maximizing absorption as a function of transition energy. These functionalities are demonstrated by

mapping the design spaces of lattice-matched GaSb/$InAs_{0.911}Sb_{0.089}$ and GaSb/$InAs_{0.932}Bi_{0.068}$ superlattices and strain-balanced InAs/InAsSb, InAs/GaInSb, and InAs/InAsBi superlattices on GaSb substrates. In addition to determining the optimal designs, practical design constraints inherent to epitaxial growth are implemented to limit results to what can practically be grown with high structural and optical quality. The optimized design criteria are provided for each superlattice system at key detector wavelengths across the infrared.

REFERENCES


[1] J. R. Biard, E. L. Bonin, W. N. Carr, and G. E. Pittman, Int. El. Devices Meet. **8**, 96 (1962).

[2] R. N. Hall, G. E. Fenner, J. D. Kingsley, T. J. Soltys, and R. O. Carlson, Phys. Rev. Lett. **9**, 366 (1962).

[3] I. Vurgaftman, J. R. Meyer, and L. Ram-Mohan, J. Appl. Phys. **89**, 5815 (2001).

[4] P. T. Webster, N. A. Riordan, S. Liu, E. H. Steenbergen, R. A. Synowicki, Y.-H. Zhang, and S. R. Johnson, J. Appl. Phys. **118**, 245706 (2015).

[5] P. T. Webster, A. J. Shalindar, N. A. Riordan, C. Gogineni, H. Liang, A. R. Sharma, and S. R. Johnson, *to be published*.

[6] H. Kroemer, Proc. IEEE **51**, 1782 (1963).

[7] H. Kroemer, Proc. IEEE **101**, 2183 (2013).

[8] J. W. Matthews and A. E. Blakeslee, J. Cryst. Growth **27**, 118 (1974).

[9] H. Okamoto and K. Oe, Jpn. J. Appl. Phys. **38**, 1022 (1999).

[10] Z. M. Fang, K. Y. Ma, R. M. Cohen, and G. B. Stringfellow, J. Appl. Phys. **68**, 1187 (1990).

[11] P. T. Webster, N. A. Riordan, C. Gogineni, S. Liu, J. Lu, X.-H. Zhao, D. J. Smith, Y.-H. Zhang, and S. R. Johnson, J. Vac. Sci. Technol. B **32**, 02C120 (2014).

[12] A. J. Shalindar, P. T. Webster, B. J. Wilkens, T. L. Alford, and S. R. Johnson, *to be published*.

[13] L. Esaki and R. Tsu, IBM J. Res. Dev. **14**, 61 (1970).

[14] Y.-H. Zhang, Appl. Phys. Lett. **66**, 118 (1995).

[15] E. H. Steenbergen, B. C. Connelly, G. D. Metcalfe, H. Shen, M. Wraback, D. Lubyshev, Y. Qiu, J. M. Fastenau, A. W. K. Liu, S. Elhamri, O. O. Cellek, and Y.-H. Zhang, Appl. Phys. Lett. **99**, 251110 (2011).

[16] B. V. Olsen, E. A. Shaner, J. K. Kim, J. F. Klem, S. D. Hawkins, L. M. Murray, J. P. Prineas, M. E. Flatté, and T. F. Boggess, Appl. Phys. Lett. **101**, 092109 (2012).

[17] J. Pellegrino and R. DeWames, Proc. SPIE **7298**, 72981U (2009).

[18] N. J. Ekins-Daukes, K. Kawaguchi, and J. Zhang, Cryst. Growth Des. **2**, 287 (2002).

[19] P. T. Webster, N. A. Riordan, S. Liu, E. H. Steenbergen, R. A. Synowicki, Y.-H. Zhang, and S. R. Johnson, Appl. Phys. Lett. **106**, 061907 (2015).

[20] M. Copel, M. C. Reuter, E. Kaxiras, and R. M. Tromp, Phys. Rev. Lett. **63**, 632 (1989).

[21] E. Tournié, N. Grandjean, A. Trampert, J. Massies, and K. H. Ploog, J. Cryst Growth **150**, 460 (1995).

[22] Yu. G. Sadofyev, S. R. Johnson, S. A. Chaparro, Y. Cao, D. Ding, J.-B. Wang, K. Franzreb, and Y.-H. Zhang, Appl. Phys. Lett. **84**, 3546 (2004).

[23] S. R. Johnson, Yu. G. Sadofyev, D. Ding, Y. Cao, S. A. Chaparro, K. Franzreb, and Y.-H. Zhang, J. Vac. Sci. Technol. B **22**, 1436 (2004).

[24] S. Tixier, M. Adamcyk, E. C. Young, J. H. Schmid, and T. Tiedje, J. Cryst. Growth **251**, 449 (2003).

[25] E. C. Young, S. Tixier, and T. Tiedje, J. Cryst. Growth **279**, 316 (2005).

[26] A. Janotti, Su-Huai Wei, and S. B. Zhang, Phys. Rev. B **65**, 115203 (2002).

[27] N. A. Riordan, C. Gogineni, S. R. Johnson, X. Lu, T. Tiedje, D. Ding, Y.-H. Zhang, R. Fritz, K. Kolata, S. Chatterjee, K. Volz, and S. W. Koch, J. Mater. Sci. **23**, 1799 (2012).

[28] S. Francoeur, M.-J. Seong, A. Mascarenhas, S. Tixier, M. Adamcyk, T. Tiedje, Appl. Phys. Lett. **82**, 3874 (2003).

[29] V. Pačebutas, K. Bertulis, L. Dapkus, G. Aleksejenko, A. Krotkus, K. M. Yu, and W. Walukiewicz, Semicond. Sci. Technol. **22**, 819 (2007).

[30] K. Alberi, J. Wu, W. Walukiewicz, K. M. Yu, O. D. Dubon, S. P. Watkins, C. X. Wang, X. Liu, Y.-J. Cho, and J. Furdyna, Phys. Rev. B **75**, 045203, (2007).

[31] W. Martienssen, *Springer Handbook of Condensed Matter and Materials Data.* (Springer Berlin Heidelberg, 2005), pp. 98.

[32] A. S. Bracker, M. J. Yang, B. R. Bennett, J. C. Culbertson, and W. J. Moore, J. Cryst. Growth **220**, 384 (2000).

[33] 3G Series 10C05 system, Ircon Inc., Santa Cruz, CA USA.

[34] X'pert Epitaxy software, PANalytical B. V., Almelo, The Netherlands.

[35] J. Massies, N. Grandjean, and V. H. Etgens, Appl. Phys. Lett. **61**, 99 (1992).

[36] N. Grandjean and J. Massies, Phys. Rev. B **53**, R13231 (1996).

[37] C. D. Consorte, C. Y. Fong, M. D. Watson, L. H. Yang, and S. Ciraci, Mater. Sci. Eng. B **96**, 141 (2002).

[38] VASE and IR-VASE systems, J. A. Woollam Co. Inc., Lincoln, NE USA.

[39] WVASE software, J. A. Woollam Co. Inc., Lincoln, NE USA.

[40] M. Schubert, *Infrared Ellipsometry on Semiconductor Layer Structures: Phonons, Plasmons, and Polaritons.* (Springer, Heidelberg, 2004), pp. 21.

[41] R. de L. Kronig, J. Opt. Soc. Am. Rev. Scient. Instrum. **12**, 547 (1926).

[42] H. A. Kramers, Atti Congr. Int. Fis. Como **2**, 545 (1927).

[43] S. L. Chuang, *Physics of Optoelectronic Devices*. (Wiley, New York, 1995), pp. 671-674.

[44] M. Gladysiewicz, R. Kudrawiec, and M. S. Wartak, J. Appl. Phys. **118**, 055702 (2015).

[45] J. Wu, W. Shan, and W. Walukiewicz, Semicond. Sci. Technol. **17**, 860 (2002).

[46] G. L. Bir and G. E. Pikus, *Symmetry and Strain-Induced Effects in Semiconductors*. (Wiley, New York, 1974).

[47] S. L. Chuang, *Physics of Optoelectronic Devices* (Wiley, New York, 1995).

[48] S. Imhof, A. Thränhardt, A. Chernikov, M. Koch, N. S. Köster, K. Kolata, S. Chatterjee, S. W. Koch, X. Lu, S. R. Johnson, D. A. Beaton, T. Tiedje, O. Rubel, Appl. Phys. Lett. **96**, 131115 (2010).

[49] C. Gogineni, N. A. Riordan, S. R. Johnson, X. Lu, and T. Tiedje, Appl. Phys. Lett. **103**, 041110, (2013).

[50] K. L. Teo, J. S. Colton, P. Y. Yu, E. R. Weber, M. F. Li, W. Liu, K. Uchida, H. Tokunaga, N. Akutsu, and K. Matsumoto, Appl. Phys. Lett. **73**, 1697, (1998).

[51] L. Viña, S. Logothetidis, and M. Cardona, Phys. Rev. B **30**, 1979 (1984).

[52] S. R. Johnson and T. Tiedje, J. Appl. Phys. **78**, 5609 (1995).

[53] E. F. Schubert, *Light-Emitting Diodes*. (Cambridge University Press, New York, 2007), pp. 87-90.

[54] F. Urbach, Phys. Rev. **92**, 1324 (1953).

[55] S. P. Svensson, W. L. Sarney, H. Hier, Y. Lin, D. Wang, D. Donetsky, L. Shterengas, G. Kipshidze, and G. Belenky, Phys. Rev. B **86**, 245205 (2012).

[56] Y. P. Varshni, Physica (Utrecht) **34**, 149 (1967).

[57] R. Pässler and G. Oelgart, J. Appl. Phys. **82**, 2611 (1997).

[58] S. A. Lourenço, I. F. L. Dias, J. L. Duarte, E. Laureto, E. A. Meneses, J. R. Leite, and I. Mazzaro, J. Appl. Phys. **89**, 6159 (2001).

[59] R. Pässler, J. Appl. Phys. **89**, 6235 (2001).

[60] Z. M. Fang, K. Y. Ma, D. H. Jaw, R. M. Cohen, and G. B. Stringfellow, J. Appl. Phys. **67**, 7034 (1990).

[61] B. R. Bennett, B. V. Shanabrook, R. J. Wagner, J. L. Davis, and J. R. Waterman, Appl. Phys. Lett. **63**, 949 (1993).

[62] A. Y. Lew, E. T. Yu, and Y.-H. Zhang, J. Vac. Sci. Technol. B **14**, 2940 (1996).

[63] L. Ouyang, E. H. Steenbergen, Y.-H. Zhang, K. Nunna, D. L. Huffaker, and D. J. Smith, J. Vac. Sci. Technol. B **30**, 02B106 (2012).

[64] M. R. Wood, K. Kanedy, F. Lopez, M. Weimer, J. F. Klem, S. D. Hawkins, E. A. Shaner, and J. K. Kim, J. Cryst. Growth **425**, 110 (2015).

[65] V. S. Speriosu and T. Vreeland Jr., J. Appl. Phys. **56**, 1591 (1984).

[66] P. G. Snyder, B. N. De, G. Merkel, and J. A. Woollam, Superlattice Microst. **4**, 97 (1988).

[67] J. A. Woollam, P. G. Snyder, K. G. Merkel, and S. A. Alterovitz, Mater. Sci. Eng. B **5**, 291 (1990).

[68] J. Wagner, J. Schmitz, N. Herres, F. Fuchs, and M. Walther, J. Appl. Phys. **83**, 5452 (1998).

[69] R. de L. Kronig and W. G. Penney, Proc. R. Soc. Lond. A **130**, 499 (1931).

[70] H.-S. Cho and P. R. Prucnal, Phys Rev. B **36**, 3237 (1987).

[71] S.-H. Pan and S.-M Feng, Phys. Rev. B **44**, 5668 (1991).

[72] M. W. Prairie and R. M. Kolbas, Superlattice Microst. **7**, 269 (1990).

[73] D. Lackner, O. J. Pitts, M. Steger, A. Yang, M. L. W. Thewalt, and S. P. Watkins, Appl. Phys. Lett. **95**, 081906 (2009).

[74] Y. Lin, D. Wang, D. Donetsky, L. Shterengas, G. Kipshidze, G. Belenky, S. P. Svensson, W. L. Sarney, and H. Hier, J. Electron. Mater. **42**, 918 (2013).

[75] E. Merzbacher, *Quantum Mechanics*. (Wiley, New York, 1970), pp. 490.

[76] S. L. Chuang, *Physics of Optoelectronic Devices*. (Wiley, New York, 1995), pp. 355.

[77] C. Kittel, *Introduction to Solid State Physics*. (Wiley, New York, 2005), pp. 198.

[78] A. P. Roth, W. J. Keeler, and E. Fortin, Can. J. Phys. **58**, 560 (1980).

[79] MATLAB 2011b, The MathWorks, Inc., Natick, MA USA.

[80] M. Kawabe, M. Kondo, N. Matsuura, and K. Yamamoto, Jpn. J. Appl. Phys. **22**, L64 (1983).

[81] A. C. Gossard, *Semiconductors and Semimetals* **40** (Academic Press, New York, 1994) p. 153-167.

# APPENDIX A

# BACKSIDE ROUGHING PROCEDURE

In order to determine the optical constants of a material using spectroscopic ellipsometry, the reflection and absorption introduced by each layer in the sample structure must be modeled. If the substrate on which the layer structure is grown is transparent over the spectral range of interest, then reflections from the backside of the wafer which are incoherent with respect to the reflections from the epitaxial layers can result, causing a depolarization in the total reflection reaching the detector. The intensity of the backside reflected beam can be minimized by roughing the backside of the substrate to minimize this depolarization and improve the accuracy of the modeled optical constants. The backside roughing procedure utilized in this work is detailed below.

1. Lay the sample epitaxial side down on a soft cleanroom wipe.
2. Take a cotton-tipped applicator and wrap a small piece of 400 grit sandpaper around the tip as shown in Figure A1.
3. Roughen the backside of the substrate with the sandpaper by making circular motions all around the back surface while using your other hand to keep the wafer held still.
4. As GaSb powder accumulates around the sample, move the wafer to other locations on the wipe to prevent the powder from moving under the wafer and scratching the epitaxial surface.
5. When the backside surface is a matte grey color, the surface may be sufficiently roughened. Measure the sample and verify that the percentage depolarization has been reduced. Depolarization values of a percent or so are acceptable, while values of 5% or more indicate that a significant backside reflection is still present.

Figure A1 shows the backside of a GaSb wafer being roughened, and the resulting matte grey color finish. Figures A2 and A3 show the ellipsometric parameters Ψ and Δ and the measurement depolarization from an InAs/InAsSb type-II superlattice (sample E, see Table 12), before and after backside roughing. Significant deviation between Ψ, Δ, and the percentage depolarization before and after backside roughing indicates that reflections from the backside of the GaSb wafer constituted a significant fraction of the total measured reflection at 67° angle of incidence.

Figure A1. Backside of a GaSb wafer being roughened using 400 grit sandpaper wrapped around a cotton-tipped applicator.

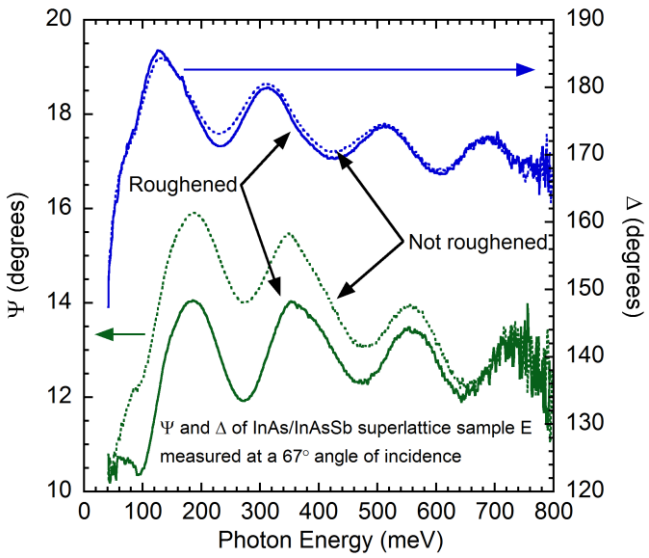


Figure A2. Ellipsometric parameters Ψ (left-hand vertical axis, green) and Δ (right-hand vertical axis, blue) of an InAs/InAsSb superlattice (sample E, see Table 12) measured before and after backside roughing of the GaSb substrate (dotted and solid curves).

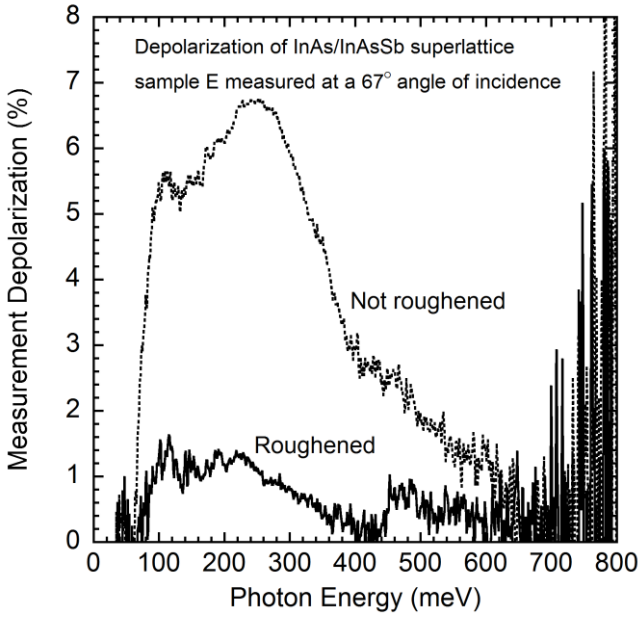


Figure A3. Depolarization of the reflection from an InAs/InAsSb superlattice (sample E, see Table 12) measured before and after backside roughing of the GaSb substrate (dotted and solid curves).

# APPENDIX B

# OPTIMIZED SUPERLATTICE DESIGN PARAMETERS

Table B1. Optimal and practical design parameters for lattice-matched GaSb/$InAs_{0.911}Sb_{0.089}$ superlattices. Electron-hole wavefunction overlap square $\left|\Psi_h^*\Psi_e\right|^2$, absorption coefficient $\alpha_{SL}$, and the superlattice constituent layer thicknesses are provided for several key detector wavelengths at low temperature (0 K) and at room temperature (295 K). When the optimal design calls for thicknesses less than 0.500 nm, an alternate set of practical design parameters are also provided which limit the minimum layer thickness to 0.500 nm. The horizontal dotted line separates designs in the digital alloy regime (above) and extended wavelength regime (below). In the digital alloy regime, the optimal design calls for an infinitesimal period thickness superlattice, therefore only the practical design parameters are given.

| Transition wavelength (μm) | | Optimal or practical | Wavefunction overlap square $\left\|\Psi_h^*\Psi_e\right\|^2$ (%) | Absorption coefficient $\alpha_{SL}$ ($cm^{-1}$) | GaSb thickness (nm) | $InAs_{0.911}Sb_{0.089}$ thickness (nm) |
|---|---|---|---|---|---|---|
| at 0 K | at 295 K | | | | | |
| 3.0 | 3.5 | Practical | 97.4 | 5484 | 0.500 | 1.540 |
| 4.0 | 4.8 | Optimal | 71.2 | 3553 | 0.550 | 4.630 |
| 5.0 | 6.4 | Optimal | 46.3 | 2310 | 1.170 | 4.350 |
| 8.0 | 12.1 | Optimal | 23.8 | 1188 | 1.870 | 5.650 |
| 10.0 | 17.2 | Optimal | 18.2 | 908 | 2.050 | 6.380 |
| 12.0 | 23.9 | Optimal | 15.0 | 749 | 2.210 | 6.880 |
| 15.0 | 39.1 | Optimal | 12.2 | 609 | 2.400 | 7.400 |

Table B2. Optimal and practical design parameters for lattice-matched GaSb/$InAs_{0.932}Bi_{0.068}$ superlattices. Electron-hole wavefunction overlap square $\left|\Psi_h^*\Psi_e\right|^2$, absorption coefficient $\alpha_{SL}$, and the superlattice constituent layer thicknesses are provided for several key detector wavelengths at low temperature (0 K) and at room temperature (295 K). When the optimal design calls for thicknesses less than 0.500 nm, an alternate set of practical design parameters are also provided which limit the minimum layer thickness to 0.500 nm. The horizontal dotted line separates designs in the digital alloy regime (above) and extended wavelength regime (below). In the digital alloy regime, the optimal design calls for an infinitesimal period thickness superlattice, therefore only the practical design parameters are given.

| Transition wavelength (μm) | | Optimal or practical | Wavefunction overlap square $\left\|\Psi_h^*\Psi_e\right\|^2$ (%) | Absorption coefficient $\alpha_{SL}$ ($cm^{-1}$) | GaSb thickness (nm) | $InAs_{0.932}Bi_{0.068}$ thickness (nm) |
|---|---|---|---|---|---|---|
| at 0 K | at 295 K | | | | | |
| 3.0 | 3.6 | Practical | 99.8 | 4334 | 0.500 | 0.610 |
| 4.0 | 5.1 | Practical | 99.3 | 3240 | 0.500 | 1.090 |
| 5.0 | 6.7 | Practical | 98.3 | 2571 | 0.500 | 1.640 |
| 8.0 | 13.2 | Practical | 90.0 | 1479 | 0.500 | 3.830 |
| 10.0 | 19.4 | Practical | 76.8 | 1013 | 0.500 | 5.810 |
| 12.0 | 28.0 | Optimal | 60.0 | 667 | 0.280 | 13.900 |
| 12.0 | 28.4 | Practical | 58.2 | 647 | 0.500 | 8.300 |
| 15.0 | 55.1 | Optimal | 40.7 | 453 | 0.860 | 7.160 |

Table B3. Optimal and practical design parameters for strain-balanced InAs/InAsSb, superlattices. Electron-hole wavefunction overlap square $\left|\Psi_h^*\Psi_e\right|^2$, absorption coefficient $\alpha_{SL}$, and the superlattice constituent layer thicknesses and mole fractions are provided for several key detector wavelengths at low temperature (0 K) and at room temperature (295 K). When the optimal design calls for thicknesses less than 0.500 nm or strain exceeding -2%, an alternate set of practical design parameters are also provided which limit the minimum layer thickness to 0.500 nm and the maximum strain to -2%. All designs are located within the extended wavelength regime.

| Transition wavelength (μm) | | Optimal or practical | Wavefunction overlap square $\left\|\Psi_h^*\Psi_e\right\|^2$ (%) | Absorption coefficient $\alpha_{SL}$ ($cm^{-1}$) | InAs thickness (nm) | InAsSb thickness (nm) | Sb mole fraction |
|---|---|---|---|---|---|---|---|
| at 0 K | at 295 K | | | | | | |
| 4.0 | 4.8 | Optimal | 94.6 | 4721 | 1.884 | 1.396 | 0.211 |
| 5.0 | 6.3 | Optimal | 66.3 | 3308 | 3.749 | 1.121 | 0.395 |
| 5.0 | 6.3 | Practical | 66.3 | 3308 | 3.748 | 1.162 | 0.384 |
| 8.0 | 12.3 | Optimal | 37.5 | 1871 | 5.780 | 1.160 | 0.550 |
| 8.0 | 12.1 | Practical | 34.8 | 1737 | 6.694 | 2.076 | 0.384 |
| 10.0 | 18.0 | Optimal | 31.3 | 1562 | 6.484 | 1.196 | 0.592 |
| 10.0 | 17.5 | Practical | 26.6 | 1327 | 8.465 | 2.625 | 0.384 |
| 12.0 | 26.2 | Optimal | 27.7 | 1382 | 6.970 | 1.220 | 0.620 |
| 12.0 | 25.1 | Practical | 21.2 | 1058 | 10.168 | 3.152 | 0.384 |
| 15.0 | 47.3 | Optimal | 24.5 | 1223 | 7.472 | 1.248 | 0.646 |
| 15.0 | 44.8 | Practical | 15.5 | 774 | 12.595 | 3.905 | 0.384 |

Table B4. Optimal and practical design parameters for strain-balanced InAs/GaInSb, superlattices. Electron-hole wavefunction overlap square $\left|\Psi_h^*\Psi_e\right|^2$, absorption coefficient $\alpha_{SL}$, and the superlattice constituent layer thicknesses and mole fractions are provided for several key detector wavelengths at low temperature (0 K) and at room temperature (295 K). When the optimal design calls for thicknesses less than 0.500 nm or strain exceeding -2%, an alternate set of practical design parameters are also provided which limit the minimum layer thickness to 0.500 nm and the maximum strain to -2%. The horizontal dotted line separates designs in the digital alloy regime (above) and extended wavelength regime (below). In the digital alloy regime, the optimal design calls for an infinitesimal period thickness superlattice, therefore only the practical design parameters are given.

| Transition wavelength (μm) | | Optimal or practical | Wavefunction overlap square $\left\|\Psi_h^*\Psi_e\right\|^2$ (%) | Absorption coefficient $\alpha_{SL}$ ($cm^{-1}$) | InAs thickness (nm) | GaInSb thickness (nm) | In mole fraction |
|---|---|---|---|---|---|---|---|
| at 0 K | at 295 K | | | | | | |
| 3.0 | 3.6 | Practical | 95.7 | 5501 | 1.488 | 0.502 | 0.297 |
| 4.0 | 5.0 | Optimal | 74.4 | 4226 | 3.239 | 0.491 | 0.676 |
| 4.0 | 5.1 | Practical | 71.3 | 4050 | 2.642 | 0.818 | 0.324 |
| 5.0 | 6.7 | Optimal | 55.5 | 3152 | 3.584 | 0.806 | 0.450 |
| 5.0 | 6.8 | Practical | 54.7 | 3107 | 3.275 | 1.015 | 0.324 |
| 8.0 | 13.6 | Optimal | 34.8 | 1977 | 4.623 | 1.177 | 0.396 |
| 8.0 | 13.7 | Practical | 34.5 | 1960 | 4.398 | 1.362 | 0.324 |
| 10.0 | 20.6 | Optimal | 29.3 | 1664 | 5.143 | 1.257 | 0.413 |
| 10.0 | 20.8 | Practical | 28.9 | 1642 | 4.848 | 1.502 | 0.324 |
| 12.0 | 31.4 | Optimal | 25.9 | 1471 | 5.551 | 1.299 | 0.432 |
| 12.0 | 31.8 | Practical | 25.5 | 1448 | 5.176 | 1.604 | 0.324 |
| 15.0 | 65.6 | Optimal | 22.9 | 1301 | 6.012 | 1.328 | 0.458 |
| 15.0 | 67.8 | Practical | 22.2 | 1261 | 5.535 | 1.715 | 0.324 |

Table B5. Optimal and practical design parameters for strain-balanced InAs/InAsBi, superlattices. Electron-hole wavefunction overlap square $\left|\Psi_h^*\Psi_e\right|^2$, absorption coefficient $\alpha_{SL}$, and the superlattice constituent layer thicknesses and mole fractions are provided for several key detector wavelengths at low temperature (0 K) and at room temperature (295 K). When the optimal design calls for thicknesses less than 0.500 nm or strain exceeding -2%, an alternate set of practical design parameters are also provided which limit the minimum layer thickness to 0.500 nm and the maximum strain to -2%. The horizontal dotted line separates designs in the digital alloy regime (above) and extended wavelength regime (below). In the digital alloy regime, the optimal design calls for an infinitesimal period thickness superlattice, therefore only the practical design parameters are given.

| Transition wavelength (μm) | | Optimal or practical | Wavefunction overlap square $\left\|\Psi_h^*\Psi_e\right\|^2$ (%) | Absorption coefficient $\alpha_{SL}$ ($cm^{-1}$) | InAs thickness (nm) | InAsBi thickness (nm) | Bi mole fraction |
|---|---|---|---|---|---|---|---|
| at 0 K | at 295 K | | | | | | |
| 10.0 | 19.0 | Practical | 99.7 | 1410 | 0.500 | 0.760 | 0.113 |
| 12.0 | 27.8 | Optimal | 98.3 | 1093 | 0.427 | 4.083 | 0.075 |
| 12.0 | 27.9 | Practical | 98.2 | 1092 | 0.500 | 3.350 | 0.078 |
| 15.0 | 51.5 | Optimal | 91.6 | 1019 | 1.322 | 2.008 | 0.113 |